FACULTY OF SCIENCE AND TECHNOLOGY

MASTER'S THESIS

Study programme / specialisation: Marine and Offshore Technology	The *(spring/autumn)* semester, *(year)* Spring 2023 Open / ~~Confidential~~
Author: Weixin Zeng	
Supervisor at UiS: Dr. Guang Yin Co-supervisor: Prof. Muk Chen Ong	
Thesis title: Numerical simulations of gas-liquid two-phase flow induced forces on 90-degere elbow structures	
Credits (ECTS): 30	
Keywords: Computational fluid dynamics; Multiphase flow; Elbows; Rigid Jumpers; Flow-induced vibration; One-way coupling; Dynamic response.	Pages:74 + appendix: 7 Stavanger, *(date)* June 15, 2023

Acknowledgements

In the beginning, I want to thank my supervisor Dr. Guang Yin for his selfless dedication and teaching during these two years. Dr. Guang Yin has not only supported me to solve technical difficulties from my first CFD projects to my master thesis, but also taught me knowledge and methodology of computational fluid dynamics. Without him, my studies and simulations based on OpenFOAM would be really tough. Once again, I would like to thank him with my highest respect.

I also want to sincerely thank my co-supervisor Professor Muk Chen Ong for providing me the best conditions of CFD research at the University of Stavanger. During my master program in UiS, he selflessly gave me guidance and help in terms of study and life. He is one of the reasons why I chose to study in UiS. I will always be grateful for his help for the rest of my life.

Apart from my co-supervisors, I would like to express my appreciation to the University of Stavanger, Department of Mechanical and Structural Engineering and Materials Science for providing me with the opportunity and resources to study and carry out the research in Norway.

Finally, I would like to express my sincere thanks to my family for their mental and financial support during the two years. They are always the motivation and significance of my life and work.

Abstract

90-degree elbow structures such as pipelines with bends and rigid jumpers, are commonly used for flow transportation in subsea systems. The produced flow from the subsea wells is normally a multiphase flow which is a mixture of oil, water, gas polymer, and even rocks. The gas-liquid two-phase flow is a typical kind of multiphase flow conveyed in subsea systems, which has several flow regimes depending on different gas and liquid velocities. The transportation of gas-liquid two-phase flow in subsea pipeline systems can be a challenge because slug flow will occur with a specific combination of the gas and liquid velocities. For a slug flow, the gas phase coalesces into large-scale bubbles named Taylor bubbles and accumulates at the elbow sections, which will lead to large pressure fluctuation at these sections. With the peak of flow-induced forces acting on these sections, the pipelines will begin vibrating which may lead to even fatigue damage to the structures. In this thesis, the gas-liquid two-phase flow-induced forces on 90-degree elbow structures are numerically investigated by a one-way coupling method based on computational fluid dynamics (CFD) simulation and finite element analysis. The Reynolds numbers in the present simulations are in the range of $2.4\times10^5 \sim 3.2\times10^5$. The mesh convergence studies are performed to determine the optimal computational grid resolution. Subsequently, the validation studies are conducted, and compared with published experimental results. Then, the numerical simulations in the open-source CFD package OpenFOAM and open-source finite-element program CodeAster are carried out to study the gas-liquid two-phase flow in pipeline structures. The studied pipeline structures in the present study cover pipe with one or two 90-degree elbows, uniplanar jumper, and multiplanar jumper. It is concluded that the flow-induced forces mainly peak at the sections where the slugging phenomena happen or the Taylor bubbles are frequently formed. For the pipe with one or two elbows, increasing the number of fixed supports can effectively reduce the reaction forces fluctuation of fixed supports. Moreover, the maximum deformation occurs at the top of the jumpers, with an evident sinking of the middle component, where the material tensile capacity should be considered in the design of subsea jumpers. Additionally, specific descriptions of the multiphase flow field are provided including volume fraction contour, iso-surface plot, and secondary flow.

Keywords: Multiphase flow; Elbows; Rigid Jumpers; Numerical simulations; Flow-induced vibration; One-way coupling; Reaction forces.

Table of contents

Chapter1.
Introduction

1.1 Background

Since the second industrial revolution, the use of fuels like oil and natural gas has been essential to the rapid development of human society. In the 1940s, the first recorded well in the world was built in Lake Erie in the USA, which used a surface vertical X-mas tree. After two decades, Shel completed a subsea well in 1961, which was followed by Esso in 1964 [1]. At the initial stage, production tasks are conducted in the platform which also integrated other functions such as possessing, intervention, storage, and transportation. With the development of the offshore oil and gas industry, new solutions were proposed such as the subsea production system (SPS). In 1970, the SPS was first put into engineering practice as a full-scale system by Esso in the Gulf of Mexico. From then on, more and more subsea systems are developed to fulfill the diverse needs of offshore oil and gas projects. Depending on the reservoirs, the resources extracted from the subsea wells are a mixture of gas, liquid, and solid. The liquid phase could be water or petroleum, which is a complex mixture of naturally occurring hydrocarbon compounds found in rock and contains impurities such as Sulphur, oxygen, and nitrogen. The gas phase could be natural gas, which is a naturally occurring mixture of hydrocarbon gases that is highly compressible. The solid phase could be the coagulum of oil and gas or rock compositions. In brief, the flow from the subsea wells and transported in subsea systems is a typical multiphase flow.

Pipelines are fundamental components of subsea systems for transportation. From detailed subsea equipment like subsea jumpers to systems like riser systems, straight or curve pipelines are widely utilized in subsea systems. For a slim pipeline, a single-phase coming flow can trigger vortex shedding in the downstream region which will further lead to a vortex-induced vibration (VIV). Despite that, for a normal pipeline transporting multiphase flow inside, a gas-liquid two-phase flow can form long and large gas bubbles, which are called Taylor bubbles (1950) [2] and will also cause significant pressure fluctuations when they are moving inside the pipeline. When the amplitude of the pressure fluctuation becomes high or its frequency equals the natural frequency of the pipeline, the pipeline will begin vibrating which is called internal flow-induced vibration (FIV) for multiphase flow inside the pipeline. The investigation of gas-liquid two-phase flow-induced forces on 90-degree elbow structures is of great significance because of the wide utilization of 90-degree elbow structures in subsea systems and the widespread FIV in the process of operation.

From the 20th century to the present, the gas-liquid two-phase flow in pipelines and the excitation forces have been experimentally and numerically investigated by many researchers such as Yih and Griffith (1970) [3], Hara (1976) [4], Pettigrew et al. (1998) [5], Nakamura et al. (2005) [6], Pontaza and Menon (2011) [7] and Dinaryanto et al. (2017) [8]. Yih and Griffith (1970) [3] measured the steady and unsteady components of the momentum flux in a two-phase flow at the exit of a vertical pipe and

processed the momentum-flux data by standard random-vibration techniques. It was found that the variation of the momentum fluxes only has influences at low frequencies. Either the low void annular flow regime or the high void slug flow regime showed the highest levels of unsteady momentum fluxes. Nakamura et al. (2005) [6] performed experiments to investigate the flow-induced vibration of a large-diameter elbow piping based on random force measurement. They concluded that a flow velocity-dependent periodic phenomenon is detected in the rear region of the elbow and the largest flow-induced random vibration forces in the pipe are discovered in the region of flow separation downstream of the elbow. Pontaza and Menon (2011) [7] numerically studied the flow-induced vibration of subsea jumpers caused by internal two-phase flow. It was concluded that Modes 1 through 4 are related to the primary flow-induced vibration frequencies and that the gas volumetric void percentage of 55% under mid-life flow circumstances results in the largest stresses. More recently, Li et al. (2022) [9] studied the flow of gas and liquid and the associated vibration in a multiplanar jumper using numerical and experimental methods. They carried out the one-way coupling numerical simulations and validated the simulations against the experimental data based on the flow patterns and the flow-induced vibrations. It was demonstrated that the pressure variations and the vibration amplitudes are related to the gas content rate, mixture velocity, and the surface velocity of the gas and liquid.

1.2 Research objective

The main objective of this thesis is to investigate and analyze gas-liquid two-phase flow-induced forces on 90-degree elbow structures by carrying out numerical simulations based on a one-way fluid-solid coupling using OpenFOAM and CodeAster. The Computational Fluid Dynamics (CFD) tools have been widely applied for investigating the characteristics of gas-liquid two-phase flow in pipelines. Available CFD packages include Fluent, STAR-CCM+, and OpenFOAM. In the present study, the open-source CFD package, OpenFOAM-v2012, is employed to carry out the numerical simulations based on the finite volume method. The response analysis of pipeline structures is performed in the open-source Finite-Element program CodeAster. The characteristics and the excitation forces of gas-liquid two-phase flow in pipe bending have been experimentally investigated by many researchers such as Liu et al. (2012) [10] and Liu et al. (2014) [11]. The results of the present CFD simulations must be generally consistent with the experimental data and able to reproduce the experimental phenomena such as slug flow and Taylor bubbles, which is the validation studies included in Chapter 3 and 4. The subsequent objective is to gain a good understanding of the two-phase flow-induced forces of the pipeline with 90-degree elbows and its dynamic responses. With different types of inlets such as vertical and horizontal inlets, the formations of slug flow could be different, which can also affect the flow-induced forces. According to engineering requirements, the supports of the pipeline with elbows can also be various which will influence the results of dynamic response and are demonstrated in Chapter 3. Apart from the points mentioned above, the final aim is to investigate the two-phase flow-induced forces inside subsea jumpers. The goal of using different types of jumpers is to evaluate the different patterns of flow-

induced forces and the dynamic response between uniplanar and multiplanar jumpers which both are commonly used in real subsea engineering practice.

1.3 Thesis outline

The outline of the thesis is summarized as follows:

- Chapter 2: Basic theory on flow characteristics inside pipelines is introduced in general. The description of gas-liquid two-phase flow in pipelines, and the introduction of numerical methods for gas-liquid two-phase flow using OpenFOAM is also given.
- Chapter 3: Numerical simulations of gas-liquid two-phase flow-induced forces at pipeline with 90-degree elbows is performed, including the validation of the numerical models, results, and discussions of flow domain inside different pipelines, the flow-induced forces, and the induced dynamic response.
- Chapter 4: Numerical simulations of gas-liquid two-phase flow-induced forces at subsea jumpers are performed, including the validation of numerical models, results, and discussions of flow domain inside the subsea jumpers, the flow-induced forces, and the induced dynamic response.
- Chapter 5: Summary of the main findings and recommendations for future work.

References

1. https://www.viperinnovations.com/a-timeline-of-subsea-innovation-in-the-oil-gas-industry-1940-2000-part-one/

2. Davies R M, Taylor G I. The mechanics of large bubbles rising through extended liquids and through liquids in tubes. J. Proceedings of the Royal Society of London. Series A. Mathematical and Physical Sciences, 1950, 200, 375-390.

3. Yih T S, Griffith P. Unsteady momentum fluxes in two-phase flow and the vibration of nuclear system components. C. Proceedings of the International Conference on Flow-Induced Vibrations in Reactor System Components. 1970, 91-111.

4. Hara F. Two-phase flow induced vibrations in a horizontal piping system. J. Nippon Kikai Gakkai Ronbunshu, 1976, 42, 2400-2411.

5. Pettigrew M J, Taylor C E, Fisher N J, et al. Flow-induced vibration: recent findings and open questions. J. Nuclear Engineering and Design, 1998, 185, 249-276.

6. Nakamura T, Shiraishi T, Ishitani Y, et al. Flow-Induced Vibration of a Large-Diameter Elbow Piping Based on Random Force Measurement Caused by Conveying Fluid: Visualization Test Results. C. ASME Pressure Vessels and Piping Conference. 2005, 41898, 457-463.

7. Pontaza J P, Menon R G. Flow-induced vibrations of subsea jumpers due to internal multi-phase flow. C. International Conference on Offshore Mechanics and Arctic Engineering. 2011, 44397, 585-595.

8. Dinaryanto O, Prayitno Y A K, Majid A I, et al. Experimental investigation on the initiation and flow development of gas-liquid slug two-phase flow in a horizontal pipe. J. Experimental Thermal and Fluid Science, 2017, 81, 93-108.

9. Li W, Zhou Q, Yin G, et al. Experimental Investigation and Numerical Modeling of Two-Phase Flow Development and Flow-Induced Vibration of a Multi-Plane Subsea Jumper. J. Journal of Marine Science and Engineering, 2022, 10, 1334.

10. Liu Y, Miwa S, Hibiki T, et al. Experimental study of internal two-phase flow induced fluctuating force on a 90 elbow. J. Chemical Engineering Science, 2012, 76, 173-187.

11. Saidj F, Kibboua R, Azzi A, et al. Experimental investigation of air–water two-phase flow through vertical 90 bend. J. Experimental thermal and fluid science, 2014, 57, 226-234.

Chapter 2.
Literature study

2.1 Flow inside pipelines

A single-phase flow inside pipelines is a classical type of internal flow in fluid mechanics. In the following sections, relevant basic concepts and phenomena in pipelines will be introduced, including the pressure drop, the turbulent flow and the secondary flow.

2.1.1 Basic principles

In general, fluid flow is categorized as external and internal, depending on whether the fluid is forced to flow over a surface or within a conduit [1]. According to the relevant definition in fluid mechanics, pipe flow is a typical internal flow regardless of the geometry of the pipelines. The restricting surfaces, as the pipe wall in pipe flow, direct the flow from an arbitrarily specified input state to an equally arbitrary output state. During this process, there will be a pressure difference between the input and output of the pipe which is called pressure drop. Normally, the pressure drop happens when frictional forces are caused by the flow resistance acting on a fluid as it passes through a conduit. Some of the hydraulic energy of the fluid is converted to thermal energy by the friction. Because the thermal energy cannot be transformed back into hydraulic energy, the fluid experiences a pressure drop, which is required for energy conservation. The pressure drop in laminar flow is expressed as:

$$\Delta P = \frac{32\mu L V_{avg}}{D^2}, \tag{2.1}$$

where μ is the dynamic viscosity of the fluid, L is the pipe length, D is the pipe diameter and V_{avg} is the average velocity of the fluid. For fully developed laminar pipe flow, V_{avg} equals half of the maximum velocity. Moreover, pipe flow also follows the conservation of mass, which means that the total mass of the flow at the inlet equals the total mass at the outlet.

Since the pipe flow is confined by solid surfaces, the fluid velocity in a pipe varies from zero at the wall because of the no-slip condition to a maximum at the pipe center. The flow region close to the wall where the viscosity significantly affects is called the boundary layer which is caused by the no-slip condition. Apart from the near-pipe-wall shear flow of the boundary layer, surface drag is another consequence of the no-slip condition, which is the force a fluid acts on a surface in the flow direction [1].

To better descript the flow inside pipelines, it is of great significance to introduce the hydrodynamic entrance region and the hydrodynamically fully developed region. Figure 2.1 shows how the fluid flow normally develops in a pipe. A pipe flow can be divided into two regions: the boundary layer region where the viscosity dominates and the velocity significantly changes and the irrotational flow region in the core part of the pipe where there is almost no friction effect and the velocity remains unchanged in the radial direction. The hydrodynamic entrance region is the area between the pipe inlet

and the point where the velocity profile is fully developed. The area beyond the hydrodynamic entrance region where the velocity profile is fully developed and remains constant is called the hydrodynamically fully developed region. The wall shear stress is relevant to the slope of the velocity profile at the surface. At the inlet where the boundary layer thickness is the smallest, the wall shear stress is the highest. With the development of the flow in the hydrodynamic entrance region, the wall shear stress gradually decreases until the hydrodynamically fully developed region where the wall shear stress becomes constant. Thus, the pressure decreases in the flow direction and the pressure drop becomes higher in the hydrodynamic entrance region. Therefore, the fluid will accelerate at the pipe center and slow down adjacent to the pipe wall according to the mass conservation.

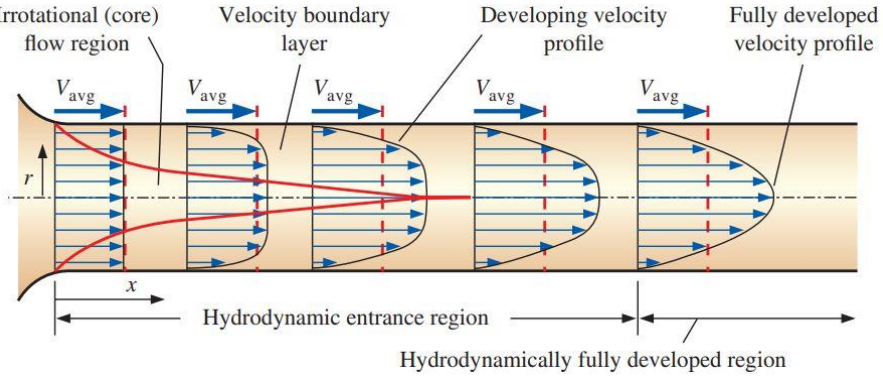

Figure 2.1. The development of the velocity boundary layer in a pipe from Cengel and Cimbala (2014) [1].

2.1.2 Turbulence and turbulence modeling

In the 1880s, Osborne Reynolds experimentally found that the flow regime mainly depends on the ratio of inertial forces to viscous forces in the fluid, which is called the Reynolds number. In a circular pipe, the Reynolds number is given as:

$$Re = \frac{V_{avg}D}{\nu} = \frac{\rho V_{avg}D}{\mu}, \tag{2.2}$$

where $\nu = \mu/\rho$ is the kinematic viscosity of the fluid, ρ is the density of the fluid, μ is the dynamic viscosity of the fluid, D is the pipe diameter, V_{avg} is the average velocity of the fluid. When the Reynolds number is large, the inertial forces are dominant and the viscous forces are too small to prevent the irregular and strong fluctuation of the fluid. The flow in this regime is called turbulent flow. While at a small Reynolds number, viscous forces can suppress the fluctuation of the fluid and maintain the fluid coordinated. The flow at this state is called laminar flow. Figure 2.2 presents the different velocity profiles of laminar and turbulent flow in a fully developed pipe flow respectively. From the experiment performed by Reynolds (1883) [2], the transition from laminar flow to turbulent was observed. In reality, a circular pipe flow is defined as laminar for $Re \leq 2300$, turbulent for $Re \geq 4000$, and transitional in between. $Re_{cr} = 2300$ is called the critical Reynolds number at which the flow

becomes turbulent. In a transitional flow, the flow shifts randomly between laminar and turbulent flow.

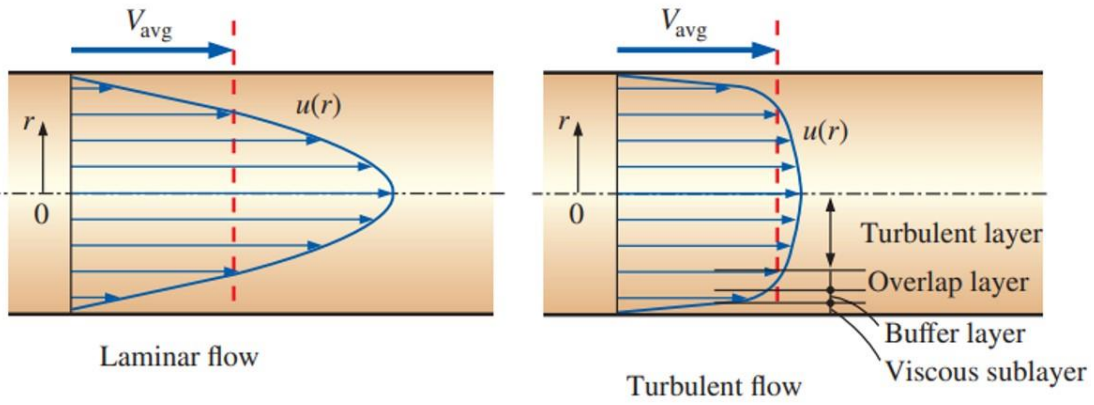

Figure 2.2. The velocity profiles of laminar and turbulent flow in a fully developed pipe flow from Cengel and Cimbala (2014) [1].

Turbulence modeling is the building and application of a mathematical model to predict the influence of the turbulence in fluid dynamics. The existing commonl used turbulence models are closure relationship between the Reynolds stress and the strain of the mean flow used in CFD simulations to predict the evolution of turbulent flows. In engineering applications, there are many turbulence models such as $k-\varepsilon$ model, $k-\omega$ model, $k-\omega$ SST model and Reynolds stress equation model (RSM). The following is a brief introduction of three commonly used models:

- $k-\varepsilon$ (k-epsilon): $k-\varepsilon$ (k-epsilon) turbulence model is the most commonly used model in CFD simulations to investigate the mean flow characteristics under turbulent flow conditions. This two-equation model provides a general description of turbulence using two partial differential equations (PDEs). The standard $k-\varepsilon$ model yields good results for turbulent shear flows, especially at the free-stream boundary. However, this model is unable to predict accurately flows with adverse pressure gradients and extra strains [3].
- $k-\omega$ (k-omega): $k-\omega$ (k-omega) turbulence model is a common two-equation model in CFD for solving the Reynolds-averaged Navier–Stokes equations (RANS equations). This model behaves very accurately in predicting separated flows [4]. Compared with the standard $k-\varepsilon$ model, the $k-\omega$ model performs more accurately for boundary layers with adverse pressure gradients and can be easily integrated into the viscous sub-layer without any additional damping functions [3].
- $k-\omega$ SST (Menter's shear stress transport): $k-\omega$ SST turbulence model is a robust two-equation eddy-viscosity turbulence model in CFD, which combines the $k-\omega$ and the $k-\varepsilon$ models. For the region close to the walls, the $k-\omega$ model is applied, while in the free-stream flow region such as the center part of the pipe flow, the $k-\varepsilon$ model is used [5].

2.1.3 Secondary flow in elbows

Piping systems normally involve components which change the direction and are called bends or elbows. Figure 2.3 concisely displays a secondary flow in a pipe elbow. When the flow accesses an elbow, a cross-stream pressure gradient is generated to balance the inward acceleration. Consequently, a secondary flow develops, with the faster fluid moving to the outside and the slower fluid to the interior of the curve. It was found that the pressure loss in a curved pipe is higher than that in a straight pipe of the same length. Rowe (1970) [7] concluded that this excess pressure loss is caused because the secondary flow continuously sweeps the faster-moving fluid towards areas near the pipe wall where it is retarded. Besides, he found that in the long bend, a mechanism is generated by the formation of total pressure gradients that are opposite in sign from those at the start of the bend and the subsequent production of vorticity with an opposite rotational sense. This mechanism prevents the secondary flow from increasing indefinitely and allows the flow to fully develop.

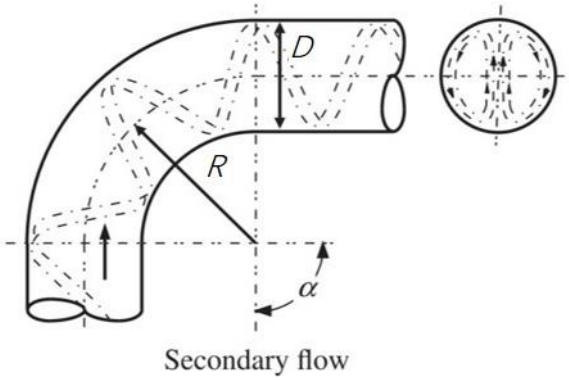

Figure 2.3. Secondary flow phenomenon in a 90-degree pipe elbow from Rennels and Hudson (2012) [6].

2.2 Multiphase flow

In fluid mechanics, multiphase flow refers to the flow in which more than one thermodynamic phase exists. These phases may consist of one chemical material (such as liquid water and water vapor), or several different chemical materials (such as oil and gas). A phase is defined as a continuous phase if it occupies an uninterrupted space in the flow. In contrast, a phase that occupies an interrupted space in the flow is classified as dispersed phase. Moreover, multiphase flow can be divided into dispersed flow and separated flow based on how the phases are distributed in the flow. In a dispersed flow, discrete particulates, such as small gas bubbles or droplets, are distributed within a continuous phase. While a separated flow consists of more than one continuous phase separated by interfaces. In this study, a gas-phase two-phase flow is the main concern, especially under the condition of slug flow, which will be introduced in the following sections.

2.2.1 Gas-liquid two-phase flow

Gas-liquid two-phase flow as a typical multiphase flow has been widely concerned and studied for many years. Depending on the fluid properties, flow rates and pipe geometry, different flow regimes will occur. Because the present flow regimes are mostly determined by experimental observation, the definition of flow regimes is varied based on the researchers' cognitions. However, most researchers have an agreement on some flow regimes which are commonly observed in experiments. The sketches of flow regimes in horizontal and vertical pipes are visualized in Figure 2.4. The flow regimes of gas-liquid flow in a horizontal pipe are briefly introduced below:

- **Bubble flow:** At this flow regime, the gas phase normally exists as bubbles moving with a continuous liquid phase. The size of the gas bubbles is non-uniform and may change by accumulating. Because of the gravity, the bubbles as a lighter phase in a horizontal pipe tend to move attaching to the upper side of the pipe.
- **Slug flow:** For a slug flow, the gas phase is separated as large gas pockets which are called Taylor bubbles [8]. Taylor bubbles generally have bullet shapes and occupy most area of the cross-section, moving with the continuous liquid phase.
- **Plug flow:** Plug flow as a kind of intermittent flow shares several similarities with slug flow including Taylor bubbles moving with continuous liquid phase. An obvious difference between them is the size of Taylor bubbles. Compared with slug flow, the Taylor bubbles in plug flow are smaller and occupy less area of the cross-section.
- **Annular flow:** Annular flow is the regime when the liquid phase moves forward as a continuous annular film on the pipe wall. The gas phase accumulates at the central cross-section with some liquid droplets.
- **Stratified flow:** When the phase velocities are low, the gas phase goes up while the liquid phase sinks due to the density distinction. The interface between them is continuous and clear.
- **Disperse flow:** Disperse flow normally happens when the liquid velocity is high. Therefore, the gas bubbles in dispersed flow are considerably tiny and evenly dispersed with minor changes in size.
- **Wavy flow:** Similar to stratified flow, the stratification between the gas phase and liquid is also obvious while the interface in wavy flow is fluctuating like a wave and the amplitude of the fluctuation is notable.

As shown in Figure 2.4 (b), most of the flow regimes in a vertical pipe are similar to those in a horizontal pipe apart from churn flow. For churn flow, the gas phase also coalesces and generates bubbles with irregular shapes. The size of bubbles in churn flow is normally not as large as Taylor bubbles.

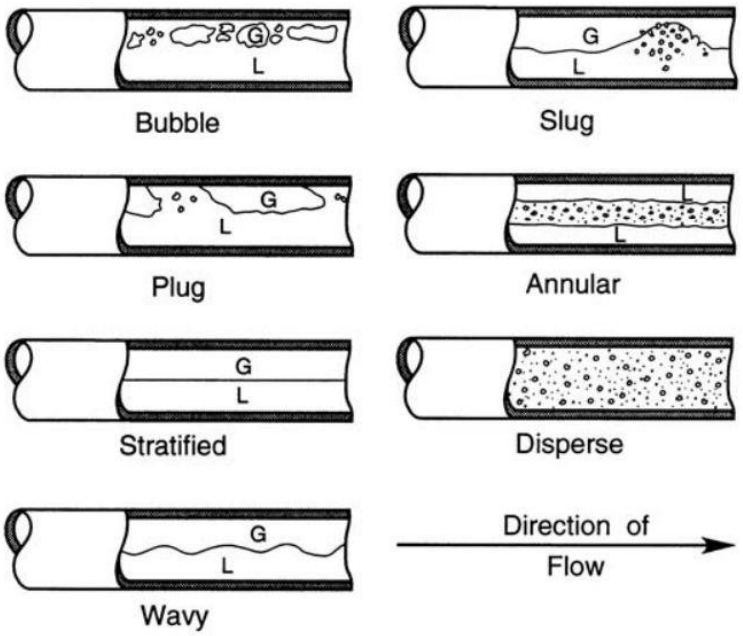

(a) In a horizontal pipe

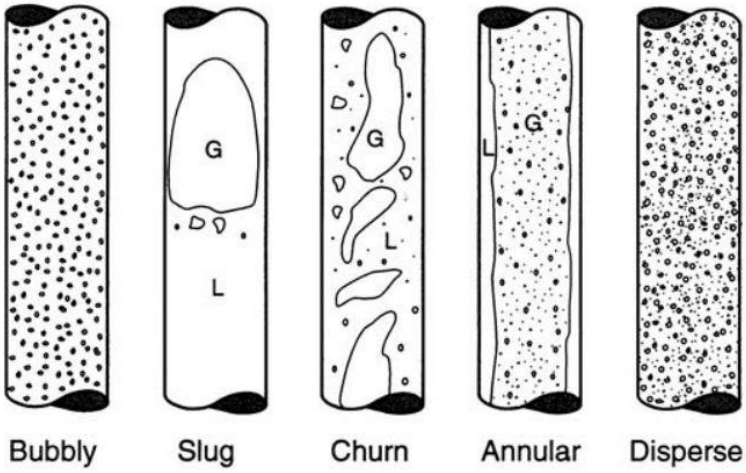

(b) In a vertical pipe

Figure 2.4. Sketches of flow regimes for gas-liquid two-phase flow in horizontal and vertical pipes. Adapted from Weisman (1983).

2.2.2 Flow pattern maps

In the research of gas-liquid two-phase flow, superficial velocity is often used which is defined as an artificial velocity computed as if the given phase is the only one in a cross-section area. Researchers have been able to establish flow pattern maps for specific combinations of geometry and fluid compositions by collecting data such as superficial velocities [9], superficial momentum fluxes [10], or volumetric flux (Figure 2.5). A flow pattern map generally illustrates the transition boundary between included flow regimes and the dimensional parameters that limit each flow pattern. Although the flow pattern maps are easy to use, they are usually limited to particular geometries like

vertical pipe or horizontal pipe. Moreover, the method of developing the flow pattern maps relies on experimental data, which are diverse for different researchers. Particularly when the flow pattern is close to the boundary of two flow regimes in the flow pattern map, practical experiment results can be different from the targeted flow regimes. Therefore, there are no existing dimensionless flow pattern maps that can cover the full parametric boundaries of the flow. Nevertheless, flow pattern maps are still useful tools in the investigation of gas-liquid two-phase flow.

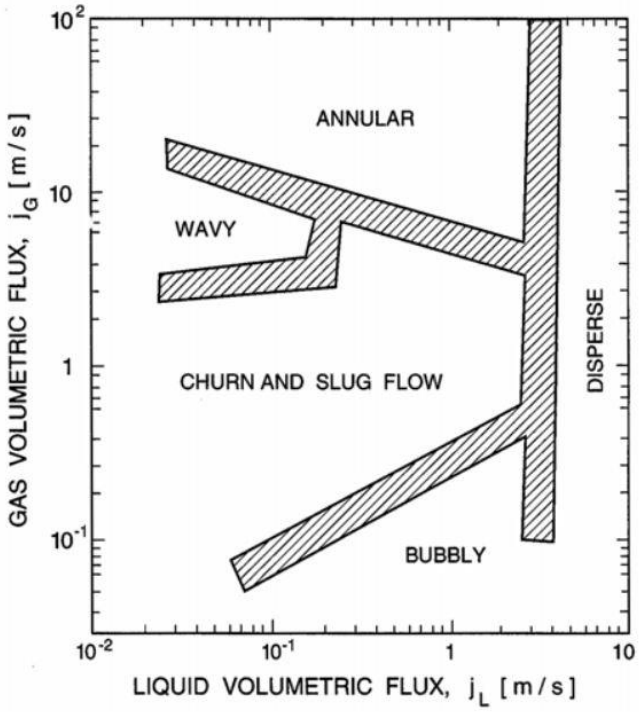

Figure 2.5. A flow pattern map for a gas-liquid two-phase flow in a vertical pipe. Adapted from Weisman (1983).

2.3 Available solvers for two-phase flow in OpenFOAM

For the CFD simulations in OpenFOAM, an appropriate solver is of great importance which will significantly affect the simulation results. An overall case directory structure of a typical OpenFOAM case is shown in Figure 2.6. The '0' directory contains the individual files for specific fields such as velocity, pressure and volume fraction of water at 0 second (the beginning time is adjustable). A 'constant' directory includes a subdirectory 'polyMesh' describing the case mesh and files specifying physical properties for the case. A 'system' directory contains the setup of parameters associated with the solution procedure itself, which includes at least 3 files: 'fvSchemes', 'fvSolution' and'controlDict'. The 'fvSchemes' file is associated with the discretisation schemes used in the solution at the run-time. The 'fvSolution' file includes the equation solvers, tolerances and other algorithm controls using during the case running. The 'controlDict' is the file where the control commands of the solvers, start & end time and data output are listed. With the rapid development of CFD

technology, plenty of solvers are developed for the simulations of multiphase flow in OpenFOAM including twoPhaseEulerFoam, interFoam, interIsoFoam. Among these various solvers, interFoam is the most widely utilized solver for gas-liquid two-phase flow, while interIsoFoam as a modification of interFoam applying isoAdvector method [11], is increasingly used in two-phase flow simulations. In the next sections, these two solvers will be mainly introduced on how to capture the interface between the gas and liquid phase.

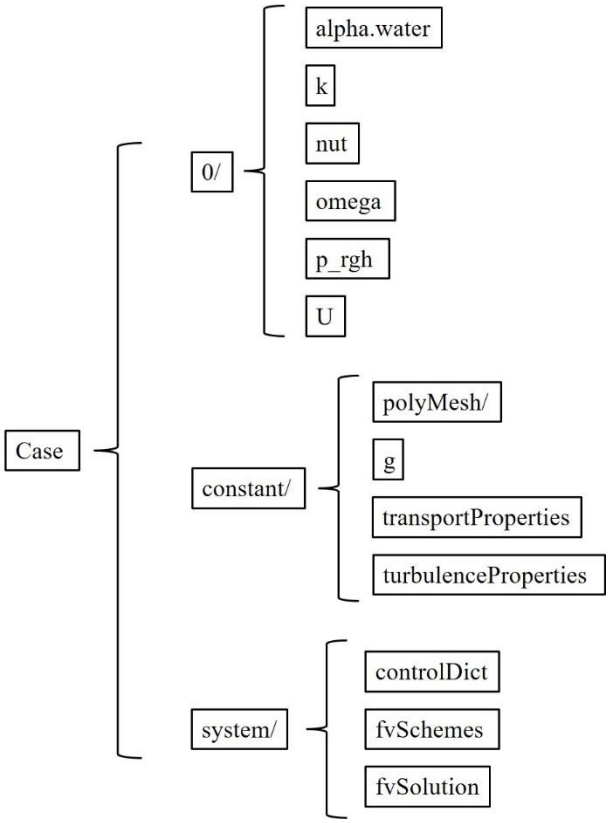

Figure 2.6. Case directory structure of interIsoFoam solver in OpenFOAM.

2.3.1 interFoam

In OpenFOAM, interFoam is a popular two-phase flow solver with the combination of the volume of fluids (VOF) method and Multidimensional Universal Limiter for Explicit Solution (MULES) scheme. The governing equations of VOF model including the continuity equation, the momentum equation and the advection equation, are specifically given in the methodology of Chapter 3 and 4. Thus, in this section the MULES scheme is mainly demonstrated. VOF model has a main defect that the interface is smearing and not clear enough. Briefly, the interface will be presented as a zone where the volume fraction α progressively shifts from 1 to 0 without the use of any further surface capture techniques. Then, the cells having the volume fraction α of both phases will be filled with a uniform combination of the two phases instead of a sharp interface dividing the fractions of each phase inside the cell. For this reason, MULES scheme is utilized in interFoam to improve the sharpness of the interface.

The advection equation in VOF model is given as:

$$\frac{\partial \alpha}{\partial t} + \boldsymbol{u} \cdot \nabla \alpha = 0, \tag{2.3}$$

where α is the volume fractions of the phases and $\boldsymbol{u}$ is the velocity vector of the fluid. In the above Equation (2.3), the second term is known as the advection term. In MULES scheme, the advection term in Equation (2.3) is modified to compress the surface and lessen the smearing of the interface [12]. Firstly, Equation (2.3) is rewritten to integral form as below:

$$\int_{\Omega_i} \frac{\partial \alpha}{\partial t} dV + \int_{\partial \Omega_i} \alpha \boldsymbol{u} \cdot \boldsymbol{n} \, dS = 0, \tag{2.4}$$

where Ω_i represents each cell element, $\partial \Omega_i$ is the cell boundary, and $\boldsymbol{n}$ is the normal vector of the cell boundary.

Then, the Equation (2.4) is discretized, with the second term written as a sum over each face of the cell and the first term written using any time-stepping scheme named forward Euler:

$$\frac{\alpha_i^{n+1} - \alpha_i^n}{\Delta t} = -\frac{1}{|\Omega_i|} \sum\nolimits_{f \epsilon \partial \Omega_i} (F_u + \lambda_M F_c)^n, \tag{2.5}$$

where λ_M is the delimiter having the value of 1 at the surface and 0 elsewhere, F_u and F_c are the advective fluxes respectively given as:

$$F_u = \Phi_f \alpha_{f,upwind}, \tag{2.6}$$

and

$$F_c = \Phi_f \alpha_f + \Phi_{rf} \alpha_{rf} (1 - \alpha)_{rf} - F_u, \tag{2.7}$$

where Φ_f is volumetric face flux. For the subscripts here, f means that the quantity is evaluated as the face and upwind denotes that an upwind scheme is applied. Φ_{rf} is shown as:

$$\Phi_{rf_c} = min\left(C_\alpha \frac{|\Phi_f|}{|\boldsymbol{S}_f|}, max\left[\frac{|\Phi_f|}{|\boldsymbol{S}_f|}\right]\right)(\boldsymbol{n}_f \cdot \boldsymbol{S}_f), \tag{2.8}$$

where C_α is a specified parameter for decreasing interface smearing, $\mathbf{S}_f$ is the cell face area vector and $\boldsymbol{n}_f$ is the normal vector of the face-centered interface.

α_{rf} in Equation (2.7) is calculated by:

$$\alpha_{rf} = \alpha_P + \frac{\alpha_N - \alpha_P}{2}\left[1 - \Psi(\Phi_f)(1 - \lambda_{\alpha r})\right], \tag{2.9}$$

where N and P respectively represent the upwind and downwind terms, $\lambda_{\alpha r}$ is a limiter and Ψ denotes a step function which returns the value of 1 where the volumetric face flux i is positive and -1 where it is negative.

In general, for $\lambda_M = 0$ which means away from the interface, the sum of advective fluxes in Equation (2.5) becomes only F_u, which is computed by a. upwind scheme. For $\lambda_M = 0$ which means at the interface, the sum of advective fluxes in Equation (2.5) is given as a combination of a higher order scheme, which provides a more precise advection at the interface and less surface smearing. By this way, the computational efficiency away from the interface is improved and the numerical diffusion at the interface is lessened.

2.3.2 interIsoFoam

Based on interFoam, the solver interIsoFoam combines VOF method with a newly

developed scheme named isoAdvector, which is established aiming to improve the interface capturing compared with interFoam. In isoAdvector scheme, the concept of isosurfaces is employed to more accurately determine face fluxes for the cells comprising the interface [13]. At first, the phase fraction $\alpha_i(t)$ in cell i at time t is given by a function $H(x,t)$ describing the continuous field of $\alpha_i(t)$:

$$\alpha_i = \frac{1}{V_i}\int_{\Omega_i} H(x,t)\, dV, \tag{2.10}$$

where V_i is the cell volume and Ω_i is denoted as each cell. Moreover, to calculate the phase fractions at the next time step, The momentum flux of over each cell face is integrated in time and summed together as the following:

$$\alpha_i(t+\Delta t) = \alpha_i(t) - \frac{1}{V_i}\sum_{j\in B_i} s_{ij}\int_t^{t+\Delta t}\int_{F_i} H(x,\tau)\boldsymbol{u}(x,\tau)\, dS d\tau, \tag{2.11}$$

where B_i is the set of all faces F_i in cell i, s_{ij} is employed to direct the flux out from the cell, τ is the parameter of integration in the timestep and dS is the differential area vector pointing out of the volume. s_{ij} is set as +1 or -1 to ensure that $s_{ij}dS$ always points out of the cell even when the direction of face j makes dS point inside the cell. The double integration in Equation (2.11) can be substituted by $\Delta V_j(t,\Delta t)$ as below, which describes the total volume of a phase across face j during one time step:

$$\int_t^{t+\Delta t}\int_{F_i} H(x,\tau)\boldsymbol{u}(x,\tau)\, dS d\tau = \Delta V_j(t,\Delta t), \tag{2.12}$$

In isoAdvector scheme, this is the main estimated quantity which using α_i, u_i and Φ_j. Φ_j is the face flux across face j given as below:

$$\Phi_j = \int_{F_i} \boldsymbol{u}(x,\tau)\, dS, \tag{2.13}$$

According to the results from Roenby et al. (2016) [13], the computational efficiency and accuracy in isoAdvector scheme are both better than MULES. Besides, isoAdvector scheme can function with higher Courant numbers compared with MULES.

References

1. Cengel, Y.A. and Cimbala, J.M., 2014. Fluid Mechanics Fundamentals and Applications, Third Edition. (New York: McGraw-Hill), 1031.
2. Reynolds, O., 1883. XXIX. An experimental investigation of the circumstances which determine whether the motion of water shall be direct or sinuous, and of the law of resistance in parallel channels. Philosophical Transactions of the Royal society of London, 174, 935-982.
3. Argyropoulos C D, Markatos N C. Recent advances on the numerical modelling of turbulent flows. J. Applied Mathematical Modelling, 2015, 39, 693-732.
4. Wilcox D C. Formulation of the kw turbulence model revisited. J. AIAA journal, 2008, 46, 2823-2838.
5. Menter F R. Two-equation eddy-viscosity turbulence models for engineering applications. J. AIAA journal, 2002, 40, 254-266.
6. Rennels, D.C. & Hudson, H.M., 2012. Pipe flow: A practical and comprehensive guide. John Wiley & Sons.
7. Rowe M. Measurements and computations of flow in pipe bends. J. Journal of Fluid Mechanics, 1970, 43, 771-783.
8. Davies R M, Taylor G I. The mechanics of large bubbles rising through extended liquids and through liquids in tubes. J. Proceedings of the Royal Society of London. Series A. Mathematical and Physical Sciences, 1950, 200, 375-390.
9. Sternling V C. Two-phase flow theory and engineering decision. C. Award lecture presented at AIChE annual meeting. 1965.
10. Hewitt G F, Roberts D N. Studies of two-phase flow patterns by simultaneous x-ray and flast photography. R. Atomic Energy Research Establishment, Harwell, England (United Kingdom), 1969.
11. Olsson E, Nilsson H. A Description of IsoAdvector–A Numerical Method for Improved Suface Sharpness in Two-Phase Flows. J. Edited by Nilsson, H, 2017.
12. Deshpande S S, Anumolu L, Trujillo M F. Evaluating the performance of the two-phase flow solver interFoam. J. Computational science & discovery, 2012, 5, 014016.
13. J. Roenby, H. Bredmose, and H. Jasak. A computational method for sharp interface advection. Royal Society Open Science 11.3 (2016).

Chapter 3.
Numerical simulations of gas-liquid two-phase flow induced forces at pipeline with 90-degree elbows

Abstract

Pipeline systems are widely used in subsea oil and gas industry to transport multiphase flow, which is a mixture of oil, gas and water produced from offshore wells. For the multiphase flow involving both gas and liquid or different liquids, slug flow is a typical flow pattern, where the gas phase will merge into large and long bubbles and move with liquid. When the bubbles pass through elbows along the pipeline, they will cause flow-induced pressure fluctuations. This pressure fluctuation can result in pipeline vibrations. If the frequency of the excitation force is close to the natural frequency of the pipeline, the slug flow can lead to resonance or even fatigue damage to the pipeline system. In the present study, numerical simulations are carried out to investigate the characteristics of gas-liquid two-phase flow and its induced excitation forces acting on pipelines with 90-degree elbows. The mesh convergence study is conducted to determine the optimal computational grid resolution. Then, the validation study is conducted against previous published experimental data. The validated numerical model is then applied to investigate four different bend pipe configurations. It is found that the excitation forces along the pipe mainly peak at the elbow sections for all pipe configurations. Different number of fixed supports are applied for pipelines and it is found that increasing the number of fixed supports can ease the fluctuation of reaction forces. Moreover, the time series of the two-phase flow-induced forces for different pipeline configurations with different numbers of fixed supports are presented and summarized, which can be utilized for further fatigue analysis or resonance analysis.

Keywords: Multiphase flow; Elbows; Numerical simulations; Flow induced vibration; Excitation forces, Reaction forces.

3.1 Introduction

In offshore industries, pipeline systems are utilized as significant components for flow transportation such as oil and gas. Many pipelines used in subsea environment are rarely straight due to the seabed geology and configuration requirement. 90-degree elbows, as one of the most basic types of pipeline components, are commonly utilized in subsea pipeline systems and subsea equipment such as manifolds and compressors. Usually, a secondary flow will be induced after the pipe bending part which will cause a distorted pipe flow. Multiphase flow such as gas-liquid two-phase flow in pipelines, displays different flow states including bubble flow, slug flow, churn flow and annular

flow. In a specific range of superficial gas and liquid velocities (one phase's superficial velocity is defined as an artificial velocity computed as if the given phase is the only one in a cross-section area), the flow can undergo transient states named slug flow and churn flow. In the slug flow state, long gas bubbles are formed and move with the liquid, which is called Taylor bubble flow for a vertical pipeline. As for the churn flow state, the gas bubbles become smaller, and the flow becomes more chaotic compared with those in the slug flow. Moreover, the two-phase flow will cause fluctuating pressure acting on the wall of the pipeline when large gas bubbles move with the liquid in these two states. This pressure fluctuation can lead to a flow-induced-vibration (FIV) and eventually fatigue damage to the pipelines. Therefore, it is of great significance to investigate the gas-liquid flow characteristics in 90-degree elbows for subsea engineering to achieve a safety design of the pipeline systems. A great number of experimental studies on multiphase flow through different pipe configurations have been conducted. Yih and Griffith (1967) [1] investigated the fluctuation of momentum fluxes in a vertical pipe. They concluded that for the liquid-gas two-phase flow, the unsteady fluctuation of momentum fluxes is significant in the low-frequency range, and FIV can occur because of these unsteady momentum fluxes. Hara (1976) [2] performed experiments to study the multiphase flow-induced vibration mechanism in a horizontal pipe and found that the excitation mechanism depends on different parameters such as the superficial gas and liquid velocities. Pettigrew et al. (1994) [3] introduced several fundamental FIV mechanisms for two-phase pipe flows, including the fluid elastic instability, the traveling pressure wave and random excitation. Moreover, Pettigrew et al. (1998) [4] summarized some new findings and discussed some of the opening questions regarding vibration excitation and damping mechanisms. Tay and Thorpe (2004) [5] investigated the effects of fluid properties inside the pipe such as surface tension and the viscosity of the fluid on the exciting forces acting on pipe bends caused by two-phase slug flow. Riverin et al. (2006) [6] measured the excitation forces of gas-liquid two-phase flow in pipe elbows and proposed the relationship between these forces and the local void fraction of the gas inside the liquid flow. More recently, experiments of two-phase flow in a 90-degree elbow were performed by Liu et al. (2012) [7] and Miwa et al. (2016) [8]. Liu et al. (2012) [7] studied the two-phase flow-induced forces on a 90-degree elbow with a pipe internal diameter of $52.5\,mm$ and a radius curvature of $76.2\,mm$ for the bend part. It was concluded that the elbow has a damping effect to suppress the high frequency of these excitation forces. Miwa et al. (2016) [8] developed a new numerical model to predict the stratified two-phase flow-induced forces in a 90-degree pipe bend and the predicted results by using this model showed a good agreement with their experimental data.

Apart from experiments, numerical simulations were also carried out to investigate the two-phase pipe flow. The volume of fluid (VOF (1981) [9]) methods were commonly employed to capture the interface between the gas and liquid phase in the two-phase flow. Hossain et al. (2019) [10] conducted numerical simulations of gas-liquid flow covering several flow states from bubble flow to annular flow and obtained the excitation forces by using momentum conservation. Wang et al. (2018) [11] investigated the FIV caused by severe slug flow using numerical simulations and

conducted a further dynamic response analysis based on a one-way coupling between the two-phase flow and the pipeline structure. It was found that the dominant frequencies of fluid force in the study are distributed near the first-order natural frequency of the structure and the amplitude of the FIV of the pipeline systems can be suppressed by using elastic foundations. Mohmmed et al. (2020) [12] performed numerical simulations based on a one-way fluid-structure coupling of gas-liquid slug flow in a horizontal pipe and validated the numerical model against experimental data. It was concluded that for constant superficial liquid velocity, the maximum excitation stress acting on the pipe wall increases with longer slugging lengths of the gas bubbles and higher slug velocity.

The objective of the present study is to investigate the characteristics of gas-liquid two-phase slug flow and the flow-induced excitation force acting on different pipelines with 90-degree elbows. The paper is organized as follows. The governing equations of the gas-liquid two-phase flow are introduced in Section 2. The computational setups are given in Section 3, including the numerical simulation models in OpenFOAM and Code Aster. The flow characteristics of the gas-liquid flow and the structural responses due to the flow-induced excitation forces are shown in Section 4. Finally, conclusions are made in Section 5.

3.2 Methodology

The Computational Fluid Dynamics (CFD) techniques have been commonly utilized to investigate the characteristics of gas-liquid two-phase flow. In the present study, the VOF model is used to capture the interface between the gas and the liquid flow and the $k-\omega$ Shear-Stress Transport ($k-\omega$ SST) model is adopted to resolve the turbulence stress.

3.2.1 VOF model

In the VOF model, the same momentum equations are shared by the two phases of the gas and the liquid. The tracking of the interface between the gas and liquid phase is achieved by using the continuity equation [13]. The governing equations of the VOF model are shown below:

The continuity equation of the fluids is given as:

$$\frac{\partial \rho}{\partial t} + \nabla \cdot (\rho \boldsymbol{u}) = 0, \tag{3.1}$$

where ρ is the density, t is the time and $\boldsymbol{u}$ is the velocity vector of the fluid.
The momentum equations of the fluids are given as:

$$\frac{\partial (\rho \boldsymbol{u})}{\partial t} + \nabla \cdot (\rho \boldsymbol{u}\boldsymbol{u}) = -\nabla \cdot P + \nabla \cdot \mu(\nabla \boldsymbol{u} + \nabla \boldsymbol{u}^T) - F, \tag{3.2}$$

where P is the pressure in the flow field, μ is the dynamic viscosity of the fluid and F is the surface tension force.

To track the interface between two phases, an additional volume continuity equation for each phase is solved and shown below:

$$\frac{\partial \alpha_i}{\partial t} + \boldsymbol{u} \cdot \nabla \alpha_i = 0, \tag{3.3}$$

where i represents each phase component.

The volume fractions of the two phases satisfy the equation:

$$\sum_{i=1}^{2} \alpha_i = 1, \tag{3.4}$$

The density ρ of the fluids can be represented as:

$$\rho = \sum_{i=1}^{2} \alpha_i \rho_i, \tag{3.5}$$

where ρ_1 represent the density of the liquid phase (also denoted as $\rho_l = 10^3\ \mathrm{kg/m^3}$) and ρ_2 represent the density of the liquid phase (also denoted as $\rho_g = 1\ \mathrm{kg/m^3}$).

The surface tension force F between the gas and liquid phase in Equation (3.2) as a source term is calculated by the continuum surface force (CSF (1992) [14]) model given as:

$$F = \sigma \left[\frac{\rho k_1 \nabla s_1}{\frac{(\rho_l + \rho_g)}{2}} \right], \tag{3.6}$$

where σ represents the surface tension coefficient and k_1 represents the surface curvature.

3.2.2 Turbulence model

The $k-\omega$ SST model is utilized to resolve the turbulence stress for both liquid and gas phases in the present study. This turbulence model combines the $k-\omega$ and the $k-\varepsilon$ models. For the region close to the walls, the $k-\omega$ model of Wilcox (1998) is applied, while in the free-stream flow region such as the center part of the pipe flow, the $k-\varepsilon$ model of Jones and Launder (1973) is used. The turbulence viscosity is calculated by:

$$\mu_t = a_1 \frac{\rho k}{max(a_1 \omega, SF_2)} \tag{3.7}$$

The turbulent kinetic energy k is obtained by solving the equation of:

$$\frac{\partial (\rho k)}{\partial t} + \nabla \cdot (\rho k \boldsymbol{u}) = \nabla \cdot \left[\left(\mu + \frac{\mu_t}{\sigma_k} \right) \nabla k \right] - \beta^* \rho k \omega + S_k, \tag{3.8}$$

where S_k is shear production term given by:

$$S_k = \mu_t \nabla \boldsymbol{u} \cdot (\nabla \boldsymbol{u} + (\nabla \boldsymbol{u})^T). \tag{3.9}$$

The turbulence specific dissipation rate ω is obtained by solving the equation of:

$$\frac{\partial (\rho \omega)}{\partial t} + \nabla \cdot (\rho \omega \boldsymbol{u}) = \nabla \cdot \left[\left(\mu + \frac{\mu_t}{\sigma_{\omega,1}} \right) \nabla \omega \right] + \gamma_2 \left(2\rho S_{ij}^2 - \frac{2}{3} \rho \omega \frac{\partial u_i}{\partial x_j} \delta_{ij} \right) - \beta_2 \rho (\omega)^2 + 2 \frac{\rho}{\sigma_{\omega,1} \omega} \frac{\partial k}{\partial x_k} \frac{\partial \omega}{\partial x_k} \tag{3.10}$$

The set of governing equations of $\mathrm{k}-\omega$ SST model is implemented and solved in the open-source CFD software package OpenFOAM. Moreover, other constants such as α_{k1}, α_{k2}, $\alpha_{\omega 1}$, $\alpha_{\omega 2}$, β_1, β_2, γ_1, γ_2, β^*, a_1, b_1, c_1 can be found in Menter et al. (2003) [15].

3.2.3 Structural model

Since the diameter of the pipeline is small compared with the length of the pipeline in the present study, the pipeline structure can be modelled as the Euler-Bernoulli beam. The gas-liquid two-phase flow-induced excitation forces acting on the walls of the pipe and the induced structural responses are calculated in a three-dimensional coordinate system. The structural dynamic equation is given by:

$$\mathbf{M}\ddot{\mathbf{u}}(t) + \mathbf{C}\dot{\mathbf{u}}(t) + \mathbf{K}\mathbf{u}(t) = \mathbf{P}(t) \tag{3.11}$$

where $\mathbf{M}$, $\mathbf{C}$ and $\mathbf{K}$ denote mass, damping and stiffness matrices; while $\ddot{\mathbf{u}}(t)$, $\dot{\mathbf{u}}(t)$ and $\mathbf{u}(t)$ denote accelerations, velocities and displacements vectors, respectively. $\mathbf{P}(t)$ denotes the load vectors acting on the pipelines, which are obtained from the fluid solver.

In the fluid-solid interaction analysis of the present study, several assumptions are made: (1) the structural damping is negligible. Therefore, $\mathbf{C} = \mathbf{0}$; (2) the matrices mentioned above are time-invariant in the pipeline systems; (3) similar to the previous studies such as Wang et al. (2018) [11], a one-way coupling between the fluid and the structure is assumed. Therefore, the effects of the structural dynamic responses of the structure on the flow field are not considered.

3.3 Computational setup

3.3.1 Computational domain and numerical methods

In the present study, the pipe diameter (D) and the 90-degree elbow curvature radius (r) are set the same as the experimental setups of Liu et al. (2012) [7], in which $D = 52.5$ mm and $r = 76.4$ mm, respectively. Four different pipeline configurations are studied with different numbers of elbows and directions of inlet flow. The geometries of the different configurations are shown in Figure 3.1. A single and two 90-degree elbow and both vertical and horizontal inlet flow are considered. The open-source CFD code, OpenFOAM-v2012, is employed to carry out the numerical simulations based on the finite volume method. A multiphase solver named interIsoFoam is utilized for the two-phase flow, which combines the Pressure Implicit with Splitting of Operators (PISO) and Semi-Implicit Method f or Pressure Linked Equations (SIMPLE) algorithms for pressure-velocity coupling. The solver interIsoFoam is a modification of the VOF solver interFoam and uses the isoAdvector method, which can maintain a sharper surface and reduce the dissipation compared with the solver interFoam according to Gamet et al. (2020) [16].

The computational domains and the length of different pipe sections for the simulations are shown in Figure 3.1. The four different configurations are named Pipe A, B, C and D in the present study. The same configurations and geometry of pipes are utilized for the dynamic response analysis in Code Aster.

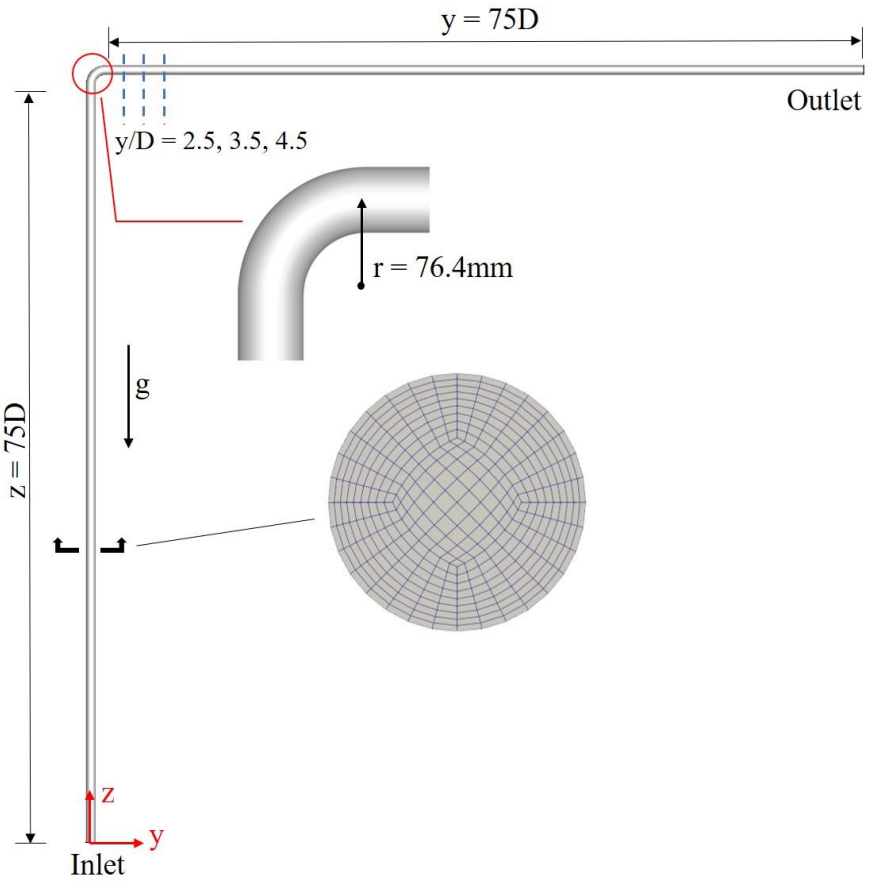
y = 75D
Outlet
y/D = 2.5, 3.5, 4.5
r = 76.4mm
g
z = 75D
z
y
Inlet

(a)

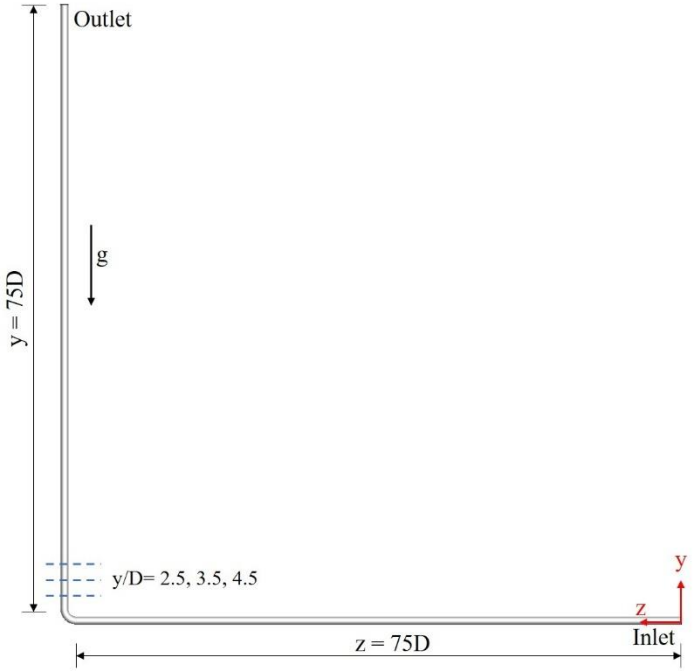
Outlet
g
y = 75D
y/D= 2.5, 3.5, 4.5
y
z
Inlet
z = 75D

(b)

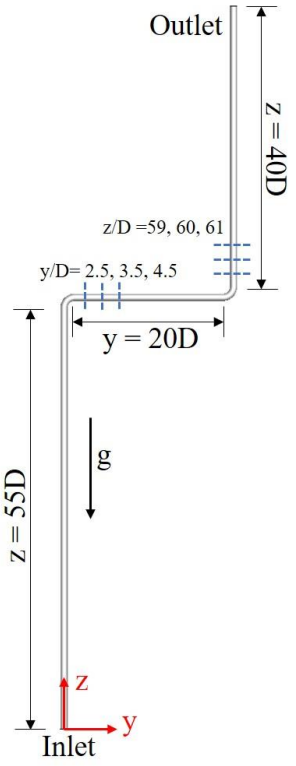
Outlet
z = 40D
z/D =59, 60, 61
y/D= 2.5, 3.5, 4.5
y = 20D
g
z = 55D
z
y
Inlet

(c)

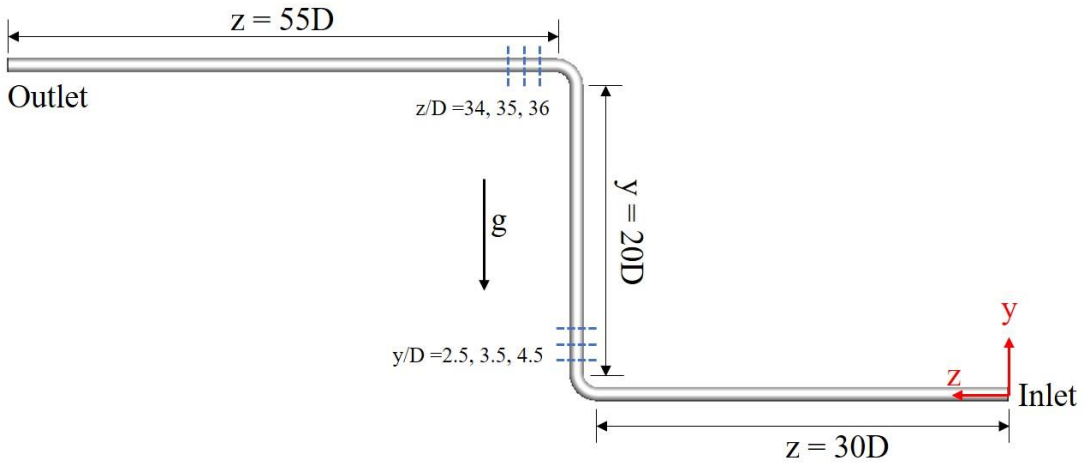

(d)

Figure 3.1. The computational domains for different configurations and the meshes in the cross-sectional plane.

3.3.2 Boundary conditions

The boundary conditions of the numerical simulations are shown in Table 3.1.

Table 3.1. Boundary conditions of CFD simulations in OpenFOAM

Surface domain	Inlet	Outlet	Pipe
U	fixedValue	pressureInletOutletVelocity	fixedValue
P	fixedFluxPressure	fixedValue	zeroGradient
k	fixedValue	zeroGradient	kqRWallFunction
ν_t	calculated	calculated	nutkWallFunction
ω	fixedValue	zeroGradient	omegaWallFunction
α	codedFixedValue	inletOutlet	zeroGradient

The void fraction α and velocity U are utilized to describe the gas injection in the gas-liquid flow at the inlet. The superficial velocities of the gas and liquid are defined respectively as

$$U_{sg} = \frac{Q_g}{A}, \tag{3.12}$$

$$U_{sl} = \frac{Q_l}{A}, \tag{3.13}$$

where Q_g and Q_l denote the volume rates of the gas and the liquid phase respectively and A is the cross-section area of the pipe.

The void fractions α_g and α_l for the two phases are defined as

$$\alpha_g = \frac{A_g}{A}, \tag{3.14}$$

$$\alpha_l = \frac{A_l}{A}, \tag{3.15}$$

where A_g and A_l denote the cross-section area occupied by the gas and liquid phase respectively. For every cross-section along the pipe, there is $A = A_g + A_l$. An example of the gas and liquid phase injection at the inlet is shown in Figure 3.2. The flow velocity U in Table 1 is defined as $U = U_{sg} + U_{sl}$.

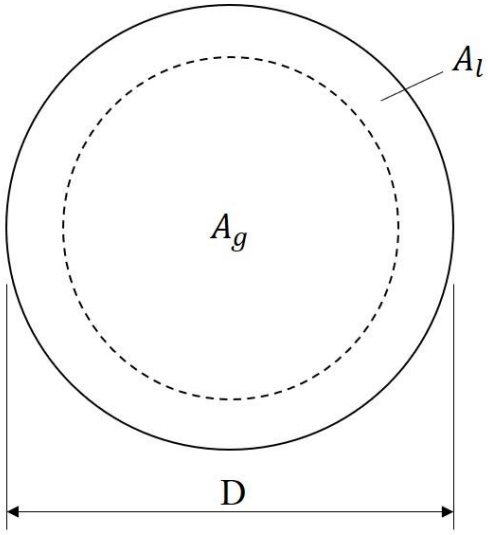

Figure 3.2. Configuration of gas and liquid phase in inlet cross-section area

In the structural responses analysis, the pipelines are modelled using consistent beam elements in Code Aster. Various numbers of fixed supports are set up for different pipe configurations in all of the dynamic analyses, which are shown in Figure 3.3. The element numbers for Pipes A, B, C and D are 1050, 1050, 875 and 690, respectively. The pipe material is stainless steel with a wall thickness of $t = 6\,\text{mm}$, a density of $\rho = 7930\,\frac{\text{kg}}{\text{m}^3}$, Young's modulus $E = 193\,\text{GPa}$ and poison ratio of 0.3. The solution technique for Eq. (3.11) is based on the unconditionally stable HHT-α method (1977).

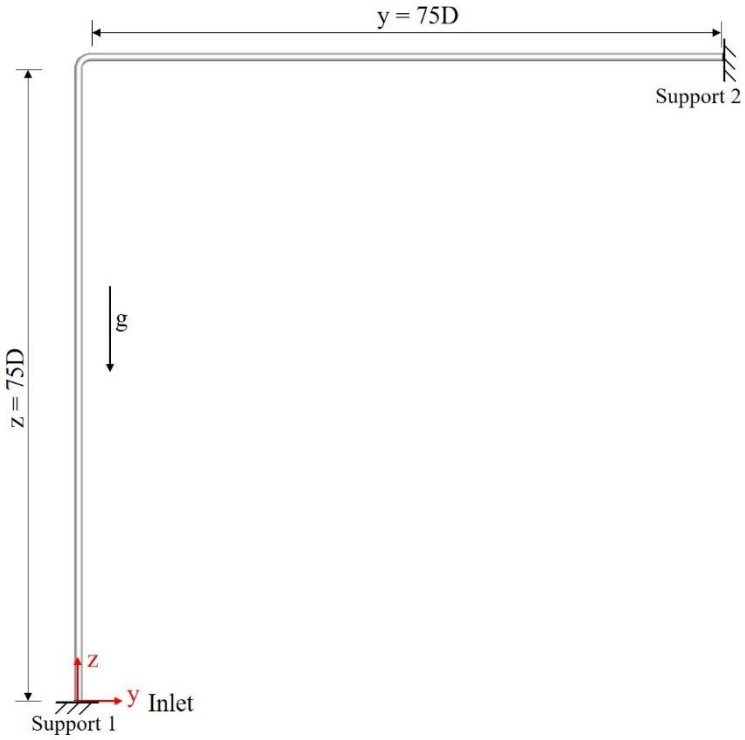

(a) Pipe A with 2 supports

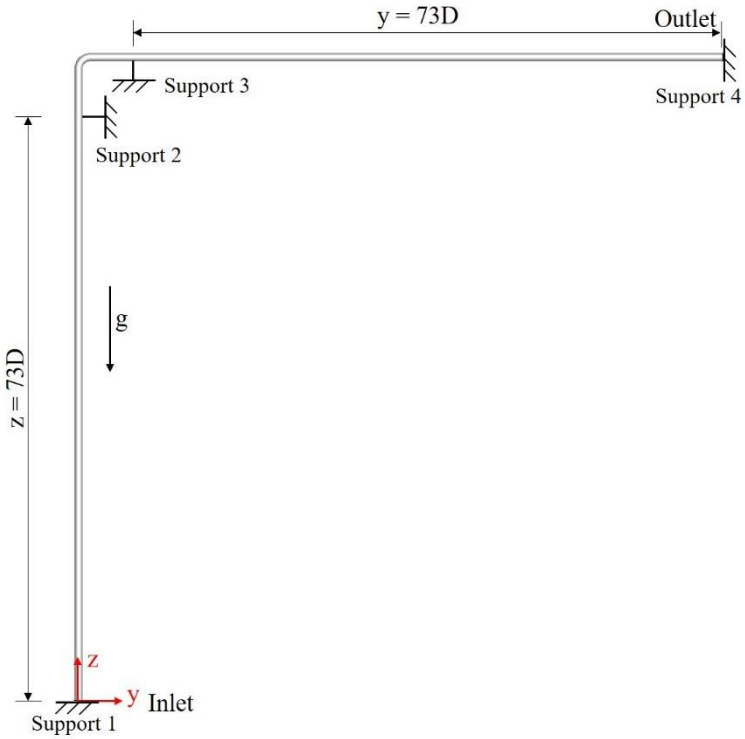

(b) Pipe A with 4 supports

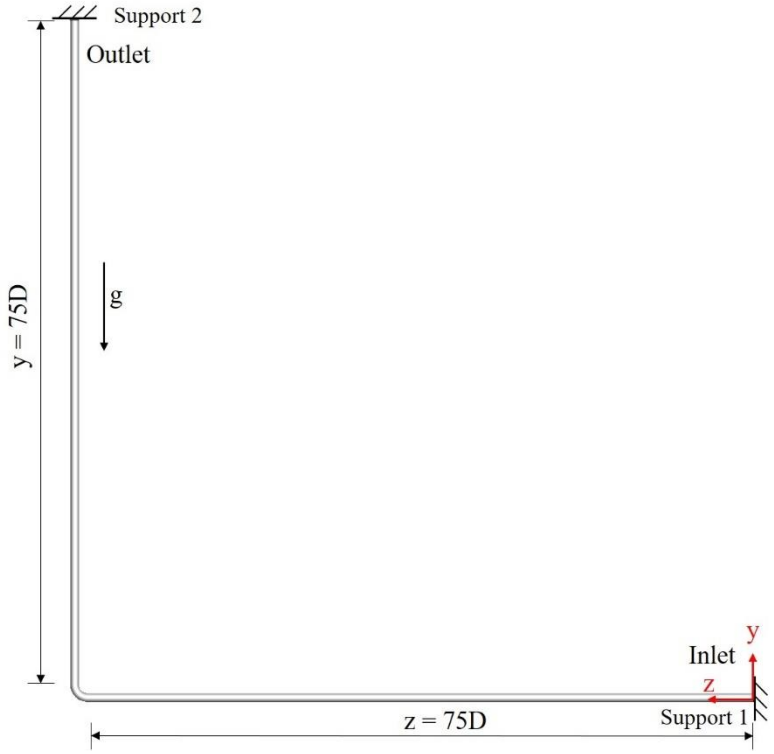

(c) Pipe B with 2 supports

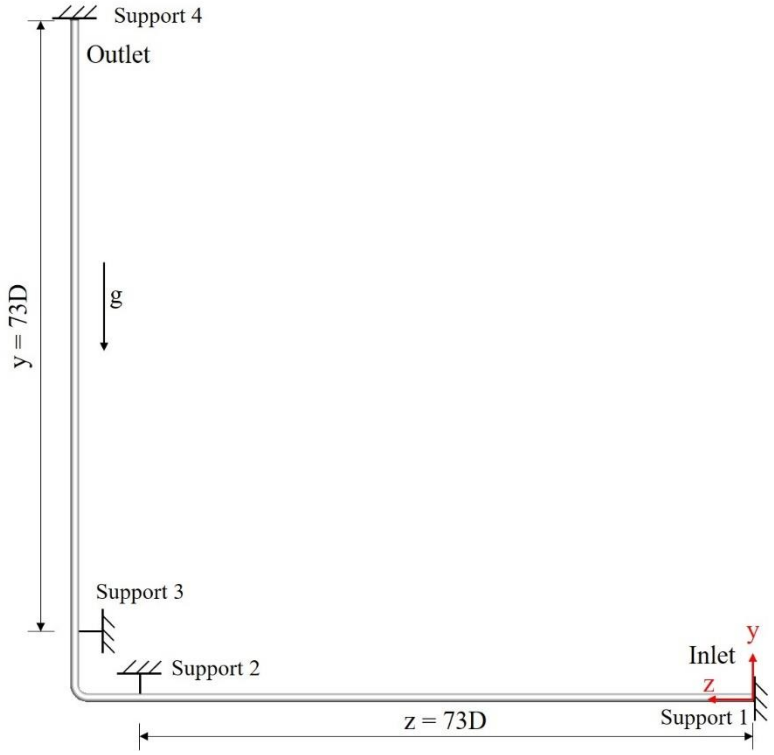

(d) Pipe B with 4 supports

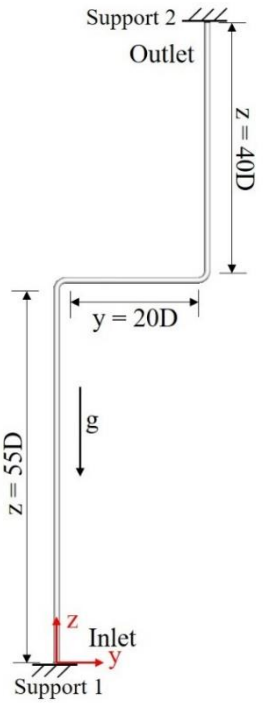

(e) Pipe C with 2 supports

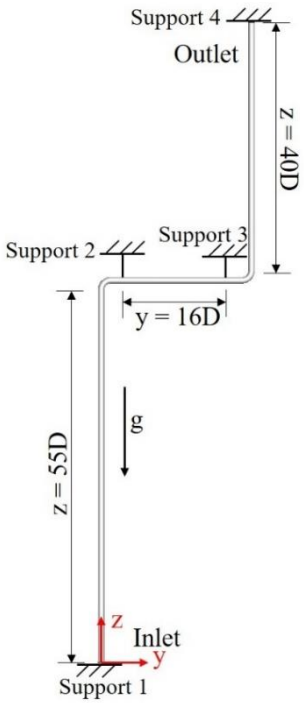

(f) Pipe C with 4 supports

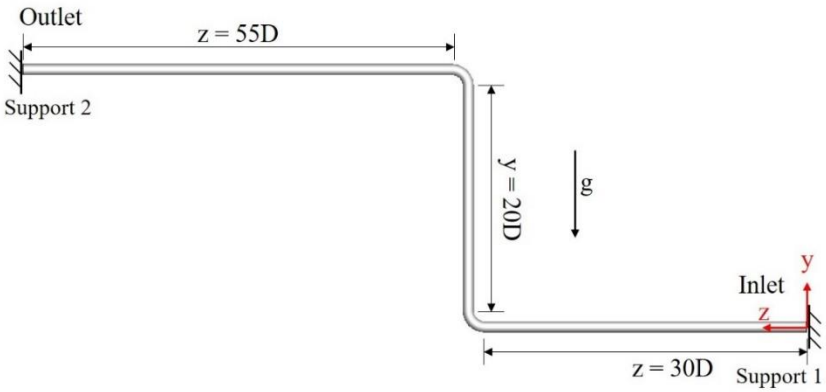

(g) Pipe D with 2 supports

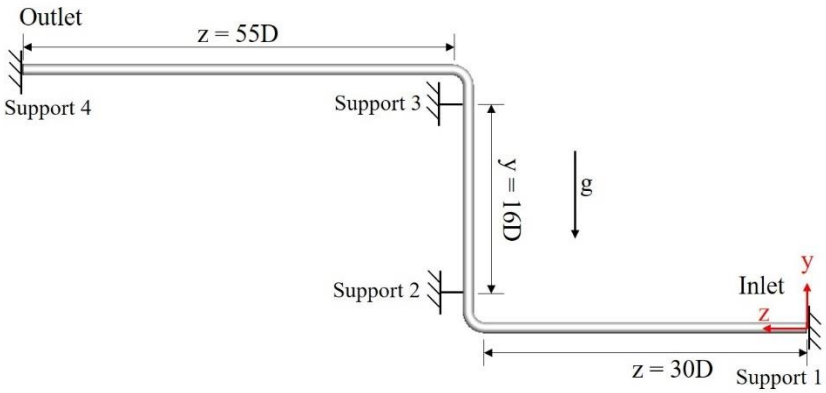

(h) Pipe D with 4 supports

Figure 3.3. Configurations of fixed supports for different pipes.

3.4 Results

3.4.1 Mesh convergence studies and validation studies

The mesh convergence studies have been carried out by using three different meshes for the slug flow in Pipe A. The superficial gas and liquid velocities are set as 0.61 m/s and 0.978 m/s, respectively. The number of cells selected for the three different meshes named Mesh 1, Mesh2 and Mesh 3 are 258720, 369600 and 504000 respectively. The simulation time is 5s which ensures the flow can fully develop. The time-step of the simulation is adjustable and set as 10^{-5} initially. The maximum Courant number is set as 0.2 for all simulation cases. Figure 3.4 shows the time histories of the void fraction for the three different meshes. The elapsed time of simulations are 170000s, 210000s and 330000s for Mesh1, Mesh2 and Mesh3 respectively. The temporal evolutions of the void fractions for the three meshes are different. However, according to Abdulkadir et al. (2015) [17] and Hossain et al. (2019) [10, 13], it is normal that the instantaneous fluctuations of the two-phase flow can vary with different meshes. The results of the mean value and the standard deviation of the void fraction for different meshes are shown in Table 3.2. The relative difference of the mean value reduces to 5.1% and the relative difference of the standard deviation reduces to 1.5% between Meshes 2 and 4. Moreover, Figure 3.5 shows the power spectra density (PSD) of the void fraction of Mesh 2 compared with the experimental data obtained by Liu et al. (2012) [7]. A similar peak value at around $f = 0.3$ Hz can be observed. Therefore, considering the results and the computational cost, the grid resolution of Mesh 2 can be regarded as sufficient for the simulation and will be employed for the subsequent simulations.

Table 3.2. Mean value and standard deviation of void fraction for different meshes

Index	Mesh 1	Mesh 2	Mesh 3
Number of cells	258720	369600	504000
Mean	0.4517	0.4986	0.4731
Std	0.2428	0.2643	0.2683

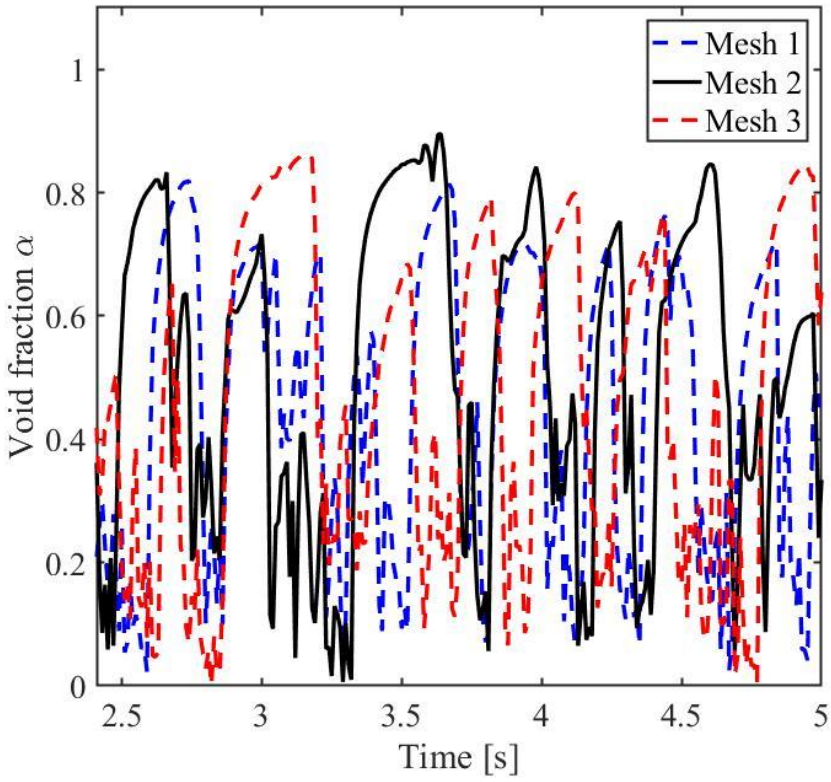

Figure 3.4. Comparison of time series of void fraction for different meshes with time.

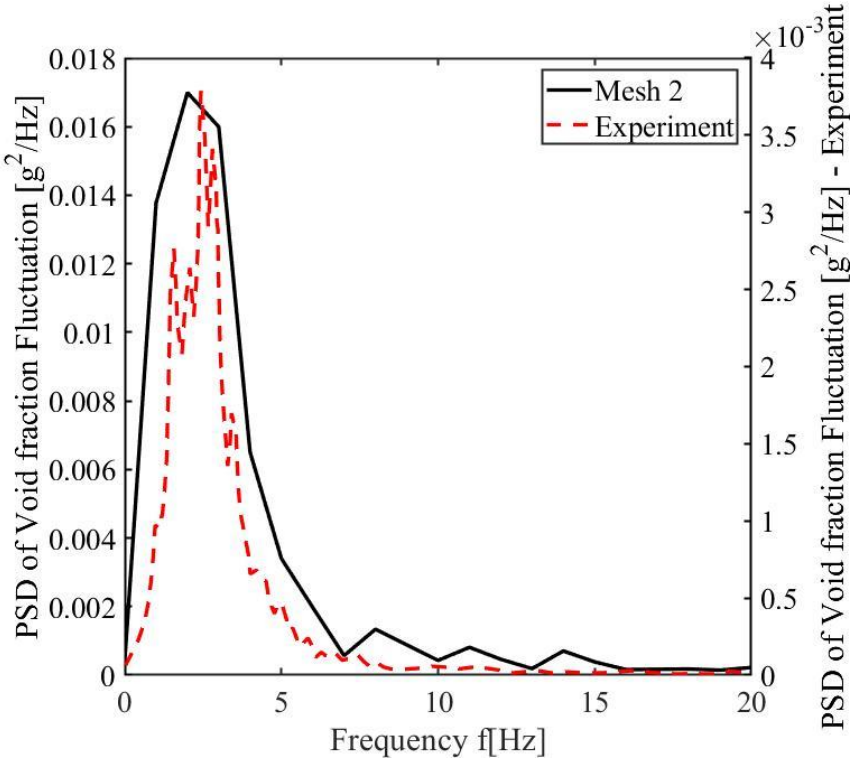

Figure 3.5. Comparison of PSD (power spectral density) of the void fraction obtained using Mesh 2 and the experimental data reported by Liu et al. (2012) [7].

3.4.2 The volume fraction of the two-phase pipe flow

The results of the volume fraction of the fully developed slug flow in Pipe A after 5s are shown in Figure 3.6. The flow is injected vertically at the inlet. The blue regions in the figure are occupied by the gas phase. Close to the inlet, a chain of small gas bubbles is formed gradually and accumulates to form increasingly big bubbles with the moving liquid. The Taylor bubbles (as denoted in Figure 3.6) subsequently appear in the vertical pipe component. When it comes to the 90-degree elbow, the Taylor bubbles break and the broken bubbles attach to the upper inner pipe wall after passing the elbow. Therefore, long bubbles are generated in the horizontal pipe component because of the density distinction between the gas and liquid phase. In the horizontal pipe component, slugging phenomena can happen as well (as denoted in Figure 3.6), depending on the superficial velocities of the gas and liquid phase.

In Figure 3.7, the three-dimensional characteristics of the gas phase in slug flow after 5s are presented in more detail by using the iso-surfaces of α = 0.5 (which is denoted as the interface between the gas and liquid) colored by the local flow velocity magnitudes. For a single Taylor bubble shown in Figure 3.7, there is an obvious difference in the velocity magnitude along the bubble, which may lead to the elongation of the bubble. At the head of the bubble, the velocity is large. At the bottom part of the bubble, the velocity magnitude is low due to the falling of the surrounding liquid films. When the gas phase comes close to the 90-degree elbow, it obviously decelerates because of the obstruction of the elbow wall. After passing the outlet of the elbow, the gas phase accelerates for a distance and decelerates again to attach to the pipe wall. The acceleration variation in this process affects the formation of big and long bubbles in the horizontal pipe component, which results in the fluctuating interface between the gas and liquid phases and fluctuating excitation loads on the pipes.

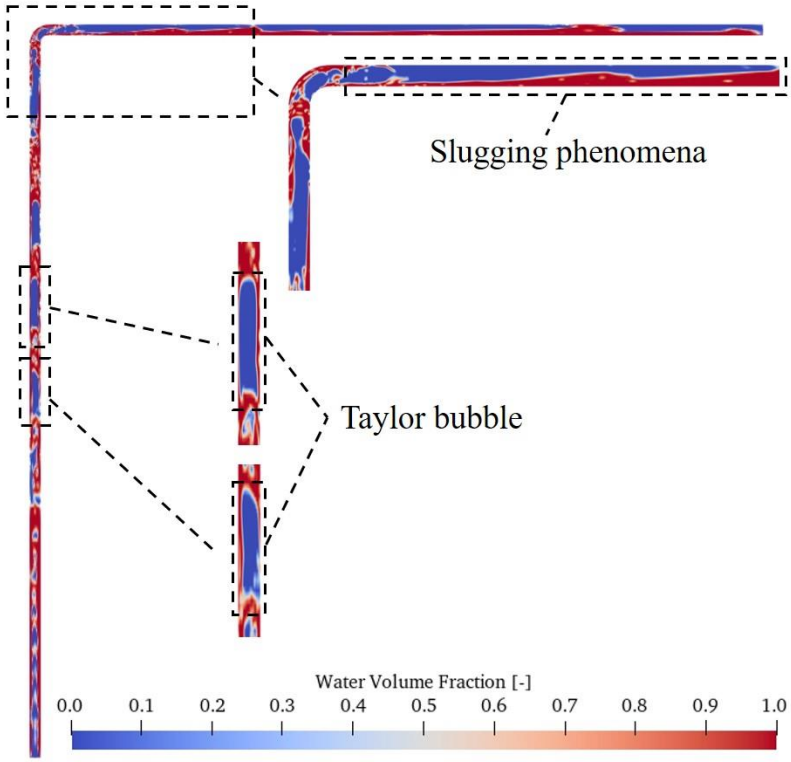

Figure 3.6. Contours of the water volume fraction in Pipe A under a superficial gas velocity of 0.978 m/s and a superficial liquid velocity of 0.61 m/s after 5s.

The results of the liquid volume fraction in Pipe B under a superficial gas velocity of 0.61 m/s and a superficial liquid velocity of 0.978 m/s after 5s are shown in Figure 3.8. A clear gas and liquid stratification can be observed in the horizontal part of the pipe. Because of the density distinction between gas and liquid phases, the gas phase accumulates at the upper pipe wall, and the liquid phase flows at the bottom pipe wall. The gas phase still attaches to the pipe wall when passing the elbow and only after a distance after the outlet of the elbow, small bubbles begin to generate. Compared with Pipe A, the Taylor bubbles generated in Pipe B are smaller and the surrounding flow is more chaotic, as shown in Figure 3.8. For the case shown in Figure 3.7, the Taylor bubbles are located at the middle part of the pipe, while for the case shown in Figure 3.9, the gas accumulates close to the pipe wall. Furthermore, due to the density difference, the region close to the outlet of the vertical pipe part is largely occupied by the gas.

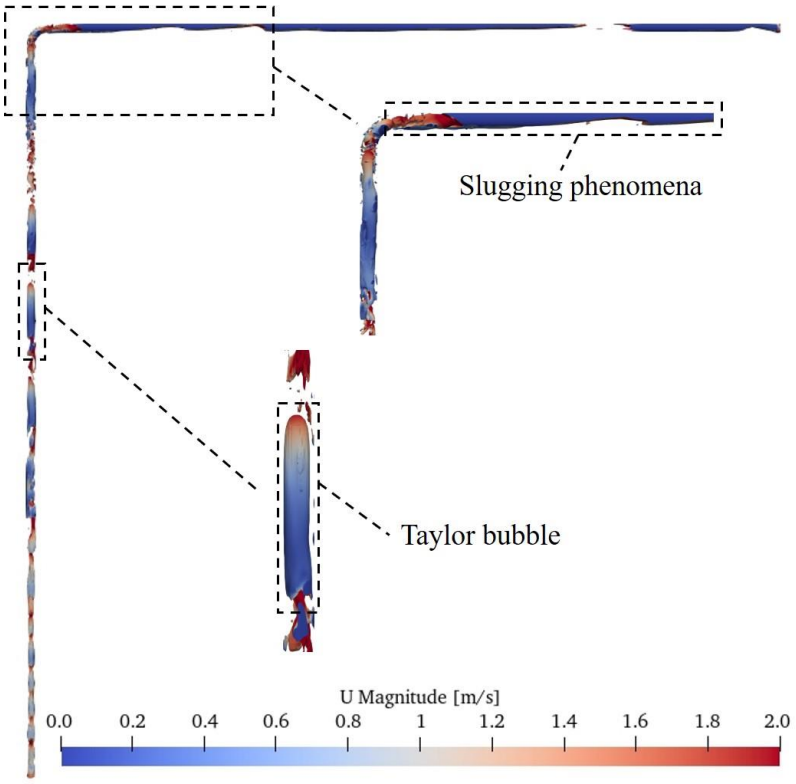

Figure 3.7. Velocity distribution in the iso-surface plot of void fraction in Pipe A under the superficial gas velocity of 0.978 m/s and superficial liquid velocity of 0.61 m/s after 5s.

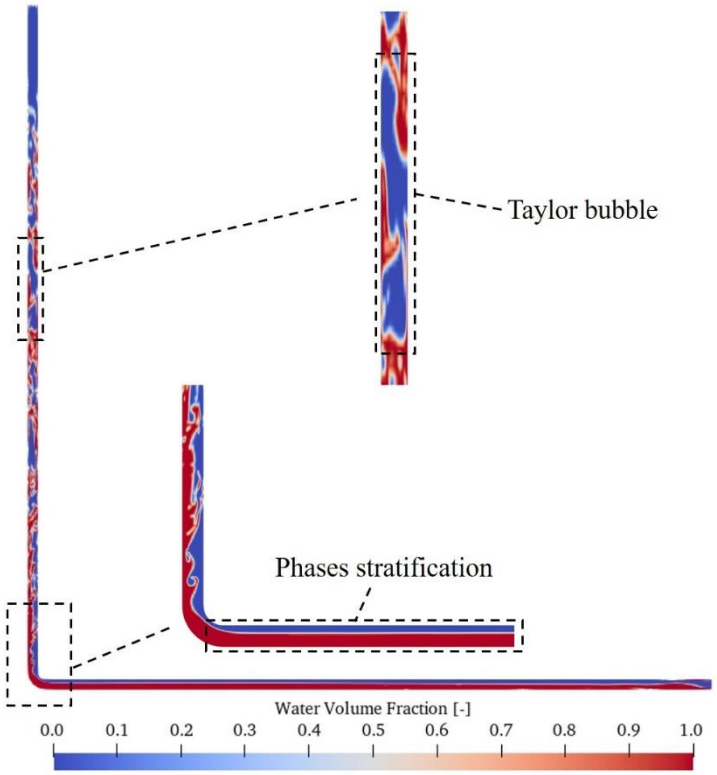

Figure 3.8. Contours of the water volume fraction in Pipe B under a superficial gas

velocity of 0.978 m/s and a superficial liquid velocity of 0.61 m/s after 5s.

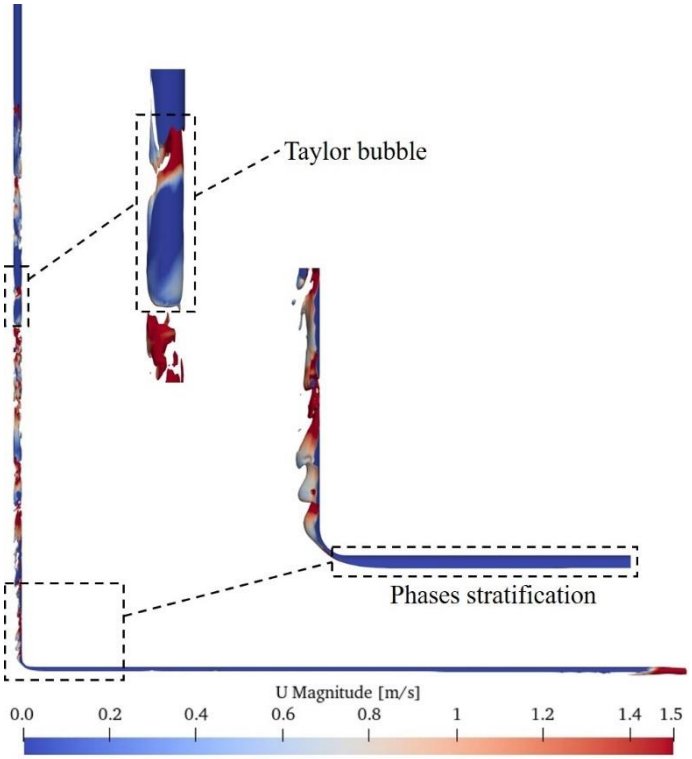

Figure 3.9. Velocity distribution in the iso-surface plot of void fraction in Pipe B under the superficial gas velocity of 0.978 m/s and superficial liquid velocity of 0.61 m/s after 5s.

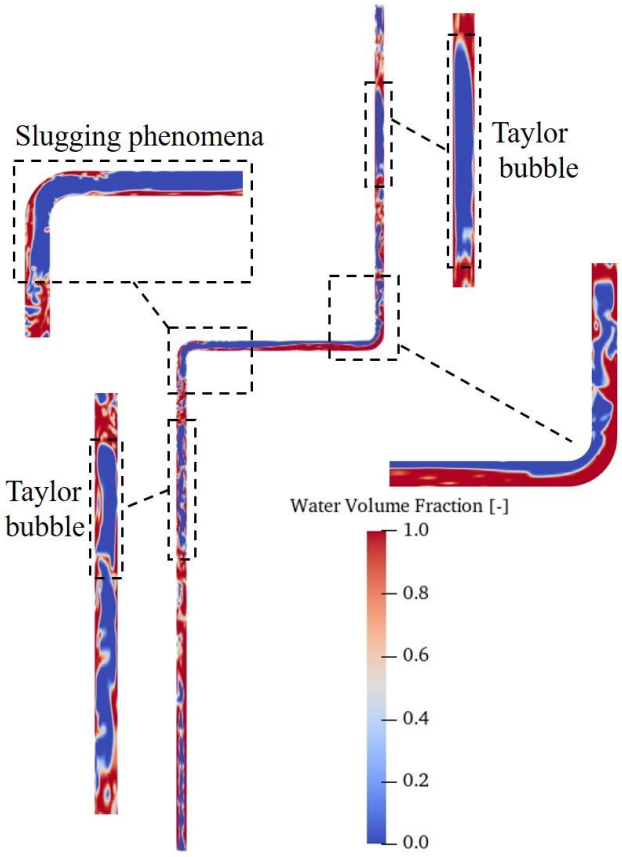

Figure 3.10. Contours of the water volume fraction in Pipe C under a superficial gas velocity of 0.978 m/s and a superficial liquid velocity of 0.61 m/s after 5s.

The results of slug flow in pipelines with two 90-degree elbows after 5s are presented in Figures 3.10 ~ 3.13. As shown in Figure 3.10, small Taylor bubbles are generated in the first vertical pipe component and coalesce in the horizontal part of the pipe. Due to the obstruction of the first elbow, the Taylor bubble becomes deformed as shown in Figure 3.11 and a stratification with an oblique interface begins to form in the horizontal part. After the second elbow, the gas region breaks into small bubbles as denoted in Figure 3.10. After a distance past the elbow, large-scale Taylor bubbles are regenerated in the second vertical part of the pipe. For Pipe D, as shown in Figure 3.12, the slugging phenomena only occur at the second elbow and there seems to be no clear shape of the Taylor bubbles, which becomes more irregular compared with previous cases. The reason for this phenomenon is that in Pipe D, the small bubbles in the vertical part of the pipe begin to coalesce at the second elbow and the Taylor bubbles have not been generated. The small-scale bubbles continue to move with the flow. Large Taylor bubbles are thus more difficult to occur in Pipe D compared to Pipe C. Figure 3.13 shows that in most regions of Pipe D, the flow velocity magnitudes tend to be smaller than in (ocated at the two elbows.

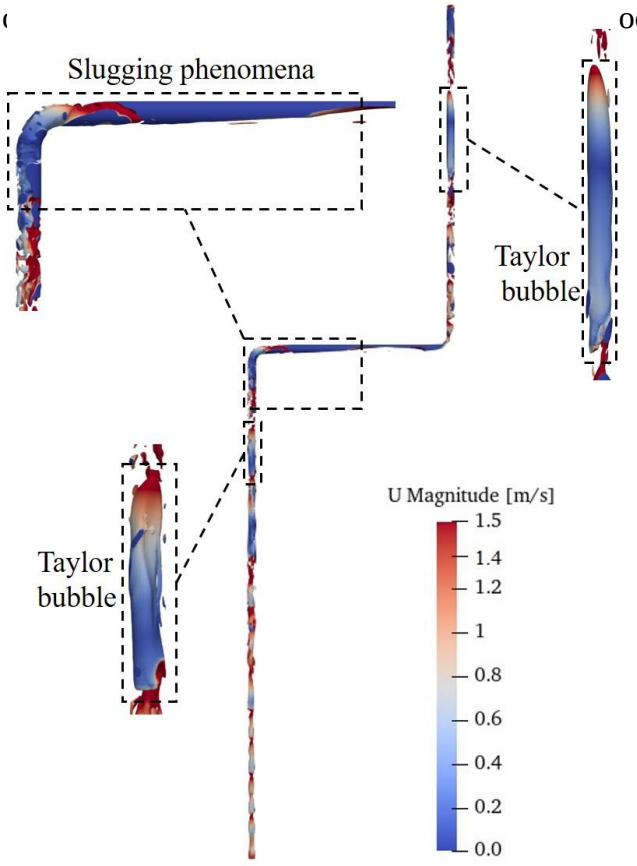

Figure 3.11. Velocity distribution in the iso-surface plot of void fraction in Pipe C under the superficial gas velocity of 0.978 m/s and superficial liquid velocity of 0.61 m/s after 5s.

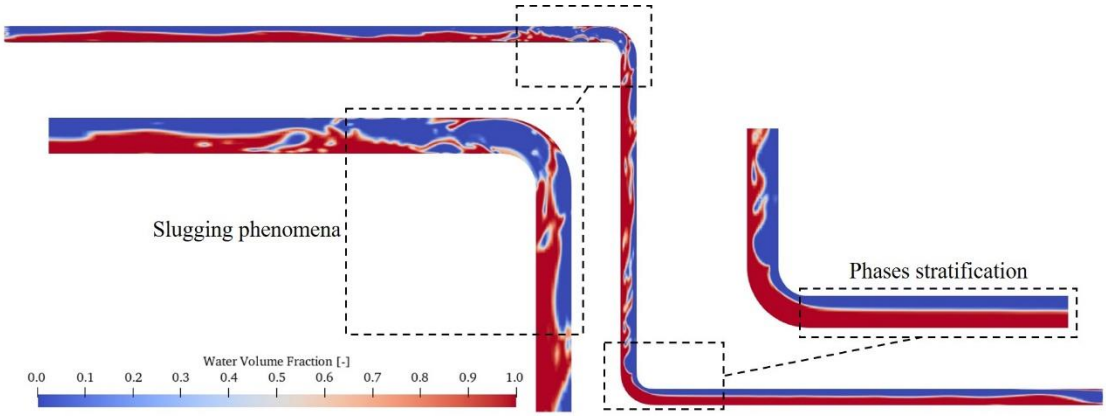

Figure 3.12. Contours of the water volume fraction in Pipe D under a superficial gas velocity of 0.978 m/s and a superficial liquid velocity of 0.61 m/s after 5s.

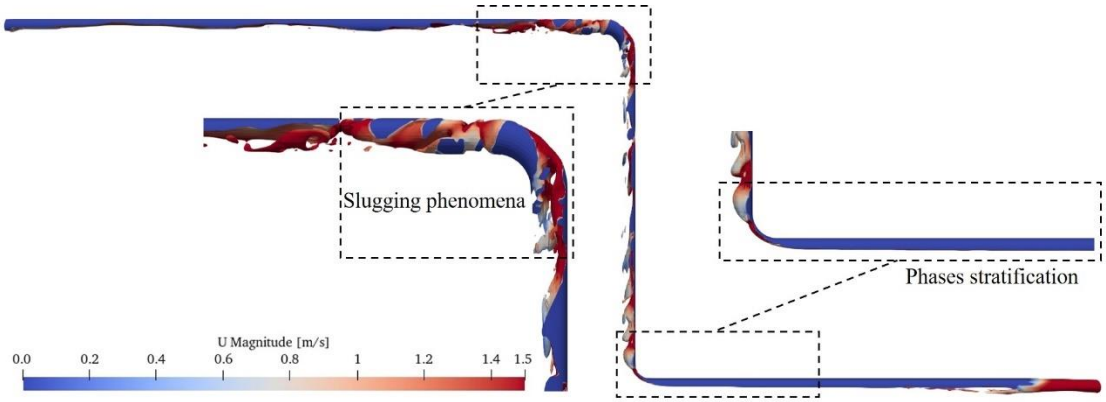

Figure 3.13. Velocity distribution in the iso-surface plot of void fraction in Pipe D under the superficial gas velocity of 0.978 m/s and superficial liquid velocity of 0.61 m/s after 5s.

Figure 3.14 shows the streamlines and the contours of tangential velocity on different sections of different pipelines. According to various previously published studies such as Dean (1927) [18], Sudo et al. (1998) [19] and Jurga et al. (2022) [20], an important phenomenon for a single-phase flow through a pipe bend is a secondary flow behind a bend part because of the centrifugal force and the friction effect of the pipe wall. Tangential velocity is defined as the vector sum of component velocities in a specific cross-section plane, which can be used to measure the strength of secondary flow. For gas-liquid two-phase flow through a pipe bend, secondary motions can also occur. The cross-sectional streamlines at three locations after the elbow as indicated in Figure 3.1 are shown in Figure 3.14 together with the contours of the tangential velocity magnitude. The cross-sectional secondary motions of gas-liquid two-phase flow are obvious for Pipes A, B and C in the downstream region of the pipe bend. However, compared with the single-phase flow, the vortex cores of the two-phase flow downstream are randomly distributed and are affected by the movement of the gas

phase. Moreover, for Pipe A, the in-plane vortices seem to be located close to the pipe wall at $y/D = 2.5$ and gradually move towards to the center part of the pipe at $y/D = 4.5$. For Pipe B, the in-plane recirculations are not strong after the horizontal part of the pipe while multiple focuses are observed. For Pipe C, multiple small vortices can be observed after the first elbow while after the second elbow, the small vortices tend to merge into a pair of large secondary flows, which are squeezed towards the pipe wall. For Pipe D, there is almost no in-plane secondary flow after the first horizontal part while after the second elbow, strong in-plane vortices are observed.

(a) Pipe A

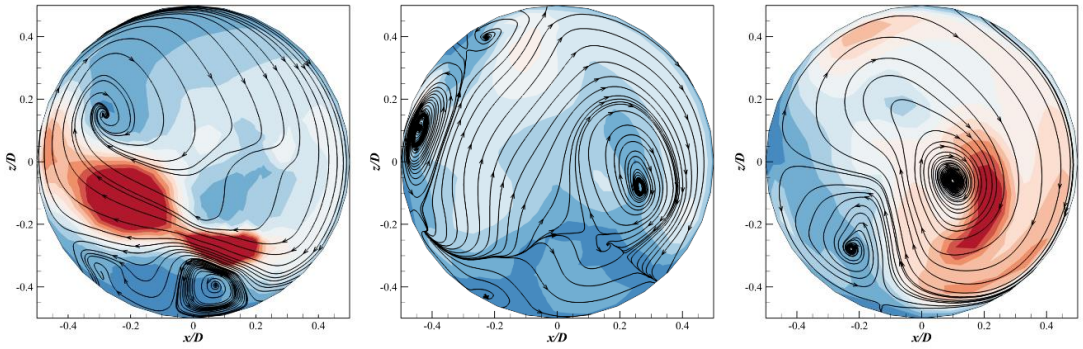

y/D = 2.5 y/D = 3.5 y/D = 4.5

(b) Pipe B

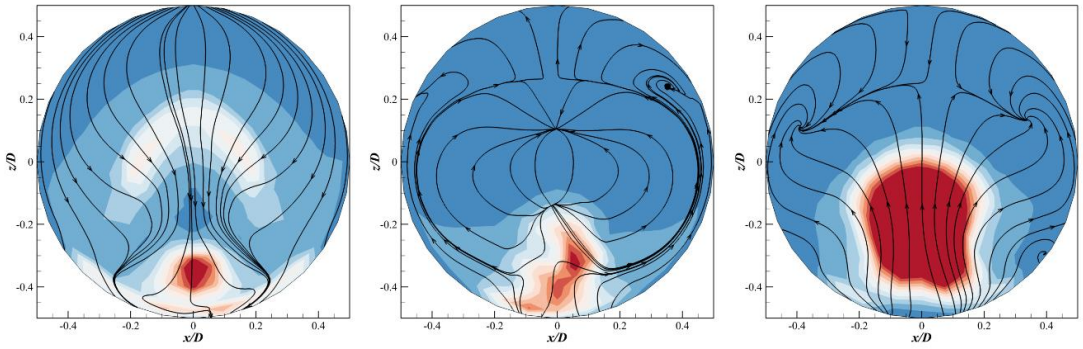

y/D = 2.5 y/D = 3.5 y/D = 4.5

(c) Pipe C

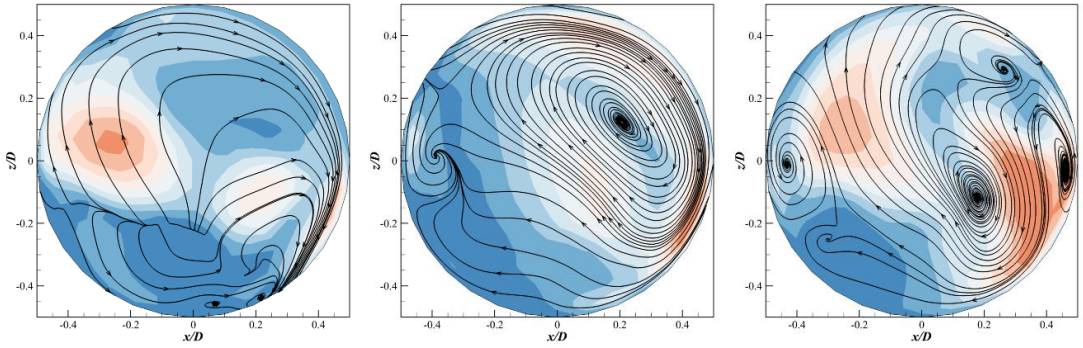

y/D = 2.5 y/D = 3.5 y/D = 4.5

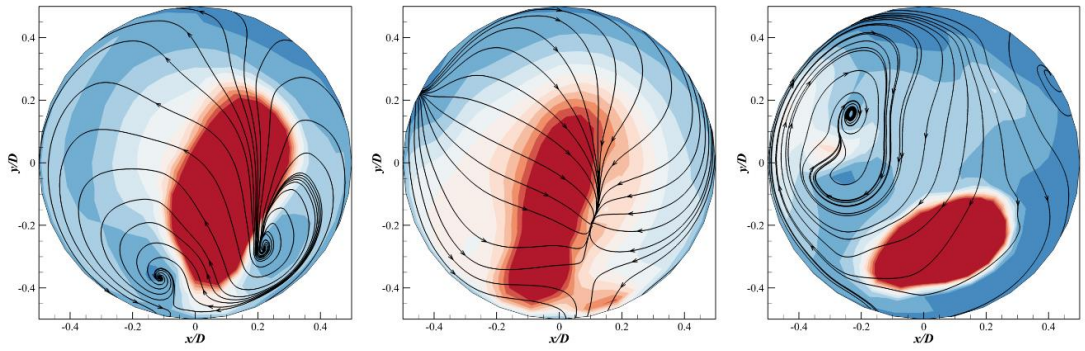

z/D = 59 z/D = 60 z/D = 61

(d) Pipe D

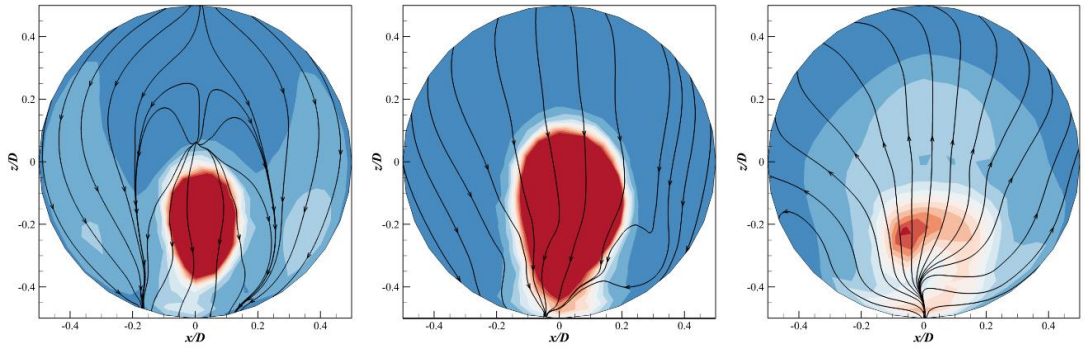

y/D = 2.5 y/D = 3.5 y/D = 4.5

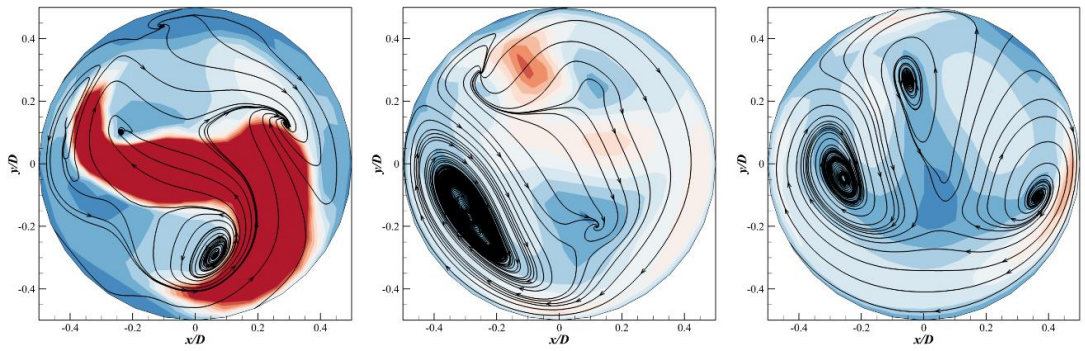

z/D = 34 z/D = 35 z/D = 36

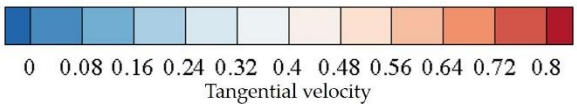

Figure 3.14. Streamlines and the contours of tangential velocity at different axial locations of different pipelines after 5s.

3.4.3 Two-phase flow induced forces

The two-phase flow-induced forces acting on the pipelines and the resulting structural response are analyzed in a one-way coupling method. The forces acting on the pipelines are obtained by using internal pressure. The forces along the pipelines at $t = 3\text{s}$, $t = 4\text{s}$ and $t = 5\text{s}$ are shown in Figures 3.15 ~ 3.18. Dimensionless distance d/L is defined as the ratio of the distance from the starting point along the pipe's central line to the total length of the pipe. The starting point is at the inlet. It should be mentioned at $t = 3\text{s}$, the two-phase pipe flows inside Pipe A and B have not reached the outlet while at $t = 5\text{s}$ is the time step when the flow is fully developed and other time steps such as $t = 3\text{s}$ and $t = 4\text{s}$ are the ones when the flow is un-fully developed.

The distribution of the force magnitudes along Pipe A at $t = 4\text{s}$ and $t = 5\text{s}$ are shown in Figure 3.15. The fluctuation of the force magnitude along Pipe A before the elbow section shows a strong correlation with the result of the water volume fraction in Pipe A shown in Figure 3.6, where Taylor bubbles display spatial periodicity in the section before the elbow. It is evident that the magnitude fluctuation of the excitation forces in Pipe A decreases rapidly close to the elbow. After the elbow, the force magnitude begins fluctuating again when the flow is fully developed.

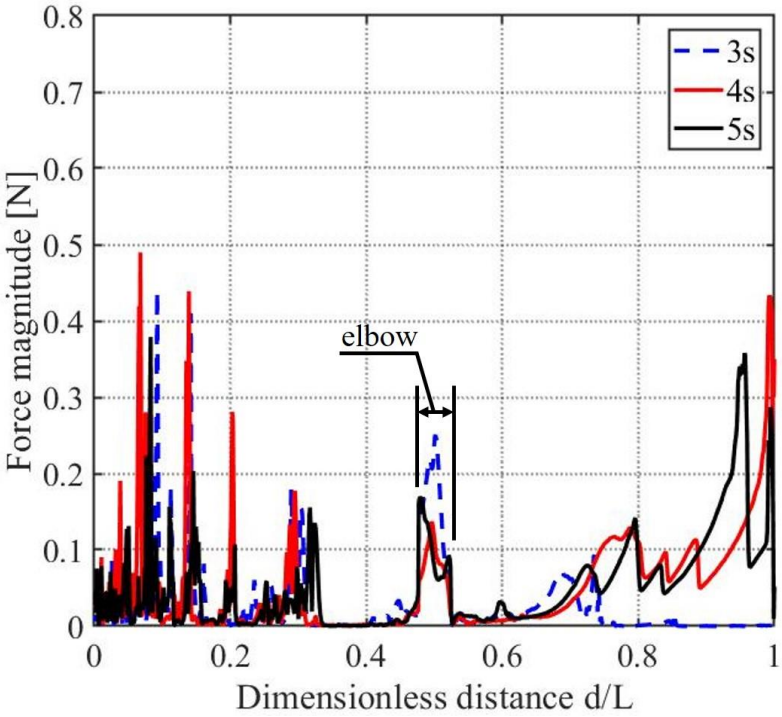

Figure 3.15. The magnitude of force acting on Pipe A under internal pressure at $t = 3\text{s}$, $t = 4\text{s}$ and $t = 5\text{s}$.

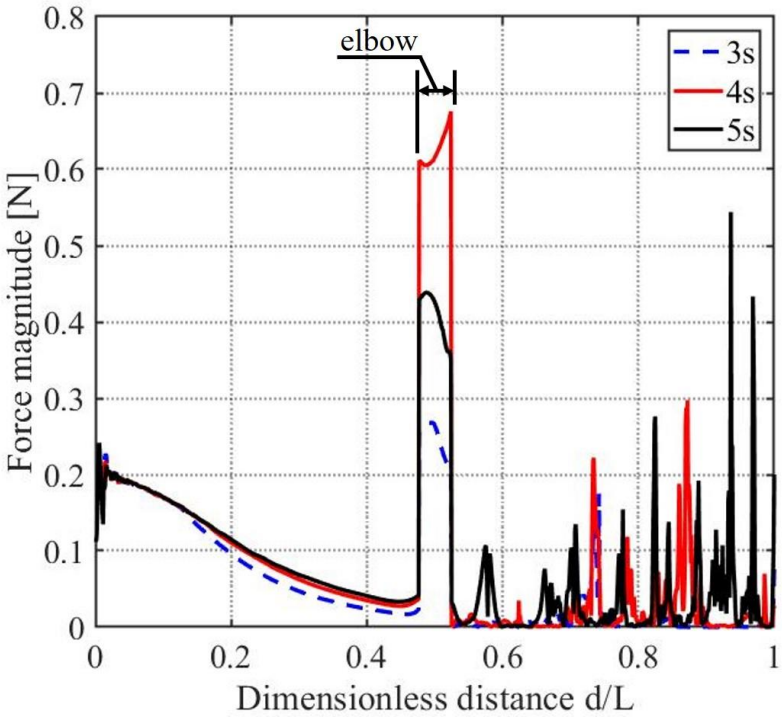

Figure 3.16. The magnitude of force acting on Pipe B under internal pressure at $t = 3\text{s}$, $t = 4\text{s}$ and $t = 5\text{s}$.

As the excitation force result shown in Figure 3.16, the magnitude of the excitation force at the elbow section in Pipe B decreases after the flow is fully developed. Moreover, compared with Pipe A, the force magnitudes at the elbow section in Pipe B are evidently higher. A possible reason is that in Pipe B, the gas phase is attached to one side of the pipe wall at the elbow due to the stratification in the horizontal part, which may lead to a higher pressure difference at the pipe wall.

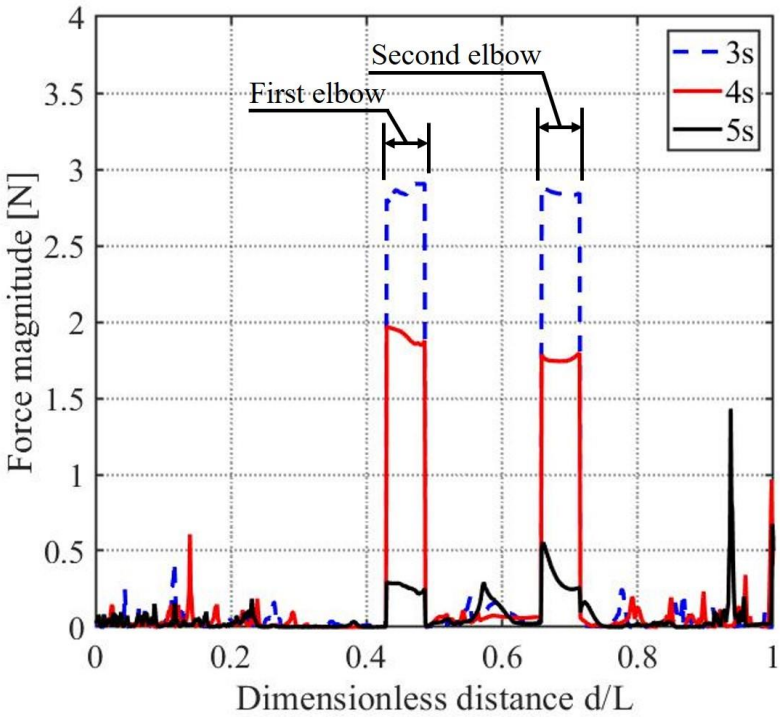

Figure 3.17. The magnitude of force acting on Pipe C under internal pressure at $t = 3\text{s}$, $t = 4\text{s}$ and $t = 5\text{s}$.

Comparing Figures 3.15, 3.16 and Figures 3.17, 3.18, it is obvious that the two-phase flow-induced forces are generally larger for the double-elbow pipelines than the sing-elbow pipelines due to a more chaotic vortices distribution in Pipes C and D. The forces at the two elbows for Pipe C are much larger than those for Pipe D before $t = 5\text{s}$ when the flow is not fully developed because Taylor bubbles are forming in the vertical section of Pipe C. In Figure 3.17, the magnitudes of the excitation force at two elbows in Pipe C obviously decrease from $t = 3\text{s}$ when the first Taylor bubbles pass through the two elbows to $t = 5\text{s}$ when the flow is fully developed. According to the force distribution in Figure 3.17 and Figure 3.18, the excitation forces mainly act on the two elbows, where there are changes in the flow directions. Therefore, the pipeline configuration of Pipe C can be critical when the two-phase flow is just injected through the inlet before fully developing through the pipeline.

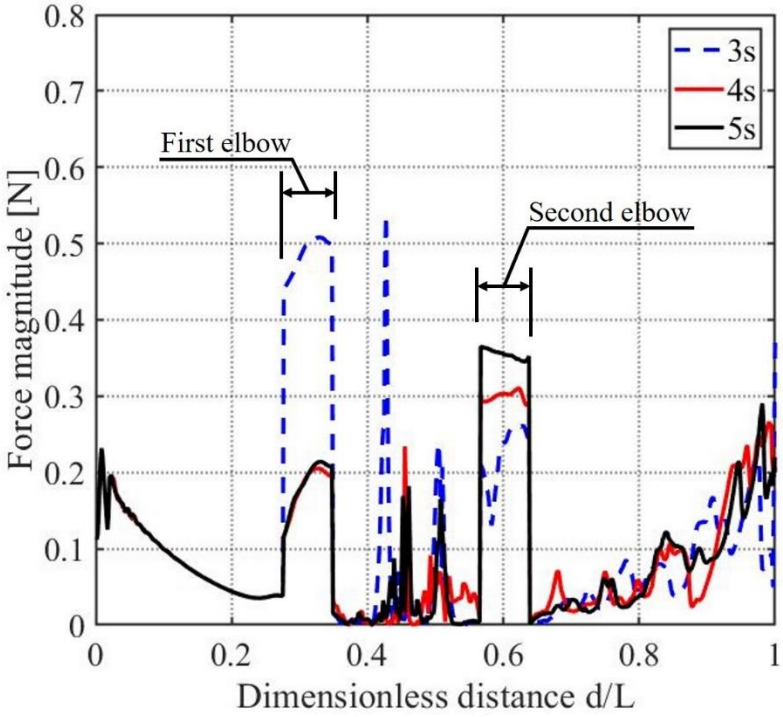

Figure 3.18. The magnitude of force acting on Pipe D under internal pressure at $t = 3\text{s}$, $t = 4\text{s}$ and $t = 5\text{s}$.

3.4.4 Dynamic response analysis

The results of the times series of the reaction forces for different pipes with fixed supports are shown in Figure 3.19, in which $N_{yi(i=1,\dots,4)}$ and $N_{zi(i=1,\dots,4)}$ are denoted as the reaction forces of fixed supports $i\ (i = 1, \dots, 4)$ in y and z directions. The specific locations of fixed supports $i\ (i = 1, \dots, 4)$ are provided in Figure 3.3. The results of reaction forces in x direction $N\_xi(i = 1, \dots, 4)$ are not shown in Figure 19 because they are all close to 0 in all of the response analysis.

From the time series of the reaction forces in Figure 3.19, the damping effect of the pipeline can be observed, which means that the reaction forces of the fixed supports fluctuate greatly in the beginning and these forces fluctuations are weaken fast. It is obvious that there are some peaks in the middle section of time because the Taylor bubbles pass the positions of the fixed supports and lead to large pressure fluctuation, which shows a good agreement with the results in Figures 3.6 ~ 3.13. These peaks of reaction forces are large compared with the two-phase flow-induced forces in Figures 3.15 ~ 3.18, which can be regarded as impact loads for the pipelines. Comparing the results of pipes with 2 supports and 4 supports, the oscillations of the reaction forces of the supports are weaken for most of the pipes with 4 supports. Therefore, the increase of the fixed supports can improve the damping effect of the pipelines on liquid-gas two-phase flow.

As the results in Figure 3.19 show, the forces fluctuations in the middle section of time for Pipe C are still great after increasing fixed supports to 4, which means the

damping effect of increasing fixed supports is not particularly effective for Pipe C. Possible reason can be that the excitation forces in Pipe C are the maximum among all pipes cases from Figures 3.15 ~ 3.18. In general, Pipe C is most sensitive to the excitation force induced by gas-liquid two-phase flow among Pipe A, B, C and D.

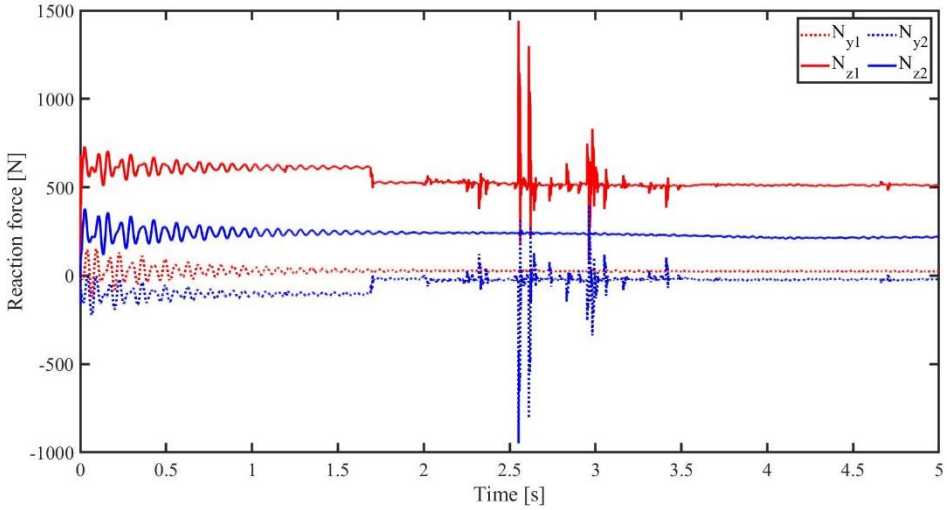

(a) Pipe A with 2 supports

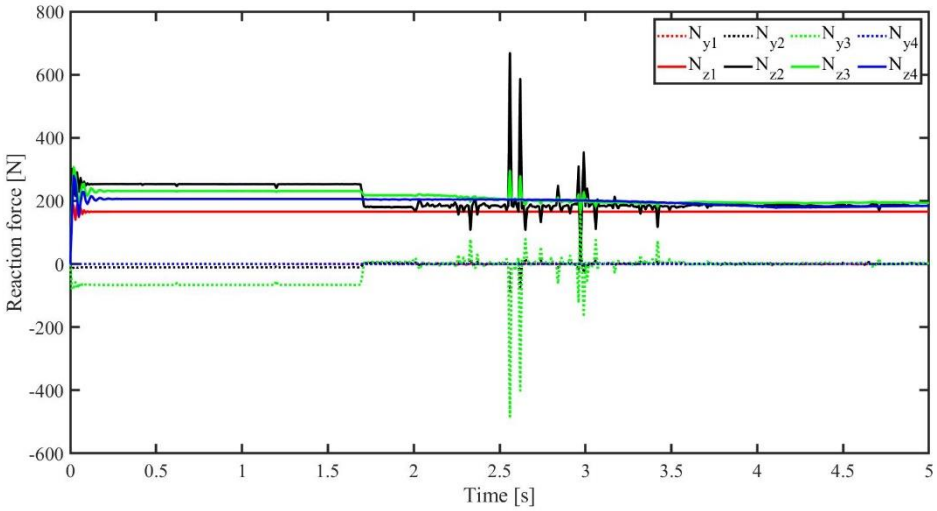

(b) Pipe A with 4 supports

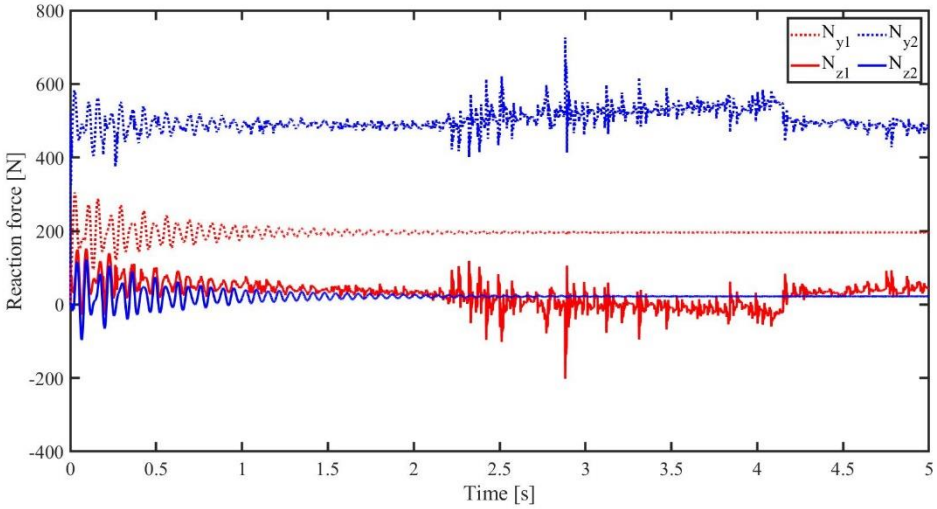

(c) Pipe B with 2 supports

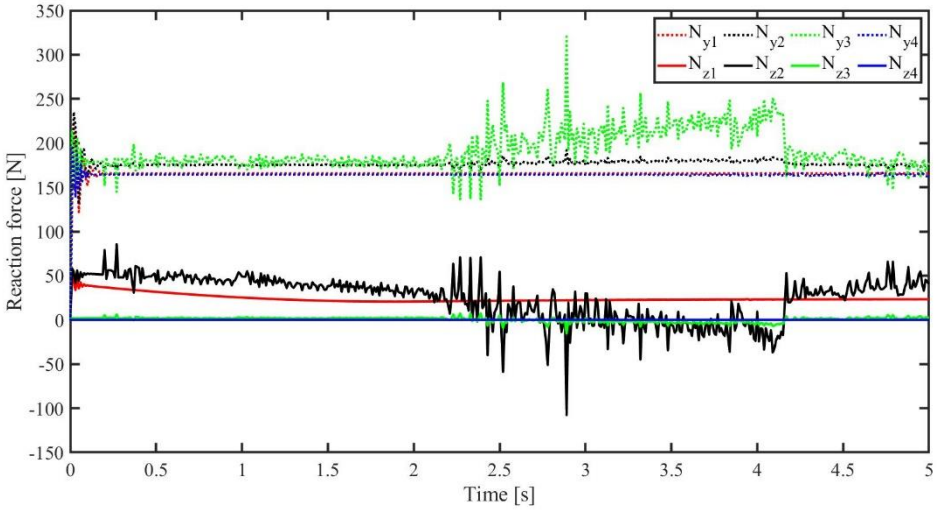

(d) Pipe B with 4 supports

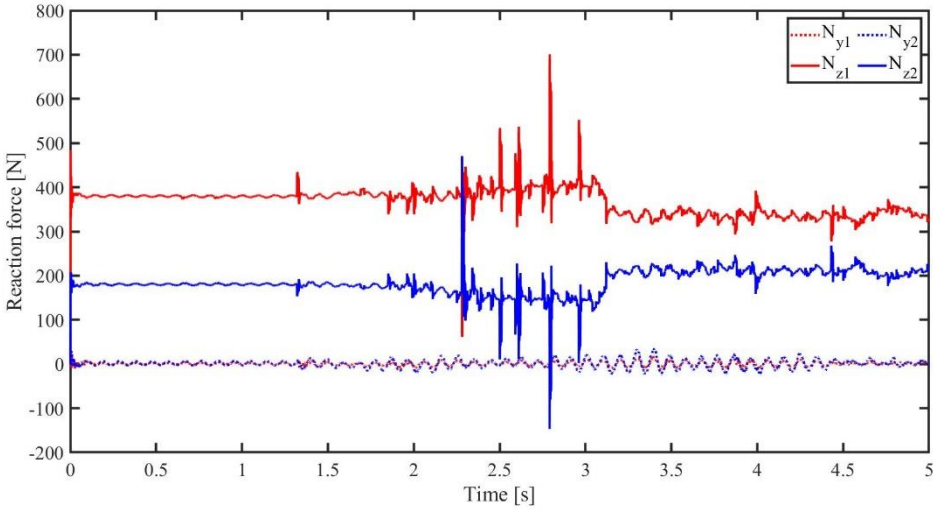

(e) Pipe C with 2 supports

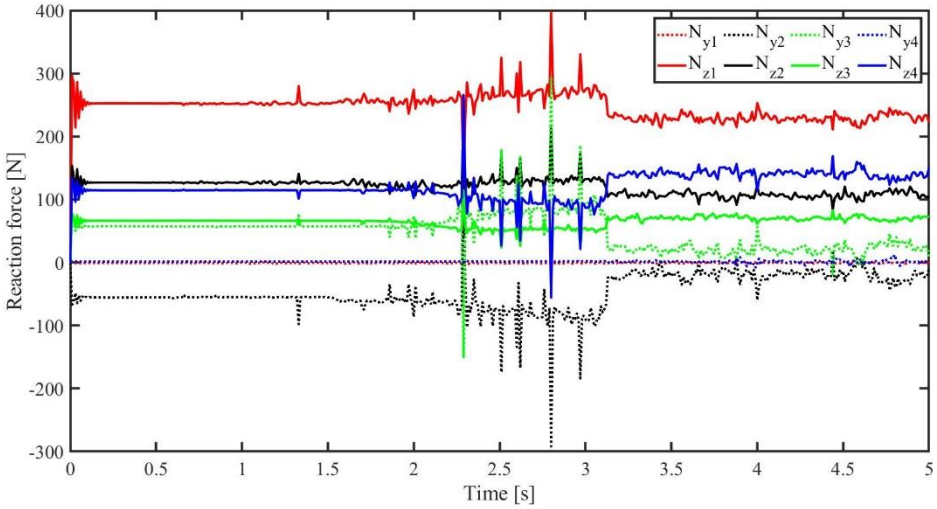

(f) Pipe C with 4 supports

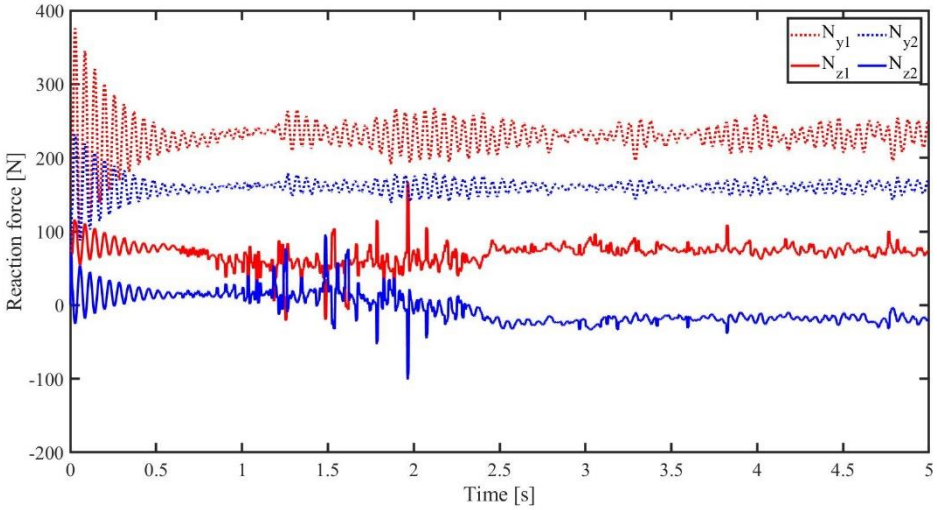

(g) Pipe D with 2 supports

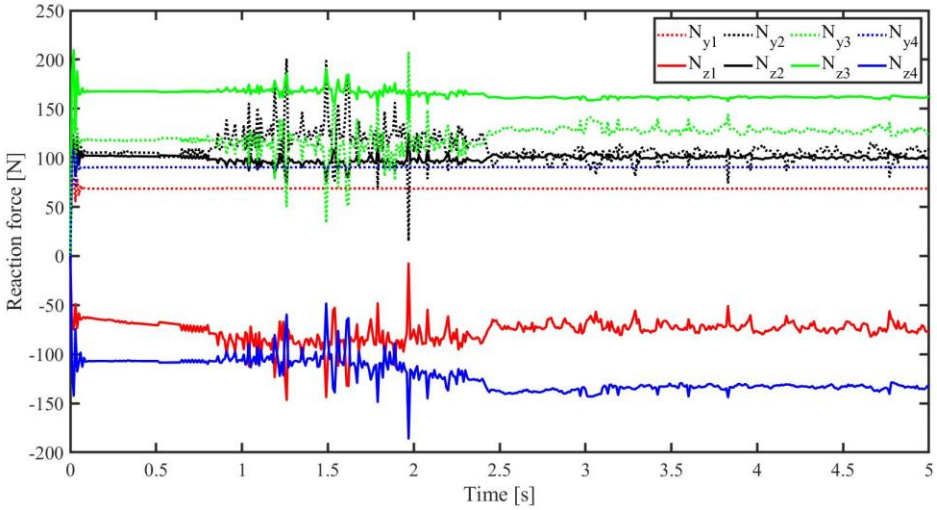

(h) Pipe D with 4 supports

Figure 3.19. Time series of reaction forces for different pipes with fixed supports.

3.5 Conclusion

In the present study, CFD simulations are carried out to investigate the gas-liquid two-phase flow inside different pipelines with 90-degree elbows and a finite element analysis is performed to study the dynamic response of the pipelines to the two-phase flow-induced forces. The VOF method is used to capture the interface between the liquid and the gas phases. The effects of the elbow configurations on the flow characteristics and the dynamic response are discussed. The main conclusions are outlined below:

- Large-scale Taylor bubbles are clearly observed in the vertical part of the pipelines for the single-elbow pipeline cases. With a horizontal inlet flow, the bubbles become small and chaotic in the vertical part of the pipe. For the double-elbow cases, with a vertical inlet flow, a stratification of the liquid and gas is formed in the horizontal part of the pipe and large Taylor bubbles are regenerated after the second elbow in the vertical pipe part. However, for the double-elbow cases with a horizontal inlet flow, there is almost no large Taylor bubble in the pipe.
- The excitation forces of gas-liquid two-phase flow in pipe change rapidly at elbow sections, where the accumulation of the gas phase with a small density occurs and thus the pressure differences become considerably large.
- Increasing the number of fixed supports can weaken the fluctuation of the reaction forces of fixed supports and enhance the damping effect of the pipelines. Among the investigated pipe configurations, the reaction forces fluctuation of the double-elbow case with a vertical inlet flow is the only one still great after using more supports, which means that this pipeline configuration is the most sensitive to multiphase flow-induced forces in the present study.

References

1. Yih T S, Griffith P. The Measurement, interpretation and use of unsteady momentum fluxes in two-phase flow. R. Cambridge, Mass.: MIT Dept. of Mechanical Engineering, 1967.

2. Hara F. Two-phase flow induced vibrations in a horizontal piping system. J. Nippon Kikai Gakkai Ronbunshu, 1976, 42, 2400-2411.

3. Pettigrew M J, Taylor C E. Two-phase flow-induced vibration: An overview. J. 1994.

4. Pettigrew M J, Taylor C E, Fisher N J, et al. Flow-induced vibration: recent findings and open questions. J. Nuclear Engineering and Design, 1998, 185, 249-276.

5. Tay B L, Thorpe R B. Effects of liquid physical properties on the forces acting on a pipe bend in gas–liquid slug flow. J. Chemical engineering research and design, 2004, 82, 344-356.

6. Riverin J L, De Langre E, Pettigrew M J. Fluctuating forces caused by internal two-phase flow on bends and tees. J. Journal of sound and vibration, 2006, 298, 1088-1098.

7. Liu Y, Miwa S, Hibiki T, et al. Experimental study of internal two-phase flow induced fluctuating force on a 90 elbow. J. Chemical Engineering Science, 2012, 76, 173-187.

8. Miwa S, Hibiki T, Mori M. Analysis of flow-induced vibration due to stratified wavy two-phase flow. J. Journal of Fluids En-gineering, 2016, 138.

9. Hirt C W, Nichols B D. Volume of fluid (VOF) method for the dynamics of free boundaries. J. Journal of computational physics, 1981, 39, 201-225.

10. Hossain M, Chinenye-Kanu N M, Droubi G M, et al. Investigation of slug-churn flow induced transient excitation forces at pipe bend. J. Journal of Fluids and Structures, 2019, 91, 102733.

11. Wang L, Yang Y, Li Y, et al. Resonance analyses of a pipeline-riser system conveying gas-liquid two-phase flow with flow-pattern evolution. J. International Journal of Pressure Vessels and Piping, 2018, 161, 22-32.

12. Mohmmed A O, Al-Kayiem H H, Osman A B, et al. One-way coupled fluid–structure interaction of gas–liquid slug flow in a horizontal pipe: Experiments and simulations. J. Journal of Fluids and Structures, 2020, 97, 103083.

13. Hossain M, Chinenye-Kanu N M, Droubi G M, et al. Investigation of slug-churn flow induced transient excitation forces at pipe bend. J. Journal of Fluids and Structures, 2019, 91, 102733.

14. Brackbill J U, Kothe D B, Zemach C. A continuum method for modeling surface tension. J. Journal of computational physics, 1992, 100, 335-354.

15. Menter F R, Kuntz M, Langtry R. Ten years of industrial experience with the SST turbulence model. J. Turbulence, heat and mass transfer, 2003, 4, 625-632.

16. Gamet L, Scala M, Roenby J, et al. Validation of volume-of-fluid OpenFOAM® isoAdvector solvers using single bubble benchmarks. J. Computers & Fluids, 2020, 213, 104722.

17. Abdulkadir M, Hernandez-Perez V, Lo S, et al. Comparison of experimental and Computational Fluid Dynamics (CFD) studies of slug flow in a vertical riser. J. Experimental Thermal and Fluid Science, 2015, 68, 468-483.

18. Dean W R. XVI. Note on the motion of fluid in a curved pipe. J. The London, Edinburgh, and Dublin Philosophical Magazine and Journal of Science, 1927, 4, 208-223.

19. Sudo K, Sumida M, Hibara H. Experimental investigation on turbulent flow in a circular-sectioned 90-degree bend. J. Ex-periments in Fluids, 1998, 25, 42-49.

20. Jurga A P, Janocha M J, Yin G, et al. Numerical simulations of turbulent flow through a 90-Deg pipe bend. J. Journal of Offshore Mechanics and Arctic Engineering, 2022, 144, 061801.

Chapter 4.
Numerical simulations of gas-liquid two-phase flow induced forces at subsea jumpers

Abstract

Rigid jumpers are wildly utilized as a significant component to transport oil and gas between subsea modules in subsea production systems. In general, rigid jumpers consist of elbows and straight pipe sections. Because the produced flow from the subsea wells is a mixture of water, oil and gas polymers, the flow transported inside jumpers usually is multiphase flow and the typical one is gas-liquid two-phase flow. Slug flow is a typical type of gas-liquid two-phase flow in which large gas bubbles are formed and move with the liquid. Oscillatory pressure fluctuation occurs where the large and long gas bubbles are passing, which can result in excitation force and flow-induced vibration on the jumper. In the present study, numerical simulations are carried out to investigate the characteristics of gas-liquid two-phase flow and its induced excitation forces acting on uniplanar and multiplanar jumpers, which are typical forms of jumpers used in subsea. The mesh convergence study is conducted to determine the optimal computational grid resolution. Then, the validation study is conducted against previous published experimental data. The validated numerical model is then applied to investigate gas-liquid two-phase flow inside different jumpers. The results show that the secondary flow phenomena are evident in the downstream of the elbows in the jumper and the excitation forces along the jumpers mainly peak at the elbow sections and the locations where large and long gas bubbles are generated. In the response analysis of the jumpers, fixed supports are applied according to engineering practice. The reaction forces of the supports in the jumpers are mainly in the gravity direction. Moreover, the maximum displacement happens at the upper side of the jumpers and the general deformation is the sinking of the jumper middle. Therefore, the tensile capacity of the upper jumper components is supposed to be considered in the design of both uniplanar and multiplanar jumpers.

Keywords: Multiphase flow; Rigid Jumper; Numerical simulations; Excitation forces; Flow-induced vibration; Reaction forces.

4.1 Introduction

Nowadays, the offshore oil and gas industry turned its attention to subsea oil and gas projects, which promoted the development of subsea oil and gas technology. In subsea oil and gas production systems, the jumper is a significant connector which is utilized to transport oil and gas between subsea components. For rigid jumpers, the structure can be uniplanar or multiplanar, with some bends in the structure. Typically, a secondary flow will be generated after the pipe bending part by the centrifugal force

and frictional effects of the pipe wall. Therefore, secondary flow happens in many parts of the structure for a rigid jumper. Due to the complexity of the oil and gas reservoir, the mixture transported inside the jumper is a multiphase flow such as a gas-liquid two-phase flow. For multiphase flow such as gas-liquid two-phase flow in jumpers, different flow states can occur including bubble flow, slug flow, churn flow, and annular flow. With different superficial gas and liquid velocities (the superficial velocity of one phase is defined as an artificial velocity on the basis that the given phase is the only one on the cross-section), the flow can experience transient states known as slug flow and churn flow. In the slug flow condition, long gas bubbles are generated and move with the liquid, which is called Taylor bubble flow in the pipeline structure. Compared to the slug flow, the gas bubbles in the churn flow state are smaller and the flow becomes more chaotic. Additionally, when the big gas bubbles move along with the liquid in these two states, the two-phase flow will induce pressure fluctuation on the wall of the jumper. This pressure variation may cause fatigue damage to the jumpers and flow-induced vibration (FIV). Therefore, it is crucial to investigate the gas-liquid flow characteristics inside jumpers for subsea engineering to establish a safer design for rigid jumpers. Because a rigid jumper is made up of straight pipes and elbows, some conclusions and findings for flow analysis can be still applied to jumpers. A number of experimental studies on multiphase flow through different pipe configurations have been conducted. Back in the 20th century, Hara (1976) [1], Pettigrew et al. (1994) [2] and Pettigrew et al. (1998) [3] had experimentally investigated the mechanism of FIV caused by multiphase flow in horizontal and vertical pipes. Riverin et al. (2007) [4] investigated the governing vibration excitation mechanism of two-phase flow in pipe and measured vibration response, excitation forces, and fluctuating properties of two-phase flow for different flow patterns. They concluded that the observed vibrations are caused by a resonance phenomenon between periodic momentum flux fluctuations of two-phase flow and the first modes of the piping system. Al-Safran (2009) [5] carried out experiments of gas-liquid two-phase flow in a horizontal pipe to investigate the slug initiation mechanism at the pipe entrance region (entrance effect) and the flow development along the pipe (pipe length effect). According to experimental findings, under high Froude number conditions (>3), fully developed slugs produced by the hydrodynamic slugging mechanism occur less frequently than those produced by the terrain slugging process. On the other hand, under low Froude number situations (Froude number < 3), fully developed slugs produced by the terrain slugging mechanism have a frequency higher than those produced by hydrodynamic slugging. Based on the relevant physical parameters to slug frequency, a new slug frequency correlation and its tuned version are developed using a broad range experimental database, which revealed good results of average percent error and standard deviation against an independent data set. Dinaryanto et al. (2017) [6] experimentally studied the gas-liquid slug two-phase flow in a horizontal pipe and the flow mechanisms of initiation and development. As a result, the main several basic mechanisms of slug flow initiation in a horizontal pipe are wave coalescences, the wave growth mechanism, and the large disturbance waves. To address these mechanisms, a flow initiation map was proposed based on experimental data. More recently, an experiment of two-phase pipe

flow was performed by Carvalho et al. (2020) [7] to investigate the flow pattern classification. They developed a novel algorithm using the vibration signal from a vertical pipe conveying a liquid-gas two-phase flow to determine the flow pattern with the analysis of the frequency domain and time domain. The results showed that it was possible to accurately identify the flow pattern in two-phase liquid-gas vertical flows.
Besides experiments, gas-liquid two-phase flow in pipe has been widely investigated by numerical simulations in Da Riva et al. (2009) [8], Bossio et al. (2014) [9], Araújo et al. (2015) [10] and Parsi et al. (2016) [11]. In contrast to the numerical analysis of multiphase flow in pipe, the numerical studies on jumper are few and most of them are studies on uniplanar jumpers carried out by Pontaza et al. (2011) [12], Chica (2017) [13], Bruschi et al. (2017) [14] and Kim et al. (2018) [15]. Zhu et al. (2022) [16] numerically studied the multiphase flow-induced vibration of an M-shape jumper using a two-way fluid-structure interaction approach. It was concluded that the out-of-plane response of the jumper midspan is suppressed with a reducing gas-liquid ratio while the in-plane response is enhanced. In contrast, both the in-plane and out-of-plane fluctuations of the jumper midspan are amplified with the increase of mixture velocity. Li et al. (2022) [17] conducted experimental and numerical studies to investigate the gas-liquid flow and the induced vibration in a multiplanar jumper. They performed the one-way coupling numerical simulations and validated the simulations against the experimental data based on the flow patterns and the flow-induced vibrations. Their studies proved that both the pressure fluctuations and vibration amplitudes are strongly relevant to the gas content rate, mixture velocity, and the gas and liquid superficial velocity.

The objective of the present study is to investigate the characteristics of gas-liquid two-phase slug flow, the flow-induced vibrations, and the corresponding excitation force acting on jumpers. Numerical simulations based on the volume of fluid (VOF (1981) [18]) methods and the one-way fluid-solid coupling are performed to analyze the interactions between the gas-liquid two-phase flow and the jumper. The paper is organized as follows. The governing equations of the gas-liquid two-phase flow are briefly introduced in Section 2. The computational setups are concretely shown in Section 3, including the numerical simulation models in OpenFOAM and Code Aster. The flow characteristics of the gas-liquid flow in jumpers and the structural responses due to the flow-induced excitation forces are presented and discussed in Section 4. Finally, conclusions are made in Section 5.

4.2 Methodology

The characteristics of gas-liquid two-phase flow have been extensively studied by computational fluid dynamics (CFD) methodologies. In the present study, the k-ω Shear-Stress Transport (k-ω SST) model is utilized to resolve the turbulence stress, and the VOF model is employed to demonstrate the interface between the gas and liquid flow.

4.2.1 VOF model

In the VOF model, the two phases of gas and liquid share a single set of momentum equations, and the tracking of the gas-liquid interface is achieved by solving a continuity equation [19]. Here are the governing equations for the VOF model:

The continuity equation of the fluids is given as:

$$\frac{\partial \rho}{\partial t} + \nabla \cdot (\rho \bar{\boldsymbol{u}}) = 0, \tag{4.1}$$

where ρ is the density, t is the time and $\bar{\boldsymbol{u}}$ is the velocity vector of the fluid.

The momentum equations of the fluids are given as:

$$\frac{\partial (\rho \bar{\boldsymbol{u}})}{\partial t} + \nabla \cdot (\rho \bar{\boldsymbol{u}} \bar{\boldsymbol{u}}) = -\nabla \cdot P + \nabla \cdot \mu (\nabla \bar{\boldsymbol{u}} + \nabla \bar{\boldsymbol{u}}^T) - S, \tag{4.2}$$

where P is the pressure in the flow field, μ is the dynamic viscosity of the fluid and F is the surface tension force.

To track the interface between two phases, an additional volume continuity equation for each phase is given and solved below:

$$\frac{\partial \alpha_q}{\partial t} + \bar{\boldsymbol{u}} \cdot \nabla \alpha_q = 0, \tag{4.3}$$

where q represents each phase component.

The volume fractions of the two phases satisfy the equation:

$$\sum_{q=1}^{2} \alpha_q = 1, \tag{4.4}$$

The density ρ of the fluids can be represented as:

$$\rho = \sum_{q=1}^{2} \alpha_q \rho_q, \tag{4.5}$$

where ρ_1 represent the density of the liquid phase (also denoted as $\rho_l = 10^3\ \mathrm{kg/m^3}$) and ρ_2 represent the density of the liquid phase (also denoted as $\rho_g = 1\ \mathrm{kg/m^3}$).

The continuum surface force (CSF (1992) [20]) model is used to compute the surface tension force S between gas and liquid phase in Equation (4.2) as a source term given as:

$$S = \sigma \left[\frac{\rho k_1 \nabla s_1}{1/2(\rho_l + \rho_g)} \right], \tag{4.6}$$

where σ represents the surface tension coefficient and k_1 represents the surface curvature.

4.2.2 Turbulence model

In the present study, the turbulence stress is resolved for both the liquid and gas phases using the $k-\omega$ SST model. The $k-\omega$ and $k-\varepsilon$ models are combined in this turbulence model. The $k-\omega$ model of Wilcox (1998) is utilized for the region close to the walls, whereas the $k-\varepsilon$ model of Jones and Launder (1973) is used for the region of free-stream flow, such as the center of the pipe flow. The turbulence viscosity is computed by:

$$\mu_t = a_1 \frac{\rho k}{max\,(a_1\omega, SF_2)} \tag{4.7}$$

The turbulent kinetic energy k is given by solving the equation of:

$$\frac{\partial(\rho k)}{\partial t} + \nabla \cdot (\rho k \bar{\boldsymbol{u}}) = \nabla \cdot \left[(\mu + \frac{\mu_t}{\sigma_k})\nabla k\right] - \beta^* \rho k \omega + S_k, \tag{4.8}$$

where S_k is shear production term obtained by:

$$S_k = \mu_t \nabla \bar{\boldsymbol{u}} \cdot (\nabla \bar{\boldsymbol{u}} + (\nabla \bar{\boldsymbol{u}})^T). \tag{4.9}$$

The turbulence specific dissipation rate ω is obtained by solving the equation of:

$$\frac{\partial(\rho\omega)}{\partial t} + \nabla \cdot (\rho\omega \bar{\boldsymbol{u}}) = \nabla \cdot \left[\left(\mu + \frac{\mu_t}{\sigma_{\omega,1}}\right)\nabla\omega\right] + \gamma_2 \left(2\rho S_{ij}^2 - \frac{2}{3}\rho\omega \frac{\partial u_i}{\partial x_j}\delta_{ij}\right) - \beta_2 \rho(\omega)^2 + 2\frac{\rho}{\sigma_{\omega,1}\omega}\frac{\partial k}{\partial x_k}\frac{\partial \omega}{\partial x_k} \tag{4.10}$$

The open-source CFD software package OpenFOAM is applied to implement and solve the set of governing equations of $\mathrm{k}-\omega$ SST model. Other constants such as α_{k1}, α_{k2}, $\alpha_{\omega1}$, $\alpha_{\omega2}$, β_1, β_2, γ_1, γ_2, β^*, a_1, b_1, c_1 can be found in Menter et al. (2003) [21].

4.2.3 Structural model

The pipeline structure in the present study can be modeled as the Euler-Bernoulli beam because the pipeline's diameter is small relative to its length. The gas-liquid two-phase flow-induced forces acting on the walls of the pipeline and the induced structural responses are computed in the three-dimensional coordinate system. The structural dynamic equation is obtained by:

$$\mathbf{M}\ddot{\mathbf{u}}(t) + \mathbf{C}\dot{\mathbf{u}}(t) + \mathbf{K}\mathbf{u}(t) = \mathbf{P}(t) \tag{4.11}$$

where $\mathbf{M}$, $\mathbf{C}$ and $\mathbf{K}$ denote mass, damping, and stiffness matrices; while $\ddot{\mathbf{u}}(t)$, $\dot{\mathbf{u}}(t)$ and $\mathbf{u}(t)$ denote accelerations, velocities, and displacements vectors, respectively. $\mathbf{P}(t)$ denotes the load vectors acting on the pipelines, which are obtained from the fluid solver.

Several presumptions are made in the analysis of fluid-solid interaction in the current study: (1) since the structural damping is negligible, $\mathbf{C} = \mathbf{0}$; (2) the matrices mentioned above are time-invariant in the pipeline systems; (3) similar to the previous studies such as Wang et al. (2018) [22], a one-way coupling between the fluid and the structure is assumed. Consequently, the effects of the structural dynamic responses of the structure on the flow field are not taken into account.

4.3 Computational setup

4.3.1 Computational domain and numerical methods

In the present study, the pipe diameter (D) and the 90-degree elbow curvature radius (r) are set the same as the experimental setups of Li et al. (2022) [17], in which $D = 48$ mm and $r = 120$ mm, respectively. Two different jumper configurations are studied. One is a uniplanar jumper and the other one is a multiplanar jumper. The

geometries of the different jumper configurations are shown in Figure 4.1. The open-source CFD code, OpenFOAM-v2012, is employed to carry out the numerical simulations based on the finite volume method. A multiphase solver named interIsoFoam is utilized for the two-phase flow, which combines the Pressure Implicit with Splitting of Operators (PISO) and Semi-Implicit Method for Pressure Linked Equations (SIMPLE) algorithms for pressure-velocity coupling. The solver interIsoFoam is a modification of the VOF solver interFoam and uses the isoAdvector method, which can maintain a sharper surface and reduce the dissipation compared with the solver interFoam according to Gamet et al. (2020) [23].

The computational domains and the length of different jumper sections for the simulations are shown in Figure 4.1 as well. The two different configurations are named Jumper A and B in the present study. The same configurations and geometry of jumpers are utilized for the dynamic response analysis in Code Aster.

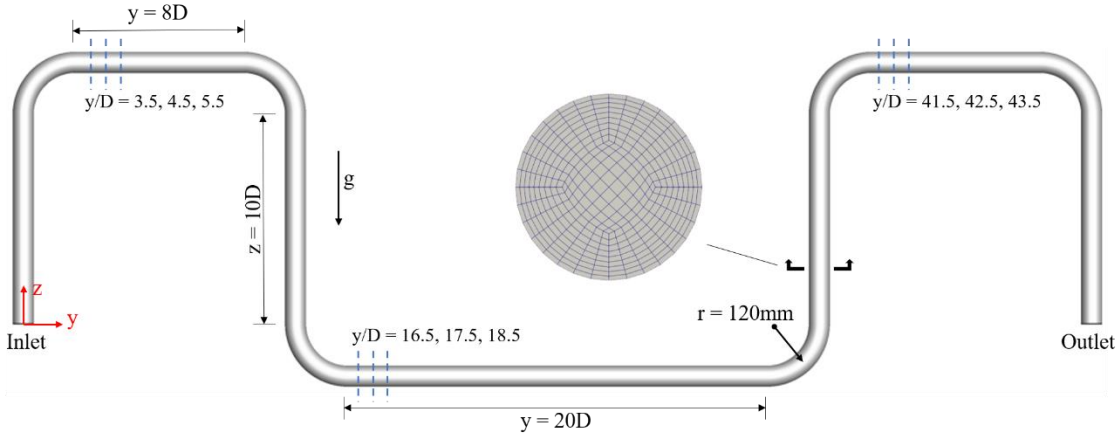

(a) Jumper A

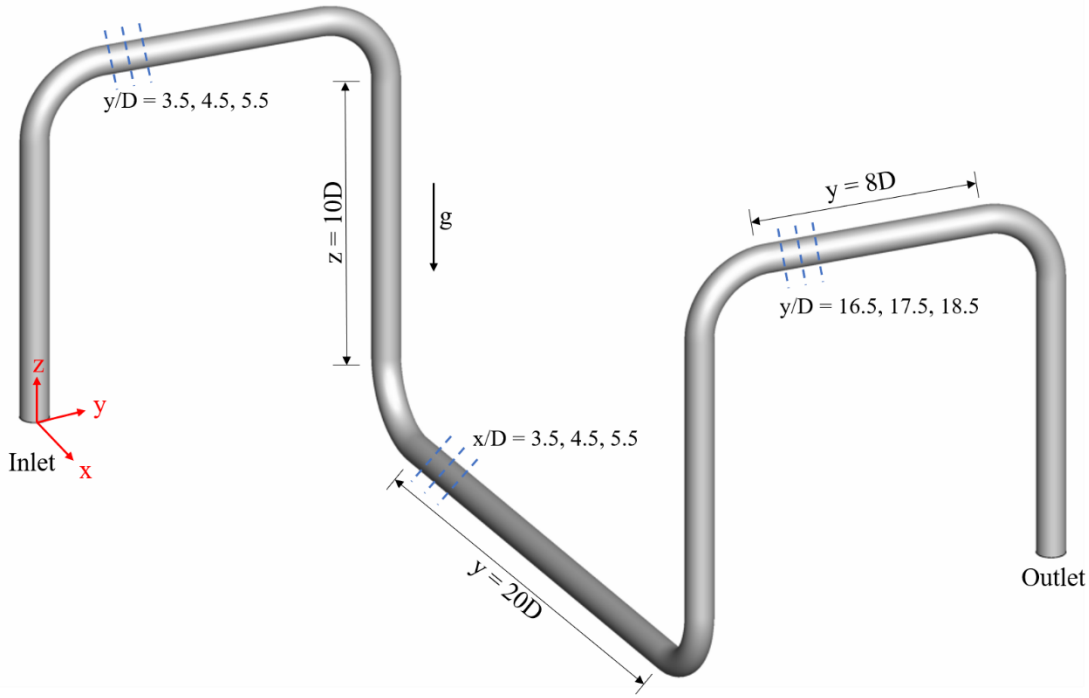

(b) Jumper B

Figure 4.1. The computational domains for different jumper configurations and the meshes in the cross-sectional plane.

4.3.2 Boundary conditions

The boundary conditions of the numerical simulations are shown in Table 4.1.

Table 4.1. Boundary conditions of CFD simulations in OpenFOAM

Surface domain	Inlet	Outlet	Pipe
U	fixedValue	pressureInletOutletVelocity	fixedValue
P	fixedFluxPressure	fixedValue	zeroGradient
k	fixedValue	zeroGradient	kqRWallFunction
ν_t	calculated	calculated	nutkWallFunction
ω	fixedValue	zeroGradient	omegaWallFunction
α	codedFixedValue	inletOutlet	zeroGradient

The void fraction α and velocity U are used to describe the gas injection in the gas-liquid flow at the vertical inlet. The superficial velocities of the gas and liquid are defined respectively as

$$U_{sg} = \frac{Q_g}{A}, \tag{4.12}$$

$$U_{sl} = \frac{Q_l}{A}, \tag{4.13}$$

where Q_g and Q_l denote the volume rates of the gas and the liquid phase respectively and A is the cross-section area of the pipe.

The void fractions α_g and α_l for the two phases are defined as

$$\alpha_g = \frac{A_g}{A}, \tag{4.14}$$

$$\alpha_l = \frac{A_l}{A}, \tag{4.15}$$

where A_g and A_l denote the cross-section area occupied by the gas and liquid phase respectively. For every cross-section along the jumper, there is $A = A_g + A_l$. An example of the gas and liquid phase injection at the inlet is shown in Figure 4.2. The flow velocity U in Table 1 is defined as $U = U_{sg} + U_{sl}$.

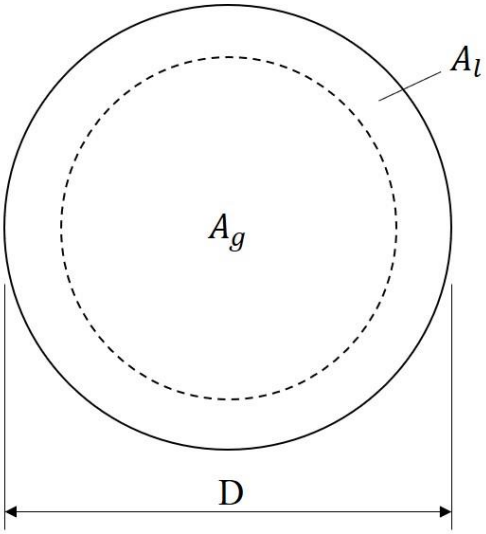

Figure 4.2. Configuration of gas and liquid phase in inlet cross-section area

In the structural responses analysis, the jumpers are modeled using consistent beam elements in Code Aster. According to the engineering practice, fixed supports are applied at the inlet and outlet of the jumpers, which are shown in Figure 4.3. The element numbers for Jumper A and B are all 756. The material of the jumpers is stainless steel with a wall thickness of $t = 2\,\mathrm{mm}$, a density of $\rho = 7850\,\mathrm{kg/m^3}$, Young's modulus $E = 206\,\mathrm{GPa}$, total length of $L = 3.66\,\mathrm{m}$ and poison ratio of 0.3. The solution technique for Eq. (4.11) is based on the unconditionally stable HHT-α method (1977).

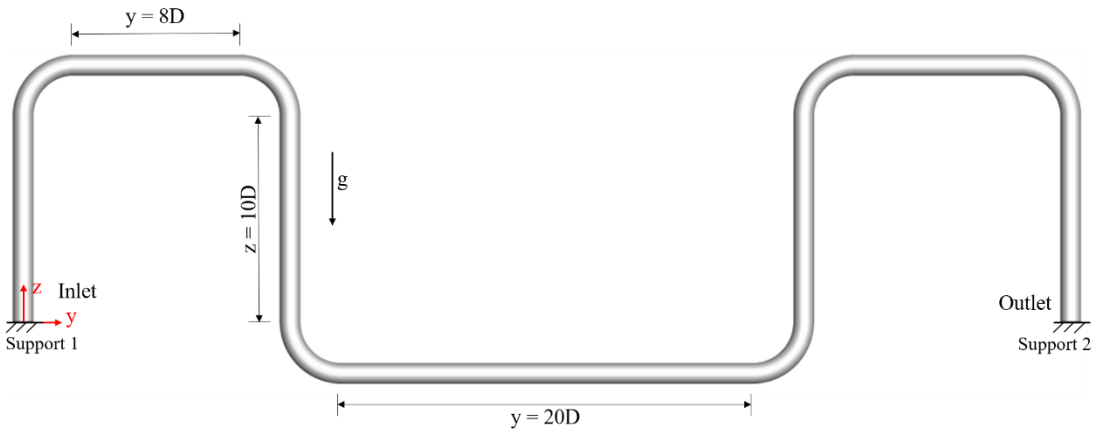

(a) Jumper A

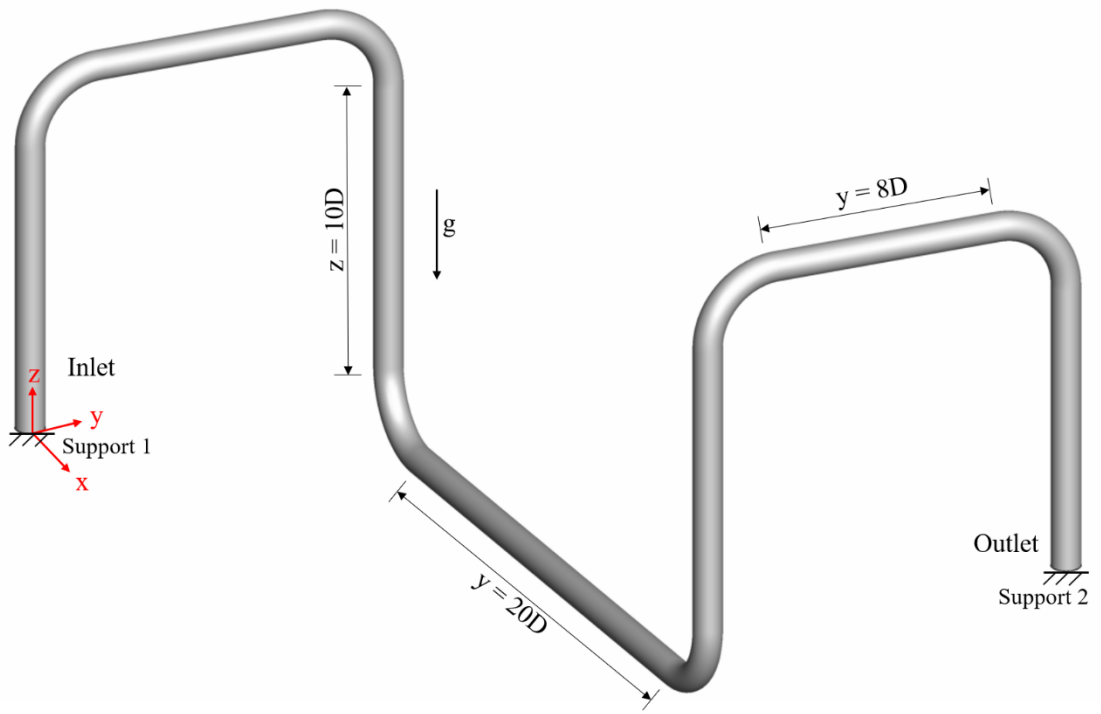

(b) Jumper B

Figure 4.3. Configurations of fixed supports for different jumpers.

4.4 Results

4.4.1 Mesh convergence studies and validation studies

The mesh convergence studies have been carried out by using four different meshes for the slug flow in a pipeline shown in Figure 4.4. The superficial gas and liquid velocities are set as 1.61 m/s and 0.91 m/s, respectively. The number of cells selected for the three different meshes named as Mesh 1, Mesh2 Mesh 3 and Mesh 4 are 338000, 475000, 612000 and 796000 respectively. The simulation time is 8s which ensures the flow can fully develop and more available data. The time-step of the simulation is adjustable and set as 10^{-5} initially. The maximum Courant number is set as 0.2 for all simulation cases. As shown in Figure 4.4, the void fraction at position CP5 is computed and used for the subsequent post-processing. Figure 4.5 shows the time histories of the void fraction at CP5 for the four different meshes. The elapsed time of simulations are 405000s, 523000s, 604000s and 712000s for Mesh 1, Mesh 2 Mesh 3 and Mesh 4 respectively. Although the temporal evolutions of the void fractions for the four meshes are different, it is normal that the instantaneous fluctuations of the two-phase flow can vary with different meshes according to Tocci (2016) [24] and Hossain et al. (2019) [19]. The results of the mean value and the relative difference of the mean value for different meshes are shown in Table 4.2. The deviation of the mean value reduces to less than 1% for Mesh 3, therefore Mesh 3 can be regarded as sufficient to provide an appropriate grid resolution. Moreover, Figure 4.6 shows the power spectra density (PSD) of the void fraction of Mesh 3 at CP5 compared with the experimental

data obtained by Saidj et al. (2014) [25]. A similar peak value at around $f = 2.5$ Hz can be observed. Therefore, considering the results and the computational cost, the numerical model based on the grid resolution of Mesh 3 can be applied for the simulation and will be employed for the subsequent simulations.

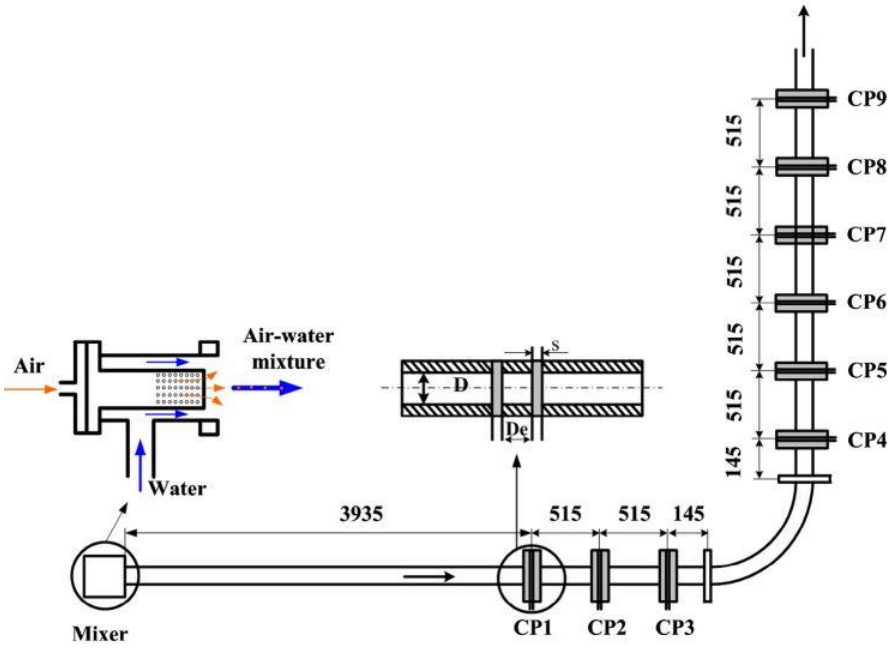

Figure 4.4. Configuration of pipeline and probe position from Saidj et al. (2014) [25].

Table 4.2. Mean value and its deviation of void fraction for different meshes

Index	Mesh 1	Mesh 2	Mesh 3	Mesh 4
Number of cells	338000	475000	612000	796000
Mean	0.4760	0.4860	0.4823	0.4838
Deviation	/	2.1%	0.76%	0.31%

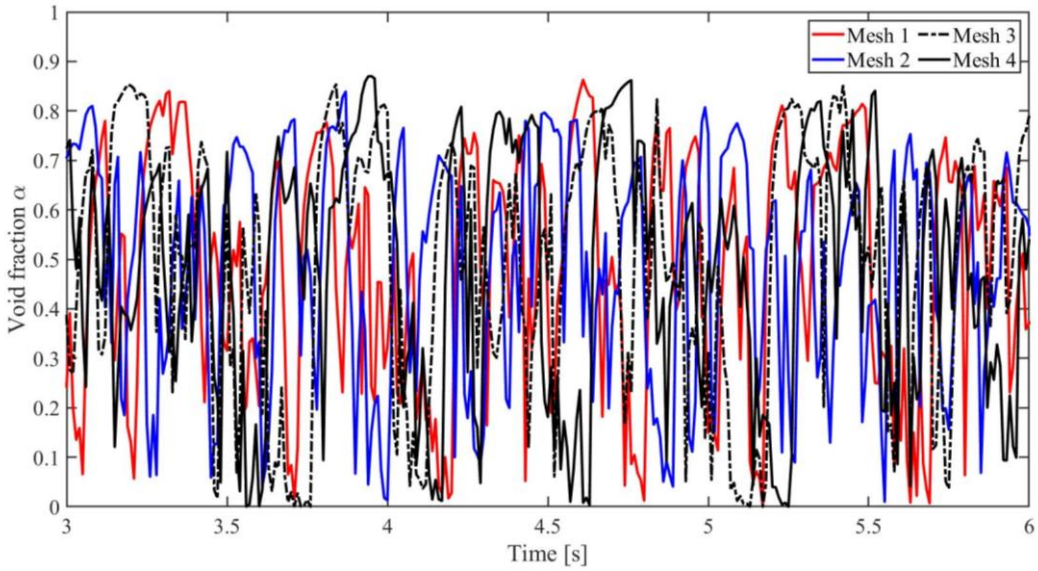

Figure 4.5. Time series of void fraction for different meshes at CP5 with time.

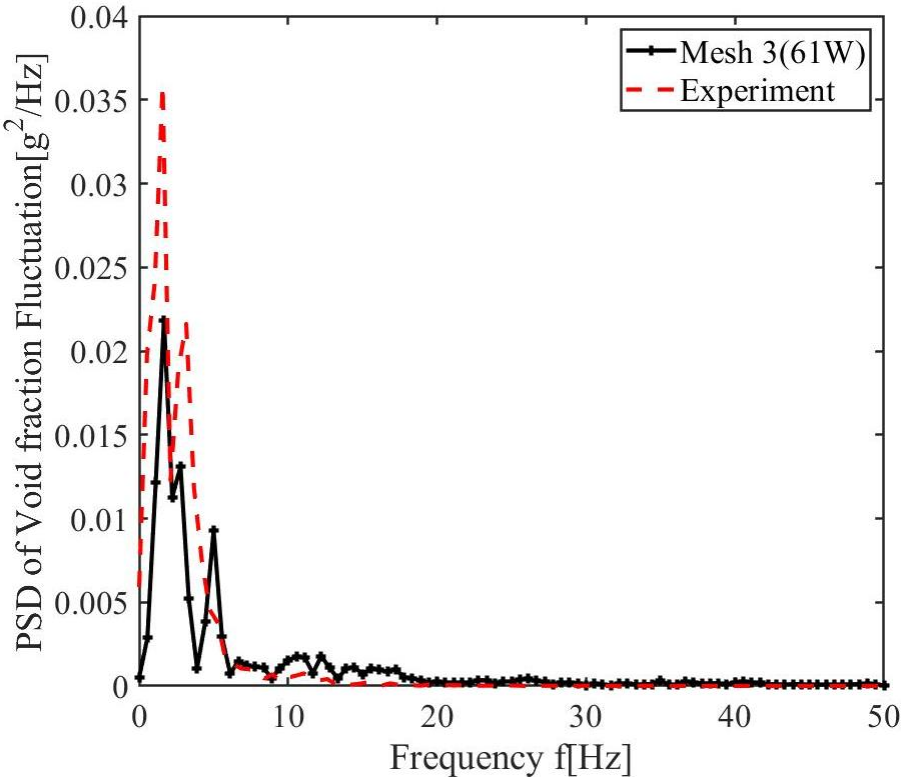

Figure 4.6. Comparison of PSD (power spectral density) of the void fraction obtained using Mesh 3 and the experimental data reported by Saidj et al. (2014) [25].

4.4.2 The volume fraction of the two-phase pipe flow

The results of the volume fraction of the fully developed slug flow in Jumper A after 3s are shown in Figure 4.7. The flow goes through the outlet for the first time at 3s, and after the first 3s, the effect of the first loop can be ignored and the flow pattern

is stationary. The flow with the liquid and the gas is injected vertically at the inlet as shown in Figure 4.2. The blue regions in Figures 4.7 and 4.9 are presented as the gas phase. A series of small gas bubbles are progressively generated and oscillate close to the inlet. When the small gas bubbles arriving the first horizontal straight pipe component, they begin to accumulate and attach to the upper side of the internal pipe wall because of the density distinction between gas and liquid phases. Subsequently, the gas phase is accelerated at the second vertical straight pipe component because of the gravity and plugs at the third elbow. After the third elbow, the flow starts to stratify again and a long and continuous gas bubble is formed as denoted in Figure 4.7, where the slugging phenomena are the most obvious compared with other parts of the pipeline. When the long and continuous gas bubble passes the fourth elbow, it begins to break and the Taylor bubble (as denoted in Figure 4.7) subsequently appears in the third vertical straight pipe component. The next development is similar to the previous one, where the Taylor bubble splits after the fifth elbow and the gas phase gathers again and accelerates at the fourth vertical straight component to the outlet of Jumper A.

The three-dimensional characteristics of the gas phase in Jumper A after 3s are displayed in more detail in Figure 4.8 by using the iso-surfaces of α = 0.5 (which is denoted as the interface between the gas and liquid) colored by the local flow velocity magnitudes. It is obvious that the velocity magnitude decreases when the flow passes the elbows, which can lead to a large pressure and the corresponding fluctuation at the elbows. As has been discussed above, the velocity magnitude of the gas phase is large where the gas phase accelerates especially in the middle of the jumper. For a single Taylor bubble, as denoted in Figure 4.8, the velocity magnitude of the head is larger than that of the tail due to gravity and the interaction of the liquid phase. The distribution of velocity magnitude in this way may result in the elongation of the Taylor bubble.

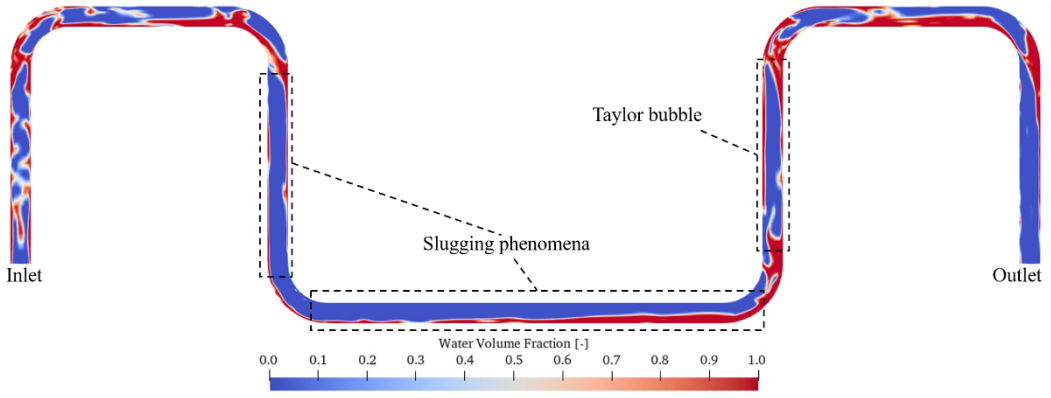

Figure 4.7. Contours of the water volume fraction in Jumper A under a superficial gas velocity of 0.978 m/s and a superficial liquid velocity of 0.61 m/s after 3s.

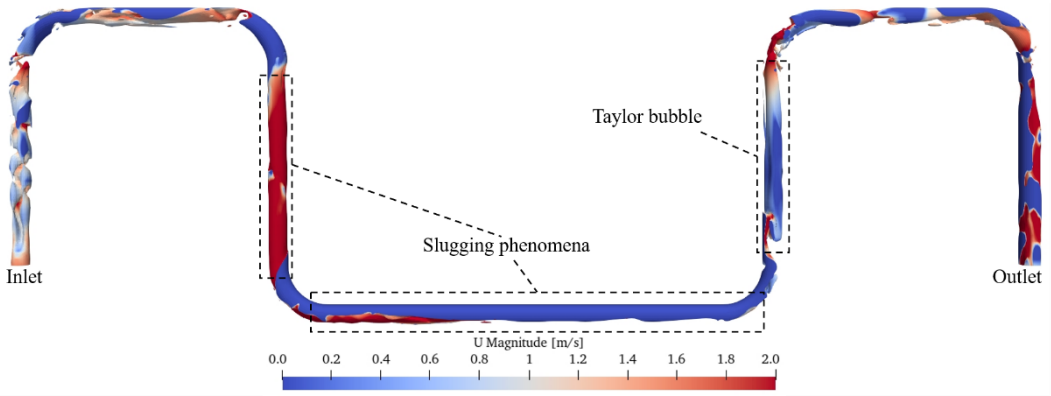

Figure 4.8. Velocity distribution in the iso-surface plot of void fraction in Jumper A under the superficial gas velocity of 0.978 m/s and superficial liquid velocity of 0.61 m/s after 3s.

The results of the fully developed slug flow in Jumper B after 3s are displayed in Figures 4.9 and 4.10. Comparing Figure 4.7 and 4.9, the developments of the gas phase in the two types of jumpers are generally similar. Slugging phenomena occur in the middle of the jumper and Taylor bubbles are generated at the subsequent pipe components. While in Jumper B, the formation of Taylor bubbles seems more frequently compared with Jumper A according to Figure 4.7-4.10. In addition, it is worth noting that more gas phase accumulates at the first four elbows compared with the final two elbows. A possible reason for this phenomenon can be the formation of Taylor bubbles at the final two elbows. It can be observed from Figure 4.8 and 4.10 that Taylor bubbles are generated by shedding from a continuous long gas phase because the velocity magnitude of the core at the tail of the Taylor bubbles is large and similar to the head of the subsequent gas phase. The different distribution of gas phase at elbows will lead to different pressure fluctuations and finally affect the response of jumpers.

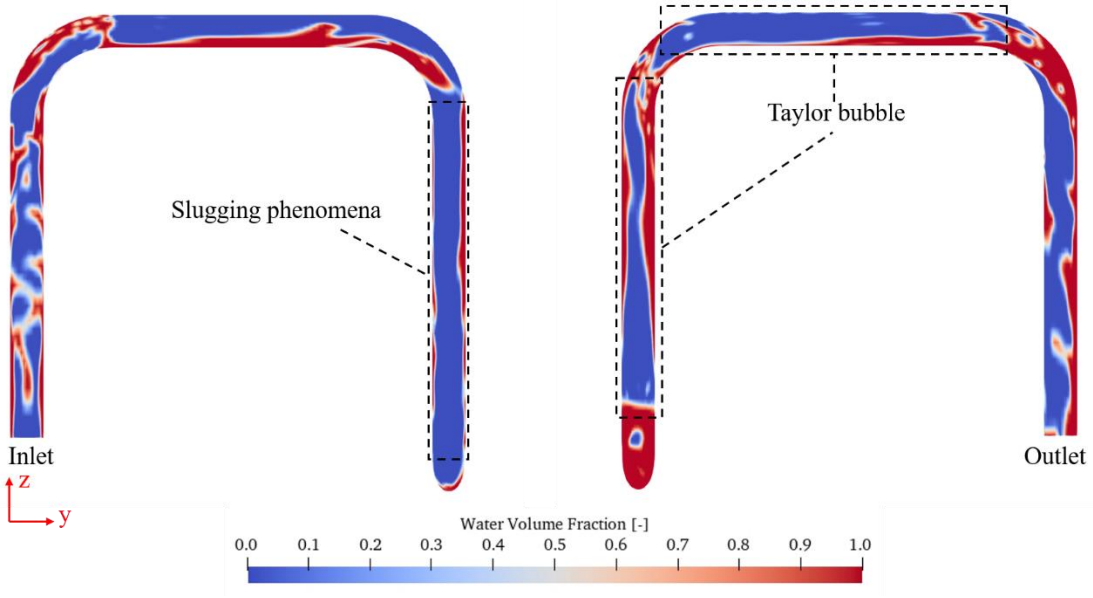

(a) Front-view

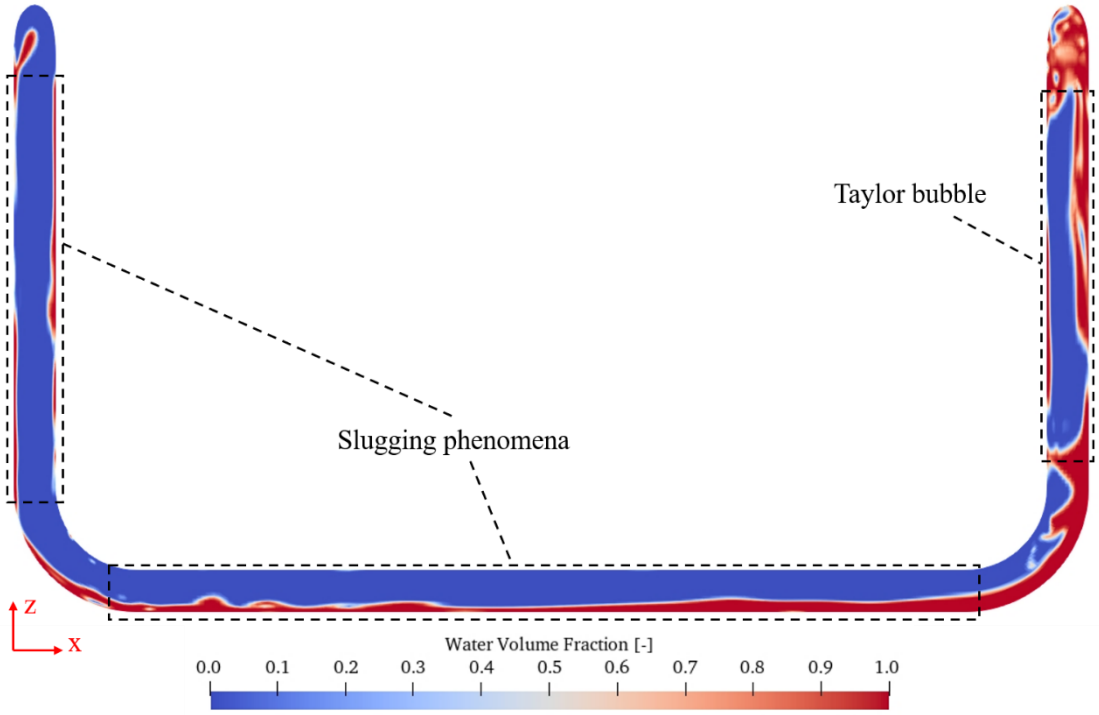

(b) Left-view

Figure 4.9. Contours of the water volume fraction in Jumper B under a superficial gas velocity of 0.978 m/s and a superficial liquid velocity of 0.61 m/s after 3s.

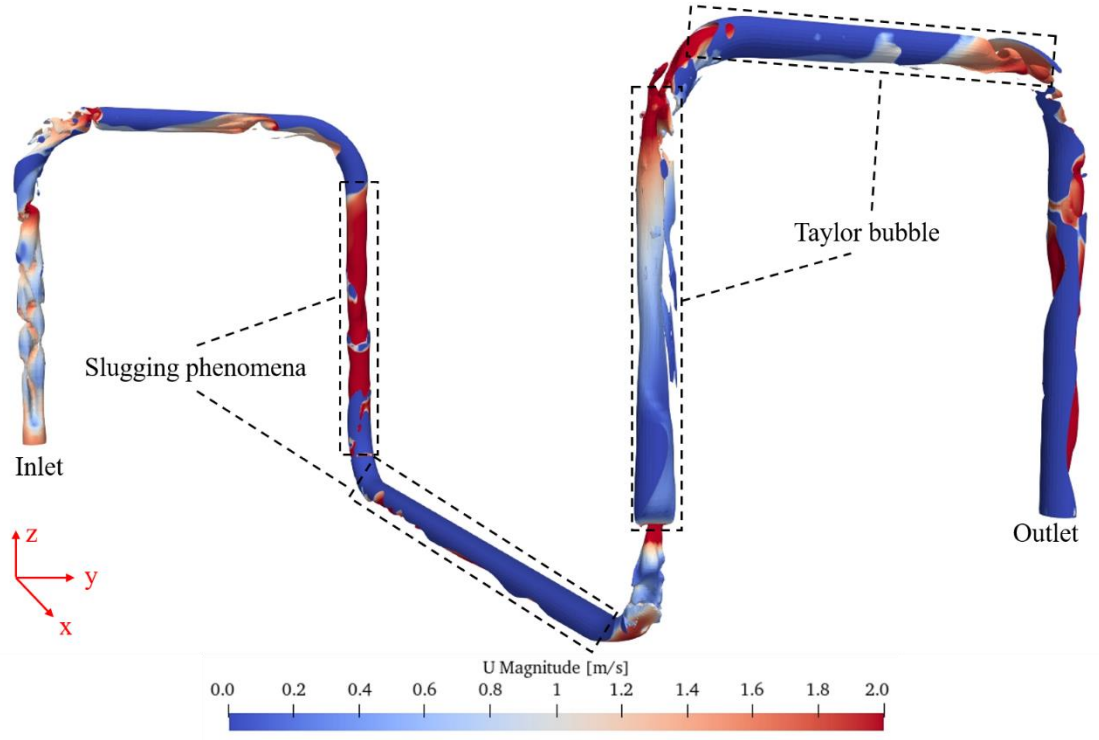

Figure 4.10. Velocity distribution in the iso-surface plot of void fraction in Jumper B under the superficial gas velocity of 0.978 m/s and superficial liquid velocity of 0.61 m/s after 3s.

Figure 4.11 shows the streamlines and the contours of tangential velocity on different sections (Refer to Figure 4.1) of different jumpers. For a single-phase flow through a pipe bend, the secondary flow behind a bend part is a significant phenomenon according to various previously published studies such as Dean (1927) [26], Sudo et al. (1998) [27]. Tangential velocity, which can be utilized to evaluate the strength of the secondary flow, is defined as the vector sum of component velocities in a specific cross-section plane. Because rigid jumpers consist of elbows and straight pipe components, secondary motions can also occur for gas-liquid two-phase flow through a jumper. In the downstream region of elbows, the cross-sectional secondary motions of gas-liquid two-phase flow are evident in Jumper A and B. For a single-phase flow, the distribution of vortex cores at the cross-section is symmetrical. However, compared with single-phase flow, the vortex cores of two-phase flow downstream are more randomly distributed which are affected by the movement of gas phase and phase stratification. Moreover, for Jumper A, the development from multiple focuses to in-plane vortices can be observed at $y/D = 3.5$, $y/D = 4.5$ and $y/D = 5.5$. In the middle of Jumper A, the in-plane recirculation is strong where the slugging phenomena occur. After the fourth elbow, the small vortices close to the pipe wall tend to move towards the center of the section and merge into bigger ones in Jumper A. For Jumper B, in-plane vortices are strong at the observed locations, especially in the middle. In the middle of Jumper B, a large vortex core is near the section center and surrounded by smaller ones, which are forced toward the pipe wall. A similar phenomenon occurs after the fourth elbow in Jumper B, where the smaller vortex core is squeezed by the larger one and moves toward the pipe wall.

(a) Jumper A

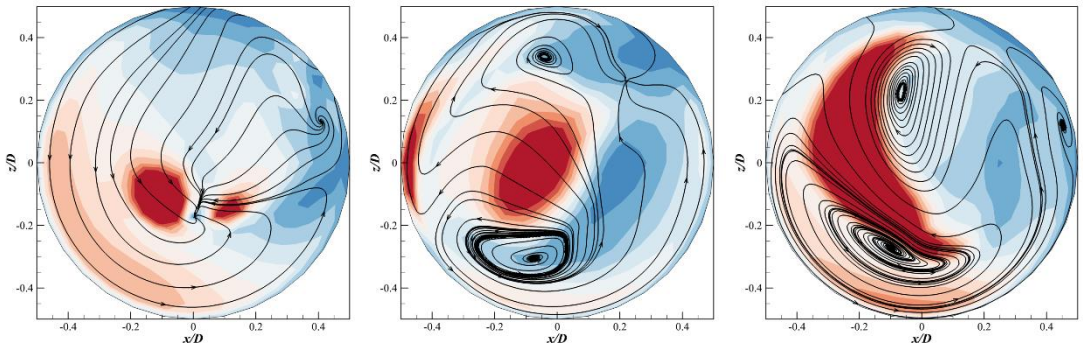

y/D = 3.5 y/D = 4.5 y/D = 5.5

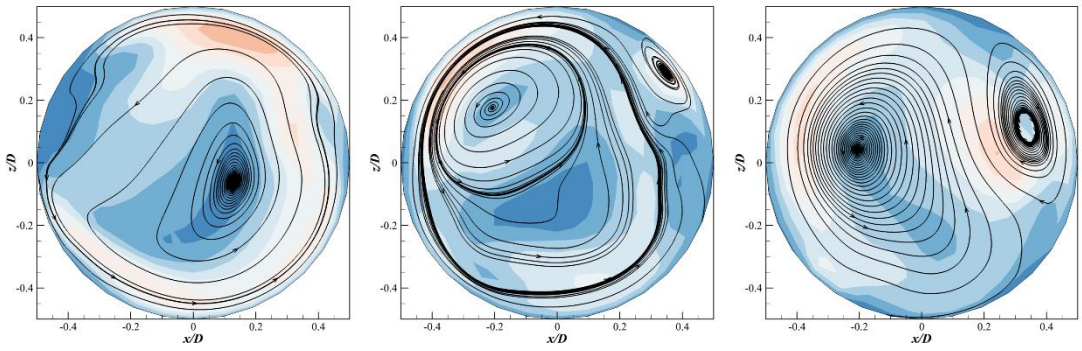

y/D = 16.5 y/D = 17.5 y/D = 18.5

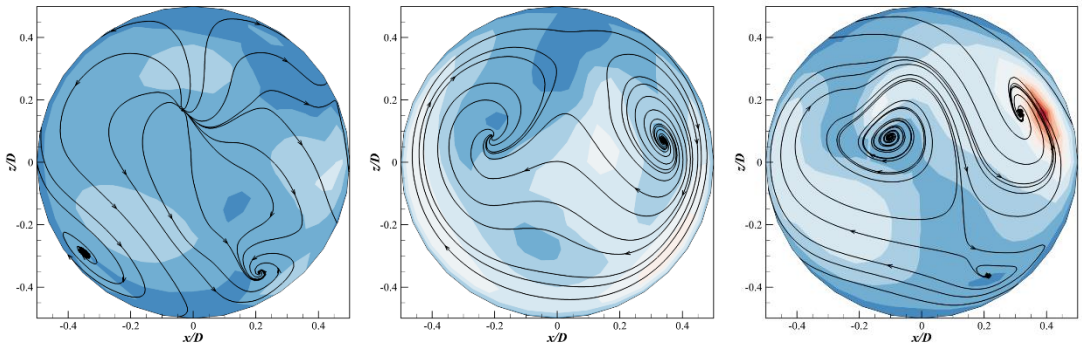

y/D = 41.5 y/D = 42.5 y/D = 43.5

(b) Jumper B

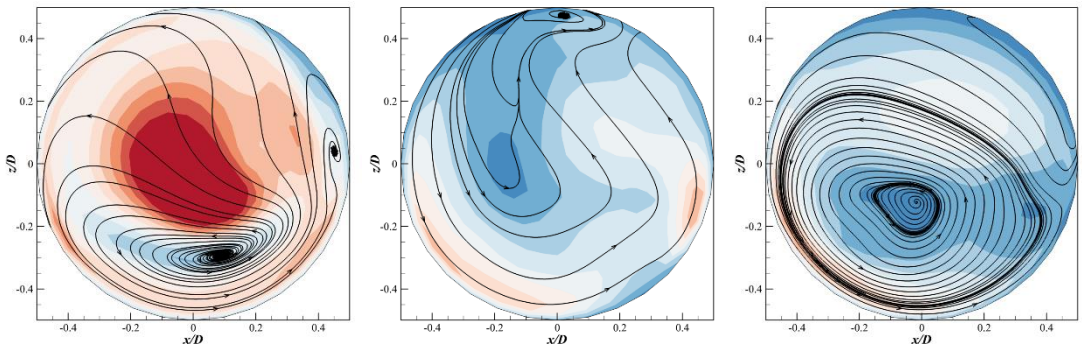

y/D = 3.5 y/D = 4.5 y/D = 5.5

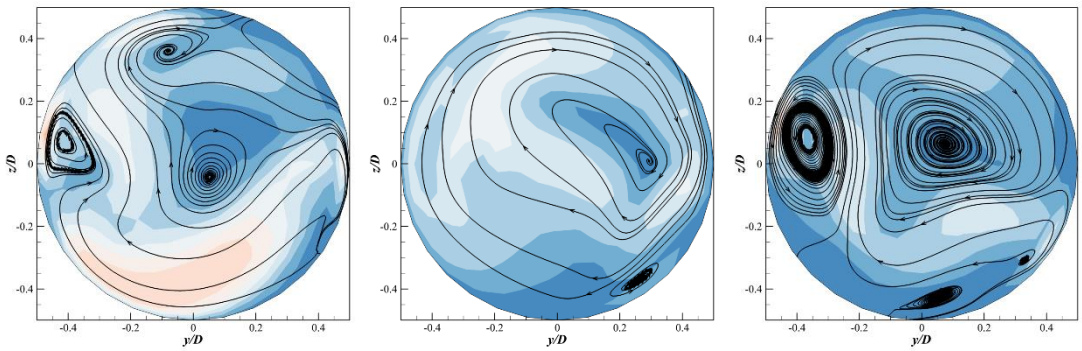

x/D = 3.5 x/D = 4.5 x/D = 5.5

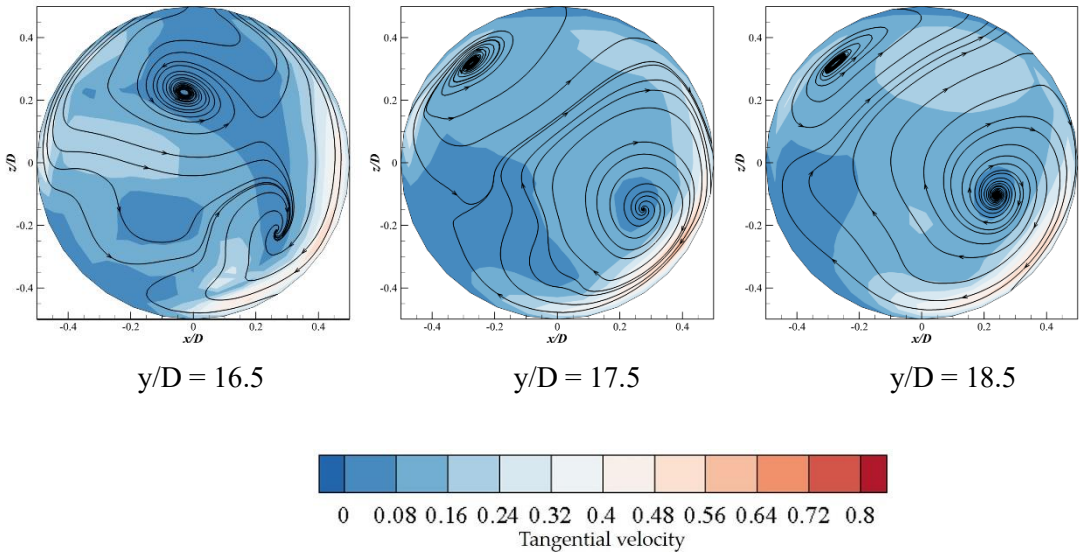

Figure 4.11. Streamlines and the contours of tangential velocity at different axial locations of different pipelines after 5s.

4.4.3 Two-phase flow induced forces

In the present study, a one-way coupling method is utilized for the analysis of the two-phase flow-induced forces acting on the jumpers and the resulting structural response. The forces acting on the jumpers are obtained based on internal pressure. The results of the excitation forces along the jumpers at three representative time steps of $t = 3\text{s}$, $t = 4\text{s}$, and $t = 5\text{s}$ are shown in Figures 4.12 and 4.13. Dimensionless distance d/L is defined as the ratio of the distance from the starting point along the jumper's central line to the total length of the jumper. The starting point is at the inlet. It should be mentioned that $t = 3\text{s}$ is the time step when the two-phase flows inside Jumper A and B just reach the outlet while at $t = 4\text{s}$ and $t = 5\text{s}$ the flow is fully developed.

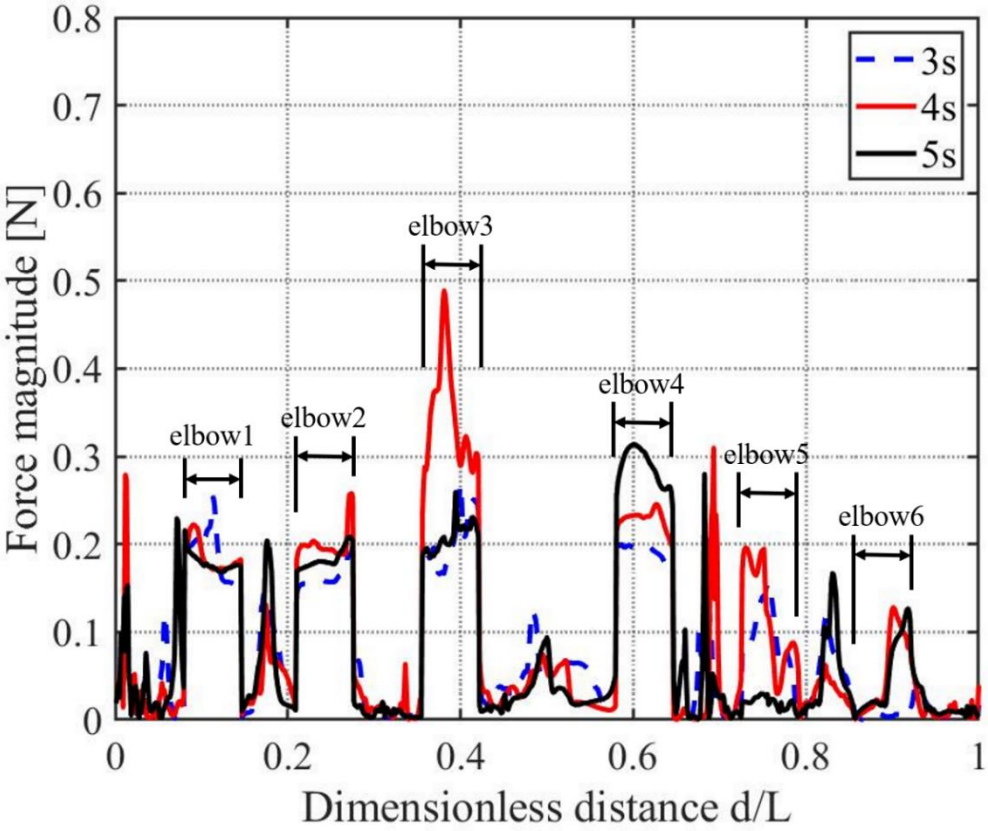

Figure 4.12. The magnitude of force acting on Jumper A under internal pressure at $t = 3\text{s}$, $t = 4\text{s}$ and $t = 5\text{s}$.

The distribution of the force magnitudes along Jumper A at $t = 3\text{s}$, $t = 4\text{s}$ and $t = 5\text{s}$ are shown in Figure 4.12. The fluctuations of the force magnitude along Jumper A are mostly distributed close to the elbow sections, which shows a strong correlation with the result of the water volume fraction in Jumper A shown in Figure 4.7. A larger fluctuation of the force magnitude means a larger gas phase passing the section, especially at the elbow sections. According to Figures 4.7 and 4.8, the gas phase tends to accumulate at the first four elbows, especially the third elbow, which explains the dominant fluctuations happen at most of the elbow sections. For the third elbow, the fluctuation of the force magnitude is the maximum along Jumper A because a severe slugging phenomenon also occurs at the location. Between the fourth and fifth elbows where the Taylor bubble is formed, the magnitude of the excitation forces in Jumper A suddenly increases, which indicates that the Taylor bubbles can result in a larger excitation force. It is evident that the magnitude fluctuation of the excitation forces in Jumper A decreases rapidly close to most of the elbows. This sudden decrease of the excitation force can be likely caused by the shedding of the gas phase from the pipe wall when it passes the outlet of the elbow.

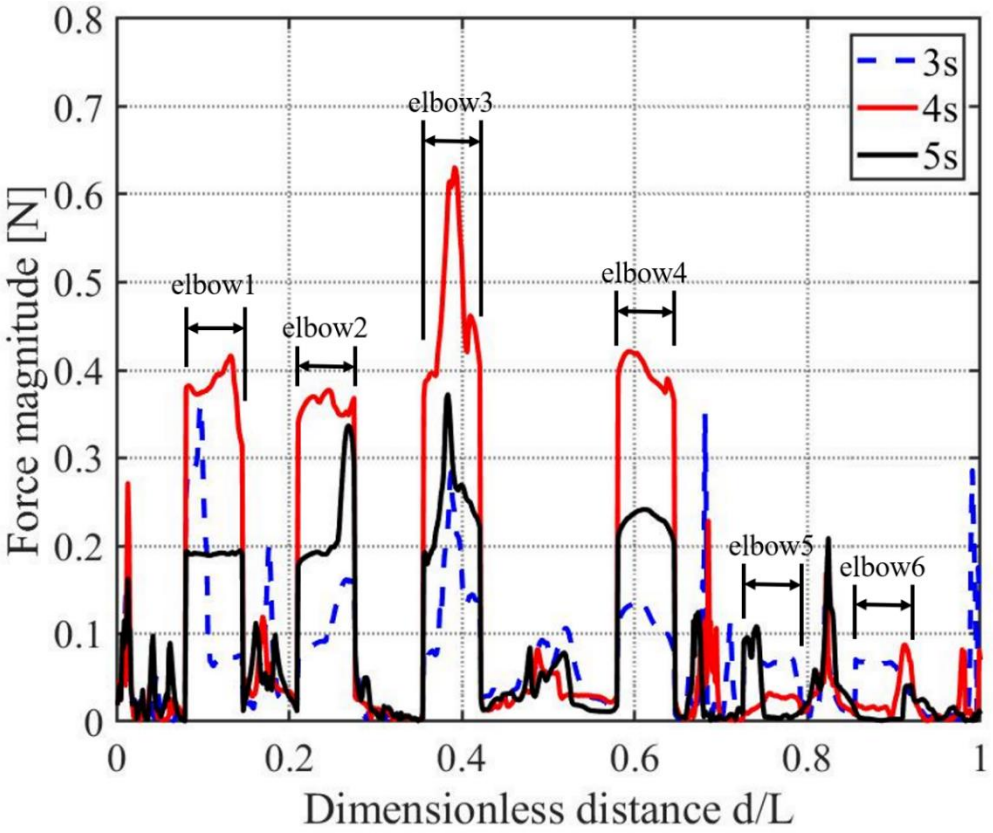

Figure 4.13. The magnitude of force acting on Jumper B under internal pressure at $t = 3\text{s}$, $t = 4\text{s}$ and $t = 5\text{s}$.

According to the excitation force result presented in Figure 4.13, the main tendency of the force magnitude in Jumper B is similar to that in Jumper A. Most of the large fluctuations of excitation force occur at the elbows and the locations where the Taylor bubbles pass through. Moreover, for both Jumper A and B, the force magnitude peaks at the third elbow at $t = 4\text{s}$, where the slugging phenomena happen frequently. A possible reason for the specific time step is that $t = 4\text{s}$ is the time step when most continuous gas phase attaches to one side of the pipe wall, squeezing the liquid to the other side and resulting in the largest pressure distinction among $t = 3\text{s}$, $t = 4\text{s}$ and $t = 5\text{s}$ in Jumper B.

In addition, it should be noted that the fluctuations of excitation force at the final two elbows are obviously weaker than that at the previous elbow for both Jumper A and B. Linking to the analysis of volume fraction, these phenomena have a strong correlation with the Taylor bubbles generated before the final two elbows. In Figure 4.7 ~ 4.10, the gas phase attaching to the wall of the final two elbows are less than other elbows, which directly leads to the decrease of force magnitude at the final two elbows.

4.4.4 Dynamic response analysis

The results of the time series of the reaction forces for different jumpers with fixed supports are shown in Figure 4.14, in which $N_{xi(i=1,2)}$, $N_{yi(i=1,2)}$ and $N_{zi(i=1,2)}$ are

denoted as the reaction forces of fixed supports $i\ (i = 1,2)$ in x, y and z directions respectively. The specific locations of fixed supports $i\ (i = 1,2)$ are provided in Figure 4.3. As shown in Figure 4.14 (a), the reaction force in the x direction is almost zero, therefore the response in the x direction can be ignored in Jumper A. For Jumper A, the reaction forces in the z direction are larger than the ones in the y direction. Considering the geometry of jumpers in Figure 1, it is evident that the reaction force in the z direction supports the weight of Jumper A and the two-phase flow with the influence of the two-phase flow movement, while the reaction force in the y direction is only affected by the two-phase flow. Consequently, the difference between the reaction forces in the y and z directions is reasonable.

In contrast to Jumper A, the characteristics of the reaction forces in Jumper B is different, especially in the x and y direction. From Figure 4.14 (b), the tendency of the reaction forces in the z direction is similar to that in Jumper A, while the reaction forces in x and y are small but not zero in Jumper B. The reason for the distinction of reaction forces in the x and y direction between Jumper A and B is the multiplanar geometry of Jumper B, which induces the three-dimensional response instead of the approximate in-plain response in Jumper A. According to the analysis of the reaction forces in Jumper A and B, it can be concluded that the ability to withstand the forces in the direction of gravity should be considered when designing the connections at the inlet and outlet of the jumper.

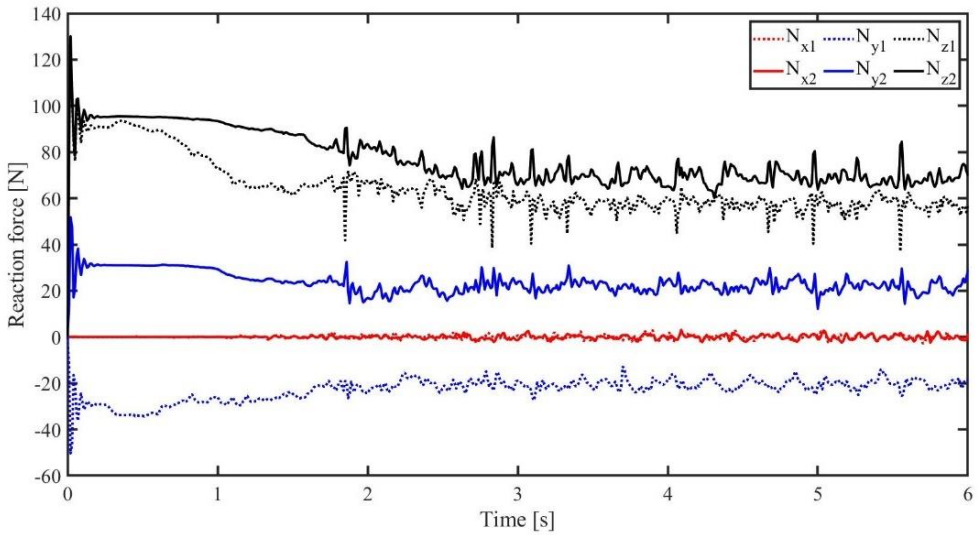

(a) Jumper A

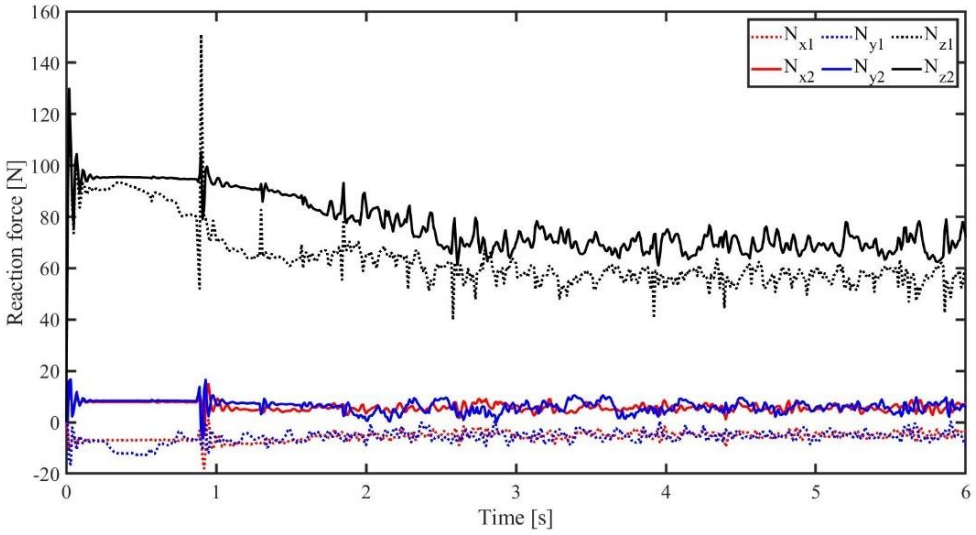

(b) Jumper B

Figure 4.14. Time series of reaction forces for different jumpers with fixed supports.

The deformation shapes of Jumper A and B after 3s are displayed in Figure 4.15. For Jumper A, because the reaction force in the x direction is almost zero, the deformation in the x direction is also can be neglected, thus the deformation in Jumper A is mainly in the y and z direction. From Figure 4.15 (a), the bottom side of Jumper A visibly sinks and the maximum magnitude of displacement happens at the upper sides of Jumper A. As mentioned before, the gravity of the jumper and the multiphase flow contributes most to the reaction force in the gravity direction. Therefore, this deformation shape in Jumper A is in good agreement with the results of the reaction forces discussed before.

As the deformation shape of Jumper B in Figure 4.15 (b) shows, the slight deformation in the y direction occurs at the bottom straight pipe component apart from the sinking of the middle jumper. Considering that Jumper B is multiplanar, the three-dimensional deformation in Jumper B is reasonable. Comparing Jumper A and B, the maximum magnitude of displacement in Jumper B is higher than that in Jumper A. A possible reason is that the multiplanar geometry of Jumper B enhances the secondary flow which boosts the slugging effect in Jumper B. Moreover, in the design of the jumper, the ability to withstand tension should be considered for the upper components of the jumper where the maximum displacement occurs in both Jumper A and B.

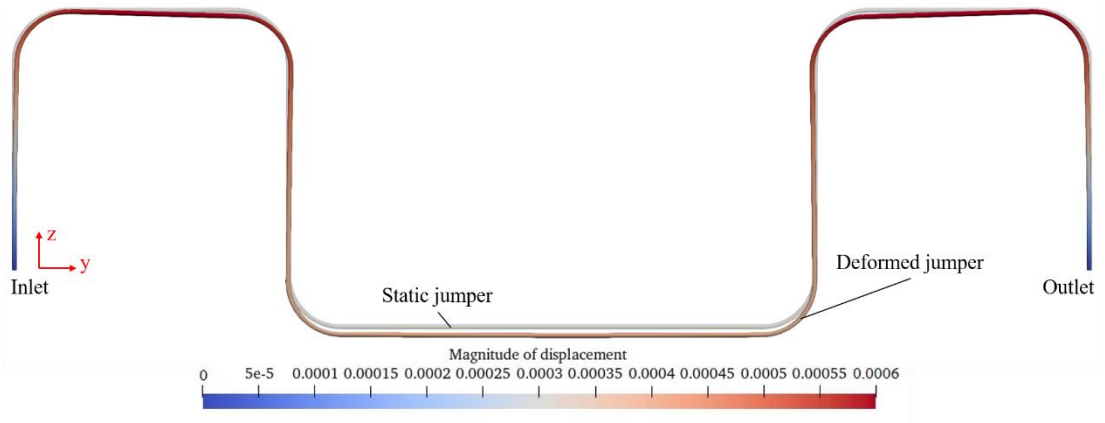

(a) Jumper A

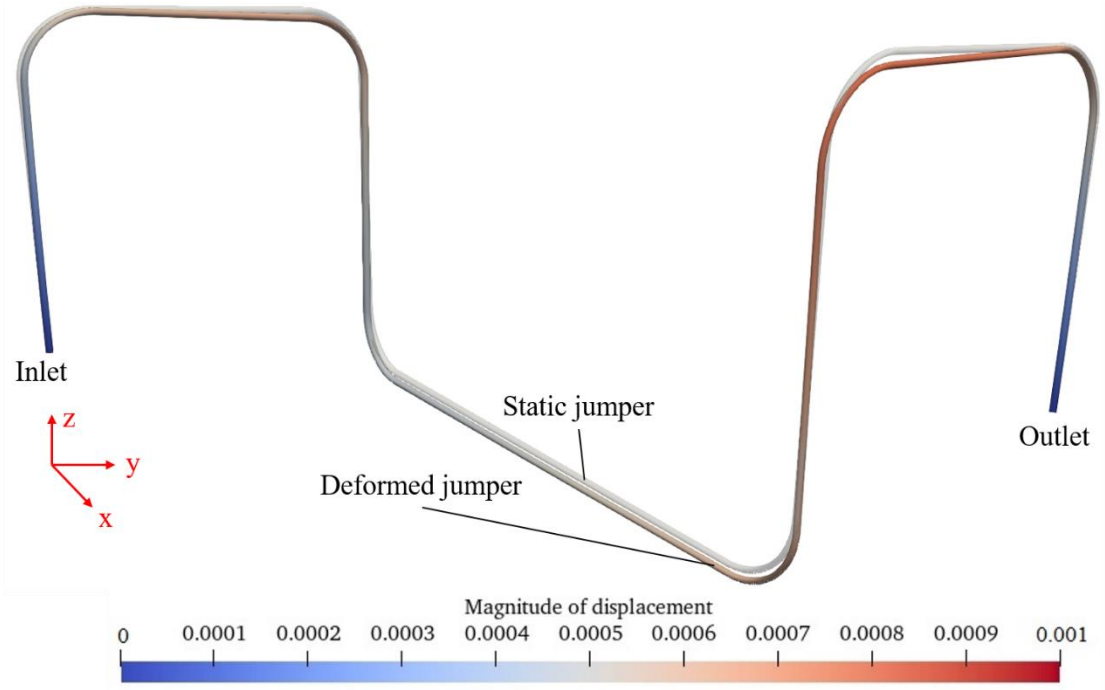

(b) Jumper B

Figure 4.15. Deformation shape of different jumpers with fixed supports after 3s.

4.5 Conclusion

In the present study, CFD simulations are carried out to investigate the gas-liquid two-phase flow inside uniplanar and multiplanar jumpers and a finite element analysis is performed to investigate the dynamic response of the jumpers to the two-phase flow-induced forces. The VOF method is used to capture the interface between the liquid and the gas phases. The gas-liquid two-phase flow characteristics in jumpers and the relevant dynamic response are discussed. The main conclusions are outlined below:

- Slugging phenomena frequently occur in the middle of both Jumper A and B, where the flow is stratified because of the density distinction between the two phases. Large-scale Taylor bubbles are observed in the vertical straight pipe component after the jumper sections where slugging phenomena happen. The elongation of

Taylor bubble has a strong correlation with gravity and the interaction of the liquid phase.

- The excitation forces of gas-liquid two-phase flow in jumper mainly peak at the elbow sections, where the gas phase with smaller density accumulates and is attached to the elbow wall and thus the pressure distinction suddenly increases. Moreover, the excitation force will increase where the Taylor bubbles just pass through.
- For the uniplanar jumper, the deformation shape is mainly also in-plain, while for the multiplanar jumper, the deformation shape is also three-dimensional. The maximum magnitude of displacement occurs at the upper side of both Jumper A and B, with the sinking of the middle part of the jumper. Therefore, the material tensile capacity at the upper side of the jumper needs to be checked in the jumper design.

References

1. Hara F. Two-phase flow induced vibrations in a horizontal piping system. J. Nippon Kikai Gakkai Ronbunshu, 1976, 42, 2400-2411.

2. Pettigrew M J, Taylor C E. Two-phase flow-induced vibration: An overview. J. 1994.

3. Pettigrew M J, Taylor C E, Fisher N J, et al. Flow-induced vibration: recent findings and open questions. J. Nuclear Engineering and Design, 1998, 185, 249-276.

4. Riverin J L, Pettigrew M J. Vibration excitation forces due to two-phase flow in piping elements. J. 2007.

5. Al-Safran E. Investigation and prediction of slug frequency in gas/liquid horizontal pipe flow. J. Journal of petroleum science and engineering, 2009, 69,143-155.

6. Dinaryanto O, Prayitno Y A K, Majid A I, et al. Experimental investigation on the initiation and flow development of gas-liquid slug two-phase flow in a horizontal pipe. J. Experimental Thermal and Fluid Science, 2017, 81, 93-108.

7. Carvalho F C T, Figueiredo M M F, Serpa A L. Flow pattern classification in liquid-gas flows using flow-induced vibration. J. Experimental Thermal and Fluid Science, 2020, 112, 109950.

8. D Da Riva E, Del Col D. Numerical simulation of churn flow in a vertical pipe. J.. Chemical Engineering Science, 2009, 64, 3753-3765.

9. Bossio V B M, Blanco A A J, Casanova M E L. Numerical modeling of the dynamical interaction between slug flow and vortex induced vibration in horizontal submarine pipelines. J. Journal of Offshore Mechanics and Arctic Engineering, 2014, 136.

10. Araújo J D P, Miranda J M, Campos J. CFD study of the hydrodynamics of slug flow systems: interaction between consecutive Taylor bubbles. J. International Journal of Chemical Reactor Engineering, 2015, 13, 541-549.

11. Parsi M, Agrawal M, Srinivasan V, et al. Assessment of a hybrid CFD model for simulation of complex vertical upward gas–liquid churn flow. J. Chemical Engineering Research and Design, 2016, 105, 71-84.

12. Pontaza J P, Menon R G. Flow-induced vibrations of subsea jumpers due to internal multi-phase flow. C. International Conference on Offshore Mechanics and Arctic Engineering. 2011, 44397, 585-595.

13. Chica L. FSI study of internal multiphase flow in subsea piping components. D, 2014.

14. Bruschi R, Parrella A, Vignati G C, et al. Crucial issues for deep water rigid jumper design. J. Ocean Engineering, 2017, 137, 193-203.

15. Kim J, Srinil N. 3-D numerical simulations of subsea jumper transporting intermittent slug flows. C. International Conference on Offshore Mechanics and Arctic Engineering. American Society of Mechanical Engineers, 2018, 51210, V002T08A028.

16. Zhu H, Hu Y, Tang T, et al. Evolution of Gas-Liquid Two-Phase Flow in an M-Shaped Jumper and the Resultant Flow-Induced Vibration Response. J. Processes, 2022, 10, 2133.

17. Li W, Zhou Q, Yin G, et al. Experimental Investigation and Numerical Modeling of Two-Phase Flow Development and Flow-Induced Vibration of a Multi-Plane Subsea Jumper. J. Journal of Marine Science and Engineering, 2022, 10, 1334.

18. Hirt C W, Nichols B D. Volume of fluid (VOF) method for the dynamics of free boundaries. J. Journal of computational physics, 1981, 39, 201-225.

19. Hossain M, Chinenye-Kanu N M, Droubi G M, et al. Investigation of slug-churn flow induced transient excitation forces at pipe bend. J. Journal of Fluids and Structures, 2019, 91, 102733.

20. Brackbill J U, Kothe D B, Zemach C. A continuum method for modeling surface tension. J. Journal of computational physics, 1992, 100, 335-354.

21. Menter F R, Kuntz M, Langtry R. Ten years of industrial experience with the SST turbulence model. J. Turbulence, heat and mass transfer, 2003, 4, 625-632.

22. Wang L, Yang Y, Li Y, et al. Resonance analyses of a pipeline-riser system conveying gas-liquid two-phase flow with flow-pattern evolution. J. International Journal of Pressure Vessels and Piping, 2018, 161, 22-32.

23. Gamet L, Scala M, Roenby J, et al. Validation of volume-of-fluid OpenFOAM® isoAdvector solvers using single bubble benchmarks. J. Computers & Fluids, 2020, 213, 104722.

24. Tocci F. Assessment of a hybrid VOF two-fluid CFD solver for simulation of gas-liquid flows in vertical pipelines in OpenFOAM. J. 2016.

25. Saidj F, Kibboua R, Azzi A, et al. Experimental investigation of air–water two-phase flow through vertical 90 bend. J. Experimental thermal and fluid science, 2014, 57, 226-234.

26. Dean W R. XVI. Note on the motion of fluid in a curved pipe. J. The London, Edinburgh, and Dublin Philosophical Magazine and Journal of Science, 1927, 4, 208-223.

27. Sudo K, Sumida M, Hibara H. Experimental investigation on turbulent flow in a circular-sectioned 90-degree bend. J. Ex-periments in Fluids, 1998, 25, 42-49.

Chapter 5.
Conclusions

5.1 Summary of the main finding

Based on the conclusions summarized in Chapter 3 and 4, the main findings of this thesis are concluded as below:

- In the 90-degree elbow structures including jumpers and pipelines with one or two elbows, large-scale Taylor bubbles are clearly observed with different formation mechanisms. Depending on the vertical or horizontal inlet, the generation of Taylor bubbles is different. For a pipeline with elbows and a horizontal inlet, the flow stratification will occur at the horizontal straight pipe components and the bubbles are formed because of the flow separation behind the elbow. For a pipeline with elbows and a vertical inlet, the gas phase interacting with the liquid is easy to accumulate as bubbles and further elongated into Taylor bubbles due to gravity. For both uniplanar and multiplanar jumpers, slugging phenomena and flow stratification normally happen in the middle horizontal pipe components, followed by Taylor bubbles at the subsequent pipe component. Moreover, for the regions where the slugging phenomenon is frequent, the secondary flow is also evident.
- The gas-liquid two-phase flow-induced forces on 90-degree elbow structures peak mainly at elbow sections, where the coalesced gas bubbles tend to attach to one side of the pipe wall and thus the pressure differences become considerably large at elbow sections. Besides, the flow-induced forces will also rapidly increase where the large-scale Taylor bubbles go through.
- For pipelines with 90-degree elbows, using fixed supports can effectively alleviate the fluctuation of the reaction forces of fixed supports and improve the damping effect of the pipelines. For jumpers, the dimension of deformation depends on the structural dimension. According to the results of dynamic response in jumpers, the magnitude of displacement peaks at the top of the jumpers and the middle section of the jumpers obviously sinks where the slugging phenomena frequently occur. Hence, the material tensile capacity at the upper side of the jumper needs to be checked in the jumper design.

5.2 Recommendations for future work

Based on the experience of this thesis, the recommendations for future work may focus on the following:

- Perform experiments of gas-liquid two-phase flow-induced forces in subsea jumpers to better validate the numerical result in this thesis.
- Conduct the fatigue analysis based on numerical results.
- For the interaction between gas-liquid two-phase flow and pipelines, utilize the two-way coupling method and compare the results with this thesis.
- Study on the characteristic of oil-water-gas three-phase flow and the flow-induced

forces in subsea jumpers. Carry out the numerical simulations including CFD simulation coupled with finite element analysis.

- Study on the effect of gas-liquid two-phase flow through an orifice.

Appendix A

alpha.water and U

Table A.1: alpha.water file in a case of pipe with 90-degere elbow

```
/*--------------------------------*- C++ -*----------------------------*\
| =========                 |                                            |
| \\      /  F ield         | OpenFOAM: The Open Source CFD Toolbox      |
|  \\    /   O peration     | Version:  v2012                            |
|   \\  /    A nd           | Website:  www.openfoam.com                 |
|    \\/     M anipulation  |                                            |
\*---------------------------------------------------------------------------*/
FoamFile
{
version     2.0;
format      ascii;
class       volScalarField;
object      alpha.water;
}
// * * * * * * * * * * * * * * * * * * * * * * * * * * * * * * * * * * * * //

dimensions      [0 0 0 0 0 0 0];

internalField   uniform 1;

boundaryField
{
#includeEtc "caseDicts/setConstraintTypes"

inlet
{
type            codedFixedValue;
value           uniform 1;

name    inlet;

codeInclude
#{
#include "fvCFD.H"
#};

codeOptions
#{
-I$(LIB_SRC)/finiteVolume/lnInclude \
-I$(LIB_SRC)/meshTools/lnInclude
#};
codeLibs
#{
-lfiniteVolume \
-lmeshTools
#};
code
#{
const fvPatch& boundaryPatch = this->patch();
const vectorField& Cf = boundaryPatch.Cf();
```

```
scalarField& field = *this;

scalar R=0.0206;

forAll(Cf, faceI)
{
scalar x = Cf[faceI].x(), y = Cf[faceI].y(), rSq = x*x + y*y;
if (rSq <= pow(R,2))
{
field[faceI] = 0;
}
else
{
field[faceI] = 1;
}

}
#};
}

pipe
{
type            zeroGradient;
}

outlet
{
type            zeroGradient;
value           uniform 0;
}
}

// ************************************************************************* //
```

Table A.2: U file in a case of pipe with 90-degere elbow

```
/*--------------------------------*- C++ -*----------------------------------*\
| =========                 |                                                 |
|          |
| \\      /  F ield         | OpenFOAM: The Open Source CFD Toolbox           |
|          |
|  \\    /   O peration     | Version:  v2012                                 |
|          |
|   \\  /    A nd           | Website:  www.openfoam.com                      |
|          |
|    \\/     M anipulation  |                                                 |
|          |
\*---------------------------------------------------------------------------*/
FoamFile
{
    version     2.0;
    format      ascii;
    class       volVectorField;
    location    "0";
    object      U;
}
// * * * * * * * * * * * * * * * * * * * * * * * * * * * * * * * * * * * * * * * //

dimensions      [0 1 -1 0 0 0 0];


internalField   uniform (0 0 0);
```

```
22.
23. boundaryField
24. {
25.     inlet
26.     {
27.         type            fixedValue;
28.         value           uniform (0 0 1.588);
29.     }
30.     outlet
31.     {
32.         type            zeroGradient;
33.     }
34.     pipe
35.     {
36.         type            fixedValue;
37.         value           uniform (0 0 0);
38.     }
39. }
40.
41.
42. // ************************************************************************* //
```

Appendix B

fvSchemes

Table B.1: fvSchemes file in a case of pipe with 90-degere elbow

```
/*--------------------------------*- C++ -*----------------------------*\
| =========                 |                                                 |
| \\      /  F ield         | OpenFOAM: The Open Source CFD Toolbox           |
|  \\    /   O peration     | Version:  v2012                                 |
|   \\  /    A nd           | Website:  www.openfoam.com                      |
|    \\/     M anipulation  |                                                 |
\*---------------------------------------------------------------------------*/
FoamFile
{
    version     2.0;
    format      ascii;
    class       dictionary;
    location    "system";
    object      fvSchemes;
}
// * * * * * * * * * * * * * * * * * * * * * * * * * * * * * * * * * * * * //

ddtSchemes
{
    default         Euler;
}

gradSchemes
{
    default         Gauss linear;
}

divSchemes
{
    default             none;

    div(rhoPhi,U)       Gauss linearUpwind grad(U);
    div(phi,alpha)      Gauss vanLeer;
    div(phirb,alpha)    Gauss linear;

    "div\(phi,(k|omega)\)"      Gauss upwind;
    div(((rho*nuEff)*dev2(T(grad(U))))) Gauss linear;

}

laplacianSchemes
{
    default         Gauss linear corrected;
}

interpolationSchemes
{
    default         linear;
}

```

```
snGradSchemes
{
    default         corrected;
}

wallDist
{
    method meshWave;
}


// ************************************************************************* //
```

Appendix C

fvSolution

Table C.1: fvSolution file in a case of pipe with 90-degere elbow

```
/*--------------------------------*- C++ -*----------------------------*\
| =========                 |                                                 |
| \\      /  F ield         | OpenFOAM: The Open Source CFD Toolbox           |
|  \\    /   O peration     | Version:  v2012                                 |
|   \\  /    A nd           | Website:  www.openfoam.com                      |
|    \\/     M anipulation  |                                                 |
\*---------------------------------------------------------------------------*/
FoamFile
{
    version     2.0;
    format      ascii;
    class       dictionary;
    location    "system";
    object      fvSolution;
}
// * * * * * * * * * * * * * * * * * * * * * * * * * * * * * * * * * * * * //

solvers
{
    "alpha.water.*"
    {
        isoFaceTol      1e-6;
        surfCellTol     1e-6;
        nAlphaBounds    3;
        snapTol         1e-12;
        clip            true;
        reconstructionScheme isoAlpha;

        nAlphaSubCycles 1;
        cAlpha          1;
    }

    "pcorr.*"
    {
        solver          PCG;
        preconditioner
        {
            preconditioner  GAMG;
            tolerance       1e-5;
            relTol          0;
            smoother        GaussSeidel;
        }
        tolerance       1e-5;
        relTol          0;
        maxIter         50;
    }

    p_rgh
    {
        solver           GAMG;
```

```
        tolerance        5e-9;
        relTol           0.01;

        smoother         GaussSeidel;



        maxIter          50;
    };

    p_rghFinal
    {
        $p_rgh;
        tolerance       5e-9;
        relTol          0;
    }

    "(U|k|omega).*"
    {
        solver          smoothSolver;
        smoother        symGaussSeidel;
        nSweeps         1;
        tolerance       1e-6;
        relTol          0.1;
    minIter        2;
    };
}

PIMPLE
{
    momentumPredictor no;
    nCorrectors     2;
    nNonOrthogonalCorrectors 2;
}

relaxationFactors
{
    equations
    {
        ".*" 1;
    }
}


// ************************************************************************* //
```